

# **UNSTEADY SEPARATION POINT INJECTION FOR PRESSURE RECOVERY IMPROVEMENT IN HIGH SUBSONIC DIFFUSERS**

by

Brian D McElwain

S.B. Aeronautics and Astronautics  
Massachusetts Institute of Technology, 2000

## **DISTRIBUTION STATEMENT A**

Approved for Public Release  
Distribution Unlimited

Submitted to the Department of Aeronautics and Astronautics  
in partial fulfillment of the requirements for the degrees of

Master of Science in Aeronautics and Astronautics

and

Engineer in Aeronautics and Astronautics

at the

Massachusetts Institute of Technology

June 2002

© Brian McElwain, 2002. All rights reserved.

The author hereby grants to MIT the permission to reproduce and to distribute publicly paper and electronic copies of this thesis document in whole or in part.

20020822 001

Author:

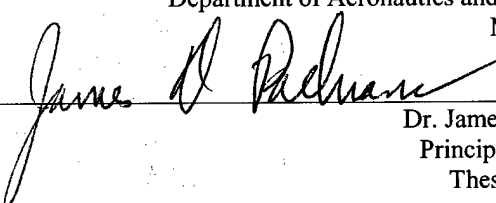


Brian D. McElwain

Department of Aeronautics and Astronautics

May 23, 2000

Certified by:



Dr. James D. Paduano

Principal Researcher

Thesis Supervisor

Certified by:

Professor Manuel Martinez-Sanchez  
Professor of Aeronautics and Astronautics  
Chairman, Engineer in Aeronautics and Astronautics Committee

Accepted by:

Professor Wallace E. Vander Velde  
Professor of Aeronautics and Astronautics  
Chairman, Departmental Graduate Committee

UNSTEADY SEPARATION POINT INJECTION FOR PRESSURE RECOVERY  
IMPROVEMENT IN HIGH SUBSONIC DIFFUSERS

by  
Brian D. McElwain

Submitted to the Department of Aeronautics and Astronautics on May 23, 2000 in partial  
fulfillment of the requirements for the Degrees of Master of Science in Aeronautics and  
Astronautics and Engineer in Aeronautics and Astronautics

**Abstract**

Serpentine inlet ducts on modern tactical aircraft distort the inlet flow and decrease pressure recovery at the aerodynamic interface plane (AIP). Current inlet designs are more aggressive, increasing distortion and decreasing pressure recovery at the AIP. Often the flow separates from the wall of the diffuser, creating most of the distortion and pressure loss in the inlet.

Diffuser separation experiments were conducted at high subsonic cruise conditions in a 2D test section. Periodic injection tangential to the flow at the separation point improved downstream pressure recovery. The injection also increased static pressure measured at the test section walls in the separated region. Flow visualization tests indicated that the separation shrinks as the injection mass flow increases. Pressure recovery also increased as injection mass flow increased. The unsteady component of the injection flow remained constant with injection mass flow, indicating that the steady component of the injection enhanced control of the separation. The preliminary conclusion is that the average velocity of the injection flow should be at least equivalent to the velocity of the core flow to maximize pressure recovery.

Experiments were also conducted in a one-sixth scale tactical aircraft diffuser at cruise conditions (3.1 lb/sec, maximum  $M = 0.65$ ). Periodic injection at the separation point improved the pressure recovery at the AIP. The improvement in pressure recovery at the AIP was limited to the area of pressure loss due to the separation in the diffuser. The diffuser has strong secondary flows that also cause losses at the AIP. These secondary flows prevented the injection from restoring pressure recovery as well as it had in the 2D test section. Higher injection mass flows than in the 2D case were required to achieve the same degree of improvement in pressure recovery at the AIP.

Thesis Supervisor: Dr James D. Paduano  
Title: Principal Researcher



## Acknowledgements

This work was supported by AFSOR contract #F49620-00-C-0035, as part of the DARPA Micro-Adaptive Flow Control Program, Dr. Thomas J. Beutner, contract monitor.

I would like to give thanks my advisor, Dr. Jim Paduano, for all the advice and direction he gave me on this project. Without his help, this study would not turned out so well. I also relied on the advise of Dr. Jerry Guenette help design the components used in my experiments. I would also like to thank Doug MacMartin for his insights into my work.

GTL technicians Jack and Jimmy helped immensely, assembling the probe for me and monitoring the De Laval during testing to allow me the freedom to conduct the test uninterrupted. Victor's machining advice and expertise were extremely valuable. I would also like to thank Lori and Mary for helping me take care of all the administrative tasks and providing a break from work when I needed it.

I would like to thank my friends who helped me during my graduate experience. Andrew, for helping me with all my testing and the many hours he spent racking his brain to help me find the answers I needed. Chris and Mark, for providing the daily lunch break to preserve our collective sanity and put everything in perspective. Sean, for always maintaining a positive outlook. Shannon and Jorge, for the fresh perspective they allowed me to see.

My family also deserves recognition. My mom and my sisters, Kim and Nellie, were there when I called to talk, always offering encouragement. David was the big brother I never had. Orlando reminded me that there is more to life than the present, but we cannot neglect the present, lest we miss out along the way.

Thanks to Spud, who stayed up with me into the wee hours of the morning, and Freckles, who got me up early the next morning.

And finally, thanks to Erin, for putting up with me throughout the whole odyssey. I would not have made it without you.



# Table of Contents

<b>ABSTRACT .....</b>	<b>1</b>
<b>ACKNOWLEDGEMENTS.....</b>	<b>3</b>
<b>LIST OF FIGURES .....</b>	<b>9</b>
<b>NOMENCLATURE .....</b>	<b>13</b>
<b>1 INTRODUCTION.....</b>	<b>15</b>
1.1 Background and Motivation.....	15
1.2 Prior Research .....	16
1.3 Approach .....	19
1.4 Research Objectives .....	20
1.5 Thesis Overview.....	21
<b>2 COMPONENT DESIGN .....</b>	<b>23</b>
2.1 De Laval Compressor.....	23
2.2 Tactical Aircraft Diffuser .....	25
2.3 2D Test Section .....	27
2.4 Injector Block .....	29
2.5 2D Flow Separator Bump.....	34
2.6 Rotary Valve.....	38
2.6.1 Valve Body .....	39
2.6.2 Valve Rotor .....	42
2.6.3 Top Plate .....	45
2.7 Unsteady Total Pressure Probe.....	47
<b>3 BENCH TEST .....</b>	<b>53</b>
3.1 Objective .....	53
3.2 Setup .....	53
3.3 Instrumentation.....	55
3.3.1 Unsteady Instrumentation .....	55
3.3.2 Steady Instrumentation.....	56

3.4	Data Acquisition.....	57
3.4.1	Unsteady Data Acquisition .....	57
3.4.1.1	Hardware.....	57
3.4.1.2	Software .....	58
3.4.2	Steady Data Acquisition.....	58
3.5	Actuation System .....	58
3.5.1	Steady Plenum.....	59
3.5.2	Rotary Valve .....	59
3.6	Calibration .....	60
3.7	Results .....	61
3.7.1	Steady Results .....	61
3.7.2	Unsteady Results.....	63
<b>4</b>	<b>2D TEST SECTION TESTS .....</b>	<b>73</b>
4.1	Objective .....	73
4.2	Setup.....	73
4.3	Instrumentation.....	76
4.3.1	Unsteady Instrumentation .....	76
4.3.2	Steady Instrumentation.....	76
4.4	Data Acquisition.....	77
4.4.1	Unsteady Data Acquisition .....	77
4.4.1.1	Hardware.....	77
4.4.1.2	Software .....	77
4.4.2	Steady Data Acquisition.....	78
4.4.2.1	Hardware.....	79
4.4.2.2	Software .....	79
4.5	Actuation System .....	80
4.6	Calibration.....	80
4.7	Results .....	80
4.7.1	Steady Results .....	80
4.7.2	Unsteady Results.....	82
4.8	Flow Visualization .....	92
<b>5</b>	<b>TACTICAL AIRCRAFT INLET TEST .....</b>	<b>97</b>
5.1	Objective .....	97
5.2	Setup.....	97
5.3	Instrumentation.....	100
5.4	Data Acquisition.....	102
5.4.1	Hardware .....	102

5.4.2	Software .....	103
5.5	Actuation System .....	103
5.6	Calibration.....	104
5.7	Results .....	104
<b>6</b>	<b>DISCUSSION .....</b>	<b>111</b>
6.1	Bench Test.....	111
6.2	2D Test Section Tests.....	113
6.3	Tactical Aircraft Inlet Test .....	115
<b>7</b>	<b>CONCLUSIONS .....</b>	<b>119</b>
7.1	Conclusions .....	119
7.2	Future Work .....	121
<b>APPENDIX A : DATA REDUCTION .....</b>		<b>123</b>
<b>APPENDIX B : COMPONENT DRAWINGS .....</b>		<b>135</b>
<b>APPENDIX C : INJECTOR REDESIGN .....</b>		<b>141</b>
<b>APPENDIX D : AERODYNAMIC INTERFACE PLANE (AIP) PROFILES.....</b>		<b>145</b>
<b>REFERENCES.....</b>		<b>155</b>



## List of Figures

Figure 2-1: De Laval Compressor Map .....	24
Figure 2-2: Tactical Aircraft Diffuser Following Oil Flow Visualization.....	25
Figure 2-3: CFD of Separation in Tactical Aircraft Diffuser ( $P_T/P_{T_0}$ ).....	26
Figure 2-4: Total Pressure Profile at the AIP ( $P_T/P_{T_0}$ ).....	27
Figure 2-5: 2D Test Section – Top Wall Shown.....	28
Figure 2-6: Injector Block.....	30
Figure 2-7: CFD of Coanda Injector (Flow Mach Number) .....	32
Figure 2-8: 4-percent Core Flow Coanda Injector .....	32
Figure 2-9: Front View of Supply Ducts .....	33
Figure 2-10: Side View of Supply Ducts .....	34
Figure 2-11: 2D Flow Separator Bump and Diffuser Centerline Profile .....	35
Figure 2-12: Actuator and Injector Block Mountings on Back of Flow Separator Bump ..	36
Figure 2-13: Static Pressure Tap for Mach Number Determination .....	37
Figure 2-14: Static Pressure Taps on Flow Separator Bump .....	38
Figure 2-15: Bottom of Rotary Valve Body .....	40
Figure 2-16: Top of Rotary Valve Body .....	41
Figure 2-17: Cut-away View of Flow Path through Rotary Valve Body .....	42
Figure 2-18: Rotary Valve Rotor .....	43
Figure 2-19: Cut-away View of Rotary Valve Rotor .....	44
Figure 2-20: Bottom of Rotary Valve Top Plate.....	45
Figure 2-21: Rotary Valve Components in Proper Arrangement .....	46
Figure 2-22: Rotary Valve Installed in Aircraft Diffuser.....	46
Figure 2-23: PSD of Warfield's Probe on Bench Mount .....	47
Figure 2-24: Completed Unsteady Total Pressure Probe.....	50
Figure 2-25: PSD of Unsteady Total Pressure Probe on Bench Mount .....	51
Figure 3-1: Bench Test Setup.....	53
Figure 3-2: Total Pressure Probe on Probe Stand .....	55
Figure 3-3: Steady Total Pressure Probe.....	56
Figure 3-4: Steady Plenum.....	59

Figure 3-5: Rotary Valve Mounted in Bench Test.....	60
Figure 3-6: Total Pressure Profile with 2% Core Flow Steady Injection .....	62
Figure 3-7: Total Pressure Profile with 4% Core Flow Steady Injection .....	62
Figure 3-8: Total Pressure Amplitude Peak to Peak vs Actuation Frequency and Spanwise Location .....	64
Figure 3-9: Average Total Pressure Oscillation Envelope and Offset.....	64
Figure 3-10: $C_\mu$ vs Frequency and Pressure Ratio .....	67
Figure 3-11: $C_\mu$ vs Frequency and Pressure Ratio Above 400 Hz.....	67
Figure 3-12: Total Pressure Envelope at 2.02 Pressure Ratio.....	68
Figure 3-13: Total Pressure Envelope at 2.9 Pressure Ratio.....	69
Figure 3-14: $C_\mu$ vs Pressure Ratio at 2 kHz Actuation.....	70
Figure 3-15: $C_\mu$ vs Span-wise Location for Pressure Ratios 2.9 and 3.1 .....	71
Figure 3-16: Steady $C_\mu$ vs Pressure Ratio .....	71
Figure 4-1: 2D Test Section Setup .....	74
Figure 4-2: Geometry vs Axial Distance .....	75
Figure 4-3: Total Pressure Profile with 4.04% Core Flow Steady Injection in 2D Test Section .....	81
Figure 4-4: $C_p$ vs Injection Mass Flow (1200 Hz actuation).....	84
Figure 4-5: $C_p$ vs Percent Injection Core Flow ( $F^+=1.37$ ).....	84
Figure 4-6: $C_p$ vs Actuation Frequency (0.018 lb/sec injection mass flow).....	85
Figure 4-7: $C_p$ vs $F^+$ (0.60 % Core Flow) .....	86
Figure 4-8: Total Pressure Profile with Steady Injection.....	87
Figure 4-9: Total Pressure Profile vs Injection Mass Flow (900 Hz actuation).....	88
Figure 4-10: Pressure Recovery Profile vs Normalized Distance form Wall ( $F+=1.03$ )....	88
Figure 4-11: Pressure Recovery vs Actuation Frequency (0.018 lb/sec injection, $C_\mu \sim 0.05\%$ ) .....	89
Figure 4-12: Pressure Recovery vs $F^+$ (0.60% Core Flow, $C_\mu \sim 0.05\%$ ) .....	90
Figure 4-13: Pressure Recovery vs Actuation Frequency and Injection Mass Flow ( $C_\mu=0.05\%$ ).....	91
Figure 4-14: Pressure Recovery vs $F^+$ and Percent Core Flow ( $C_\mu=0.05\%$ ).....	92
Figure 4-15: Flow Visualization Plate .....	93

Figure 4-16: Flow Visualization Plate Results .....	94
Figure 5-1: Tactical Aircraft Inlet Test Setup.....	98
Figure 5-2: Steady Total Pressure Can.....	101
Figure 5-3: Probe Locations in Steady Total Pressure Can .....	101
Figure 5-4: AIP Total Pressure Profile at 3.1 lb/sec without Injection .....	105
Figure 5-5: AIP Total Pressure Profile at 3.1 lb/sec with 0.106 lb/sec Injection at 2 kHz ( $C_{\mu}$ ~ 0.06% .....	106
Figure 5-6: AIP Pressure Recovery vs Core Mass Flow and Percent Injection Flow .....	107
Figure 5-7: AIP Pressure Recovery vs Core Mass Flow and Injection Steady $C_{\mu}$ .....	107
Figure 5-8: Upper Quadrant AIP Pressure Recovery vs Core Mass Flow and Percent Injection Flow.....	108
Figure 5-9: Upper Quadrant AIP Pressure Recovery vs Core Mass Flow and Injection Steady $C_{\mu}$ .....	109



## Nomenclature

A	Helmholtz throttle area
$A_{\text{duct}}$	Duct cross-sectional area
$A_{\text{inj}}$	Injection slot area
AIP	Aerodynamic Interface Plane
As	Separated area
c	Reference length (chord)
CFM	Cubic feet per minute
$C_{\mu}$	Unsteady momentum coefficient
$C_{\mu\text{steady}}$	Steady momentum coefficient
steady $C_{\mu}$	
$c_0$	Speed of sound
$C_p$	Coefficient of pressure
DN	Bearing diameter x RPM
f	Frequency
$F^+$	Nondimensional frequency
$f_{\text{actuation}}$	Frequency of actuation
$f_{\text{excitation}}$	Frequency of excitation
GPIB	General Purpose Interface Bus
h	Injection slot height
$h_{\text{bump}}$	Height of flow separator bump
$h_{\text{normalized}}$	Normalized distance from wall
L	Reference length
$\lambda$	Wavelength
I	Normalized axial distance
$L'$	Helmholtz throttle length
$L_{\text{separation}}$	Separated region length
M	Mach number
$\dot{m}$	Mass flow
$\dot{m}_{\text{calculated}}$	Calculated mass flow
P	Regulated pressure (referenced to atmospheric)
$P^*$	Reference calibration pressure
$P_{\text{atm}}$	Atmospheric pressure
$P_{\text{op}}$	Operating pressure (absolute)
$p_{\text{ref}}$	Reference static pressure
ProE	ProEngineer
$P_s$	Static pressure
$P_T$	Total pressure
$P_{T_0}$	Reference total pressure
$q_{\text{ref}}$	Reference dynamic pressure
R	Ideal gas constant
$\rho$	Density
$\rho_{\infty}$	Freestream density

$\rho_{core}$	Core flow density
$\rho_{inj}$	Injection flow density
SCFM	Standard cubic feet per minute
SDIU	Scanivalve Digital Interface Unit
SLA	Stereolithography
SLS	Selective Laser Sintering
$T^*$	Reference calibration temperature
$T_a$	Atmospheric temperature
$T_{op}$	Operating temperature
$U_\infty$	Freestream velocity
$U_{inj}$	Mean injection velocity
$u_{inj}$	Amplitude of oscillation of injection velocity
$V$	Helmholtz resonator volume
$V_\infty$	Freestream velocity
$V_{core}$	Core flow velocity
$V_{inj}$	Mean injection velocity
$\langle v_j \rangle^2$	Mean squared injection velocity oscillation amplitude
$x$	Position of bullet in mass flow throttle plug
$x_{axial}$	Axial distance
$y$	Distance from wall

---

# **1 Introduction**

---

## **1.1 Background and Motivation**

The engines of many tactical aircraft are buried inside the body of the craft. The engine is fed by a duct that channels outside flow to the engine face. These ducts are often serpentine ducts, moving the air laterally and diffusing it at the same time. Traditionally, serpentine ducts distort the flow and decrease pressure recovery, the amount of freestream total pressure retained in the flow, as they deliver the flow to the engine. As inlets become more aggressive, performing the same function in a shorter length, the distortion, or non-uniformity of the flow, increases, and the pressure recovery decreases. Often, the turning of the flow in serpentine inlets causes the flow to separate from the inlet wall. Such separation, if it occurs, is the largest cause of distortion and lost pressure recovery in these inlets.

The overall purpose of this thesis is to study and control the separation in a tactical aircraft inlet to improve the pressure recovery at the Aerodynamic Interface Plane (AIP). The AIP is an imaginary reference plane between the inlet and the engine face. Inlet pressure recovery and distortion levels are quantified at the AIP. The research that constitutes this thesis describes a portion of a joint research program between the Massachusetts Institute of Technology (MIT), the California Institute of Technology (Caltech), NASA Glenn and Northrop Grumman. The tactical aircraft inlet that serves as the test inlet for this project is a scaled model that was built by Northrop Grumman. The inlet is a serpentine duct to meet the requirement that the compressor blades be partially hidden from view. The flow separates from the upper wall of the inlet at moderate and high inlet mass flows, causing a significant pressure loss at the AIP.

In some vehicles, the length of the propulsion system sets the size of the aircraft. Thus, future designs may have more aggressive inlets to shorten the propulsion system and reduce the size of the overall aircraft. Careful aerodynamic design of these inlets can provide resistance to separation. In order to further shrink the length to the ultimate

desired values, such aerodynamic design alone cannot prevent separation. The flow inside the duct must be controlled to preserve pressure recovery.

## 1.2 Prior Research

Control of flow separation has been addressed in many studies. Grenblatt and Wygnanski [1] reviewed studies of separation control on external flows at low Mach numbers using periodic excitation including: injection, acoustic pulses and synthetic jets that have injection and suction phases that yield zero net mass flux. They concluded separation can be affected with both steady and periodic excitation. Periodic excitation performed better than steady injection, allowing control with much lower input energy. Input energy is the amount of energy used to create the periodic excitation [1].

Steady injection was found to be detrimental below momentum coefficients (Equation 1-1) of  $\sim 2\%$  [1].

$$C_{\mu_{\text{steady}}} = \frac{\rho_{\text{inj}} U_{\text{inj}}^2 h}{\rho_{\infty} U_{\infty}^2 c} \quad (1-1)$$

In this equation,  $\rho_{\text{inj}}$  and  $U_{\text{inj}}$  are defined as the density and mean velocity of the injected flow.  $\rho$  and  $U$  are defined as the density and velocity of the freestream flow.  $h$  is the width of the injection slot and  $c$  is a reference length, usually the chord of the airfoil being tested [1].

Periodic excitation at a momentum coefficient (Equation 1-2) of  $\sim 0.02\%$  was found to have a large effect on the separation [1].

$$C_{\mu} = \frac{\rho_{\text{inj}} U_{\text{inj}}^2 h}{\rho_{\infty} U_{\infty}^2 c} \quad (1-2)$$

Here,  $u_{\text{inj}}$  is defined as the amplitude of the oscillatory component of the velocity [1].

The best non-dimensional frequency for periodic excitation was found to be  $F^+ \sim 1$ .  $F^+$  is defined in Equation 1-3 where  $L$  is a reference length in the flow and  $f_{\text{excitation}}$  is the excitation frequency [1].

$$F^+ = \frac{f_{\text{excitation}} L}{U_\infty} \quad (1-3)$$

In order to further reduce the length of the separation bubble,  $F^+$  can be increased after the flow is reattached [1].

Steady suction was found to decrease the size of separation, but due to the weight and complexity of the associated system, suction was not deemed a feasible solution for use on aircraft [1].

In summary, most work on separation control has been conducted on external flows at low Mach numbers. The results of these studies indicate that periodic excitation maximizes the control of the separation for low input energy.

Often, synthetic jets are used to produce periodic excitation. Synthetic jets energize the boundary layer by ejecting high momentum fluid during half of the cycle and ingesting the low momentum boundary layer during the other half of the cycle. The suction half of the cycle is vital to the efficiency of the excitation. Without the suction stroke, the device would become an injection jet that requires an air supply to support the excitation. The combination of injection and suction allows the synthetic jets to create large variations in exit velocity with no net mass flow. These synthetic jets work well in low subsonic flows where the flow momentum is low. The velocities the jets produce are comparable to, if not greater than, the freestream flow velocity.

There is some question as to whether synthetic jets can perform as well in high subsonic flows. The peak injection velocity achieved by the jets may be above the freestream velocity, but during most of the cycle, the velocity produced will be lower than the freestream velocity. The injected momentum would be lower than the freestream momentum during most of the cycle, assuring a loss in pressure recovery due to the lower

total pressure of the injection flow relative to the freestream flow. Synthetic jets may not be able to produce enough momentum to perform well in high subsonic flows [2].

In a subsequent study, Seifert and Pack [3] confirmed the ability of pulsed injection to shrink the separated region by increasing  $F^+$  above 1 on a 2D wing section. They also demonstrated the ability of periodic excitation to decrease the severity of separation in high subsonic flow ( $M = 0.65$ ). An increase in the static pressure in the separated region indicated the decrease in separation severity [3]. These tests were conducted using no mass flow injection, but  $C_{\mu \text{ steady}}$  and  $C_{\mu}$  were relatively low (0.8% and 0.05% respectively) which limited the performance of the system at high Mach numbers.

In high subsonic flows, increasing  $F^+$  reduces the size of the separated region. The static pressure in the separated region should increase as the severity of the separation decreases.

In studies on a 2D divergent duct ( $20^\circ$  divergence of one wall), McCormick [4] used directed synthetic jets to improve pressure recovery in incompressible ( $M = 0.05$ ) flow. He found the static pressure profile along the wall with  $C_{\mu} = 0.2\%$  to be comparable to an “optimal” uncontrolled case at lower wall divergence angle ( $13^\circ$ ). The optimal uncontrolled case was defined as the wall divergence angle that yielded the maximum pressure recovery without excitation. The pressure recovery continued to improve as  $C_{\mu}$  increased until saturation at  $C_{\mu} = 0.6\%$ . The optimal excitation frequency was found to be  $F^+ = 1$ . This frequency yielded the largest improvement of pressure recovery [4].

Amitay et al [5] tested a similar 2D section that simulated a serpentine duct. They placed a deflection block opposite a divergent wall to maintain constant flow area through a duct, turning the flow without diffusing it. Synthetic jets were placed perpendicular to the flow surface, immediately downstream of the separation line.  $C_{\mu}$  was redefined (Equation 2-4) to compensate for the difference between jet width and test section width [5].

$$C_{\mu} = \frac{\rho_{\text{inj}} u_{\text{inj}}^2 A_{\text{inj}}}{\rho_{\infty} U_{\infty}^2 A_{\text{duct}}} \quad (1-4)$$

Here  $A_{inj}$  is the combined exit area of the synthetic jets and  $A_{duct}$  is the cross-sectional area of the duct. They tested the section up to  $M = 0.3$  and found that when the flow reattached, it still suffered a total pressure loss from the separation. Increasing the level of actuation decreased the total pressure loss. Based on their results, Amitay et al hypothesized that periodic excitation can improve the separation behavior of serpentine inlets at high subsonic conditions. They also stated that for fixed input energy, actuation level goes down as freestream Mach number increases. This can cause difficulties in producing the actuation levels necessary for high subsonic core flows using synthetic jets [5].

These studies indicate that separation in 2D ducts can be controlled by periodic excitation. The energy required to generate the necessary control authority increases as core flow velocity increases. Synthetic jets may not produce sufficient control authority for use in high subsonic serpentine inlets.

### 1.3 Approach

This research focuses on separation control in high subsonic serpentine inlets. The core flow Mach number ( $M = 0.65$ ) is higher than in previous internal flow separation control experiments. The associated higher core flow momentum makes it difficult to achieve the actuation momentum levels necessary to control the separation. The test inlet is an accurate one-sixth scale 3D serpentine inlet, a configuration that has not been previously tested using periodic excitation. The approach to these factors is discussed in the following paragraphs.

The core flow Mach number is higher than in previous internal flow separation control experiments. The momentum of the core flow will be higher, per unit mass, than in previous testing. In order to achieve the same control authority as in previous testing [3,4] with a thin actuation slot, the oscillation in injection velocity must be large.

The high core momentum makes it difficult to achieve the necessary actuation momentum levels. Current synthetic jets do not produce sufficient average injection momentum to interact with the core flow without introducing losses. That is, if the average momentum of the flow has lower total pressure than the core flow, the jet becomes a new source of

total pressure loss. In order to avoid such low average momentum, this study will use injection instead of synthetic jets. The injection will attain both the average and peak momentum level necessary by introducing oscillation about a non-zero average velocity. Varying the average velocity controls the average injection momentum. Varying the periodic injection velocity about the average velocity produces the oscillatory momentum. This will produce actuation with sufficient control authority that does not introduce a separate source of total pressure loss.

Actuator designs that can produce this type of injection profile are currently under development and should be available for service on aircraft in the near term. This research does not focus on new actuator development.

To maximize the effect of injection, a Coanda injector will be used. These injectors introduce flow tangential to the wall by taking advantage of the Coanda effect. The Coanda effect states that flows will follow a diverging flow surface as long as it does not diverge too rapidly. In this case, the flow will follow the wall of the diffuser as it bends away from the core flow direction in the serpentine inlet. Another benefit of Coanda injectors is that they do not tend to separate the flow when there is a non-zero mean flow, eliminating the need for a suction phase during the periodic cycle.

Experiments will be conducted in a 2D test section to reduce the number of variables inherent in the scaled aircraft inlet. The 2D experiment will limit the affect of secondary flows on the separation. It will also allow visualization of the flow to determine the nature of the effect of injection on the separated region. These results will be used to help understand the behavior of the separation in the serpentine aircraft inlet. The lessons learned from the 2D test will be applied to tests on the scaled tactical aircraft inlet.

## 1.4 Research Objectives

The objective of this research is to determine if unsteady injection at the separation line can improve pressure recovery at the Aerodynamic Interface Plane (AIP) in high subsonic inlets. More specifically, the goal is to determine if periodic velocity variations about a mean velocity can decrease the pressure loss at the AIP due to separation in the inlet. 2D

separation behavior is studied in order to investigate some of the details of the behavior in the 3D inlet. The focus of this research is to find the optimal injection parameters to improve pressure recovery at the AIP in the tactical aircraft inlet.

## 1.5 Thesis Overview

The remainder of this thesis focuses on five topics: experimental component description and design, bench testing of an actuator and injector, 2D testing of injection, injection testing in a model tactical aircraft inlet and discussion of the results of these tests. Chapter 2 provides a description of the experimental components including the design of fabricated components, including the actuator and injector. Chapter 3 describes the bench testing of the injector and actuator to characterize performance. The results describe both flow uniformity and momentum coefficient ( $C_\mu$ ). Chapter 4 details the configuration and results for tests conducted in a 2D test section. Results include static pressure profiles on the wall, total pressure profiles downstream of the separation and oil flow visualization. Chapter 5 discusses the setup and results of testing the injector and actuator in a model tactical aircraft inlet. Chapter 6 presents a discussion of the results of the three tests and their implications.



---

## **2 Component Design**

---

In order to study the effects of injection on the separation, tests were conducted in both 2D and 3D test rigs. The 3D test consisted of injection in a tactical aircraft diffuser (Section 2.2) at cruise flow conditions. Instrumentation in the diffuser measured the steady total pressure at the AIP to determine pressure recovery. This limited data could not directly indicate how injection affected the separation. In order to study the separation better, 2D tests were conducted in a 2D test section (Section 2.3). The 2D test section allowed both quantitative measurements and qualitative observations of the effect of injection on the separation. The results from testing in the 2D test section were applied to tests in the 3D test section; they were used to determine the best injection parameters and interpret the test results.

To ensure similar injection in both test facilities, the injector and actuator were designed for use in both test sections. The injector was designed into an interchangeable injector block (Section 2.4). This allowed the injection path to be changed quickly and easily without extensive modifications to either test section.

Tests in the 2D test section established the relationships between injection parameters and pressure recovery. The flow visualization tests indicated the physical mechanism the injection caused that resulted in increased pressure recovery. The relationships between injection parameters and pressure recovery were also then measured in the 2D inlet. The relationships were then used to determine and test the injection parameters in the 3D inlet.

### **2.1 De Laval Compressor**

The high subsonic experiments were conducted using a De Laval air compressor. The compressor is capable of pulling up to approximately 13 lbs/sec mass flow at a low pressure ratio, or lower mass flows at pressure ratios up to approximately 3.8. The compressor map is shown in Figure 2-1. The mass flow factor is the corrected mass flow through the compressor (Equation 2-1 where  $P_s$  is static pressure in psi and  $T_a$  is ambient temperature in °R).

$$\dot{m} = \frac{MFF \cdot P_s}{2.665 \times 10^{-3} \sqrt{T_a}} \quad (2-1)$$

The nominal operating point for the 2D test section was 2700 RPM which yielded  $M = 0.76$  past the top of the flow separator bump (Section 2.5) without injection and  $M = 0.67$  past the top of the bump with injection. The nominal operating point for the aircraft inlet was 4300 RPM.

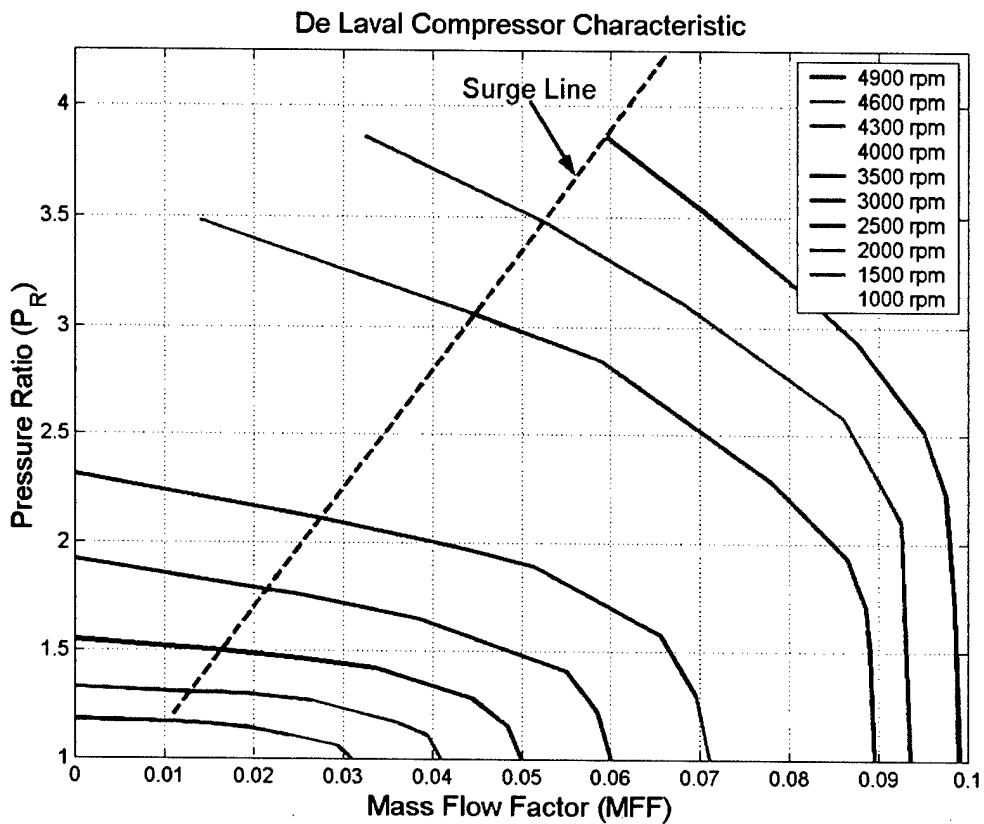


*Figure 2-1: De Laval Compressor Map*

The De Laval compressor inlet is fed by a 24-inch diameter pipe that can be fitted with various inlets, to generate high-subsonic flow used in the experiments described in this thesis. Two inlets were used: a prototype tactical aircraft diffuser designed and built by Northrop Grumman, and a 2D test section. These devices are described in the following sections.

## 2.2 Tactical Aircraft Diffuser

The tactical aircraft diffuser (Figure 2-2) is a one-sixth-scale wind tunnel model of the front section of a tactical aircraft prototype [6]. It is a serpentine duct inlet that redirects and diffuses the inlet flow to the front of the engine. The diffuser is used to simulate the flow conditions at the AIP at various operating conditions. To simulate cruise conditions, a bellmouth is mounted on the front of the diffuser instead of the actual inlet leading edge.

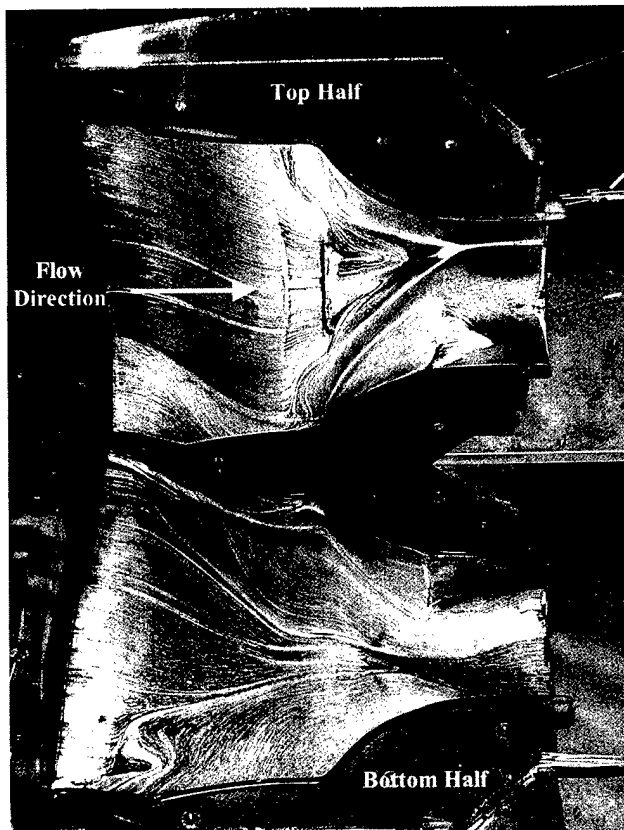


*Figure 2-2: Tactical Aircraft Diffuser Following Oil Flow Visualization*

The diffuser was formed using a rapid prototyping stereolithography (SLA) procedure, where the parts were grown layer by layer in an epoxy bath. They were then sanded and painted to produce a clean flow surface. The bellmouth was grown in four parts using the same SLA procedure. They were assembled and sanded to provide a clean flow path.

This diffuser was chosen because the flow separates off the upper wall of the diffuser (Figure 2-3), causing a loss in pressure recovery at the AIP (Figure 2-4). This loss

increases as mass flow through the diffuser increases. The poor flow characteristics of this diffuser make it a suitable candidate for testing the effects of separation point injection on pressure recovery at the AIP. Subsequent redesigns of the diffuser have modified the geometry that causes the separation and improved the pressure recovery in current designs. Such redesigns can still benefit from separation point actuation when operating at off-design conditions. Separation point actuation can also allow development of more aggressive inlets in the future.

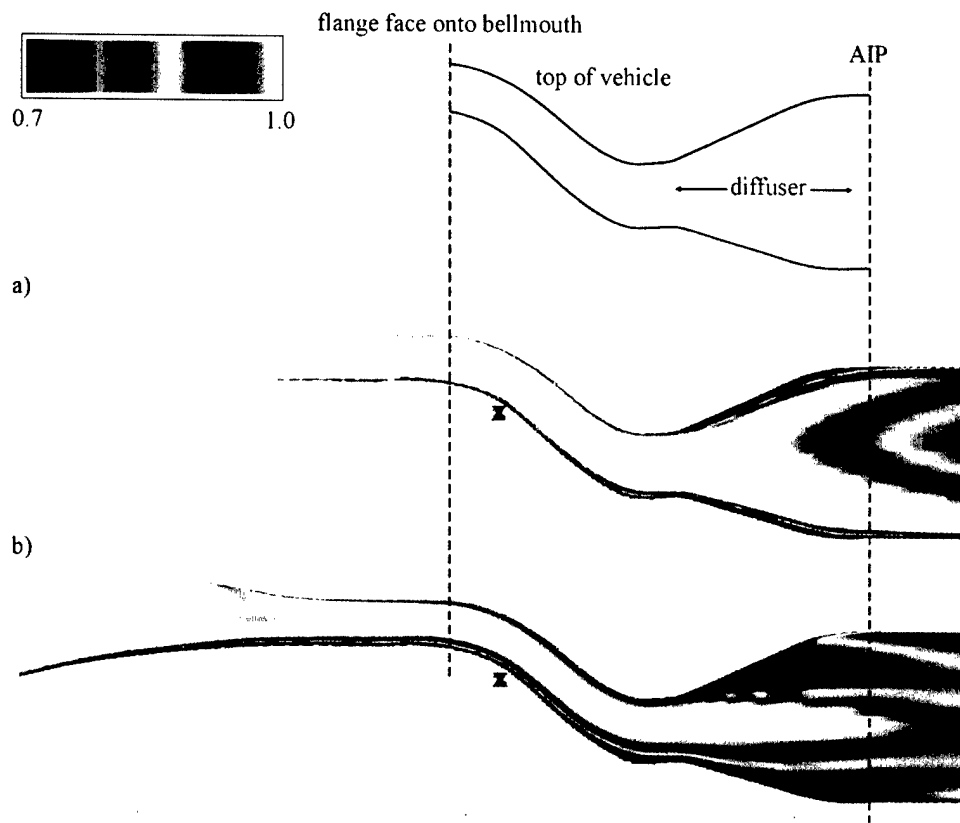


*Figure 2-3: CFD of Separation in Tactical Aircraft Diffuser ( $P_r/P_{T_0}$ )*

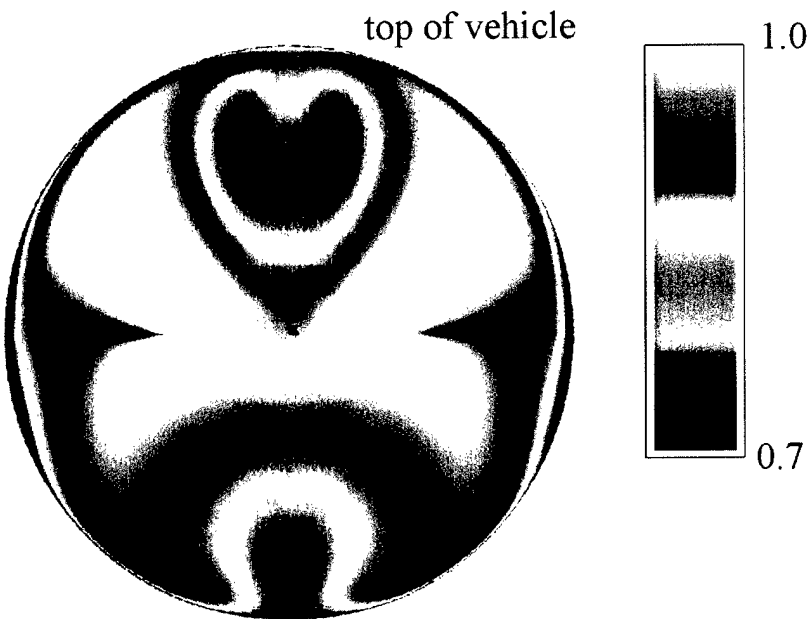


*Figure 2-4: Total Pressure Profile at the AIP ( $P_T/P_{T0}$ )*

### 2.3 2D Test Section

The 2D test section has a square 7 x 7 inch cross-section that runs 35 inches from a bellmouth-type entrance to a screen and mounting plate. The test section mounts directly on the De Laval compressor piping. The sides of the section are made of 15/16 inch Plexiglas pieces caulked and bolted together at two-inch intervals on one side and a combination of one- and two-inch intervals on the other side. The two-inch intervals are on the first 11 inches immediately downstream of the bellmouth and in the last four inches before the screen. The middle 20 inches of test section has one-inch bolt spacing. One wall in this middle section is removable and consists of: one 7 x 7 inch square aluminum plate, one 7 x 8 inch Plexiglas plate with an aluminum backing plate, and two Plexiglas inserts (either one and four inches or two and three inches long) to fill in the remaining five inches of wall. The test section can be mounted on the De Laval compressor piping with the removable wall on the upper, lower, left or right side of the test section. The 7 x 8 inch Plexiglas plate and aluminum backing plate have a traverse slot one-quarter inch wide and 5.25 inches long set one-half inch from the leading or trailing edge of the plate (depending on the plate's orientation in the test section). The backing plate has mounting holes for a lateral traverser along the slot. Another traverser can be mounted to the lateral traverser to

provide capability to scan across a cross-section of the test section. The one-inch spacing of the bolt holes in the test section allows the traverse to be moved to various axial positions in the test section. The one- to four-inch Plexiglas inserts allow the traverse plate to be moved to various positions while maintaining test section wall integrity. The assembled 2D test section is shown in Figure 2-5.

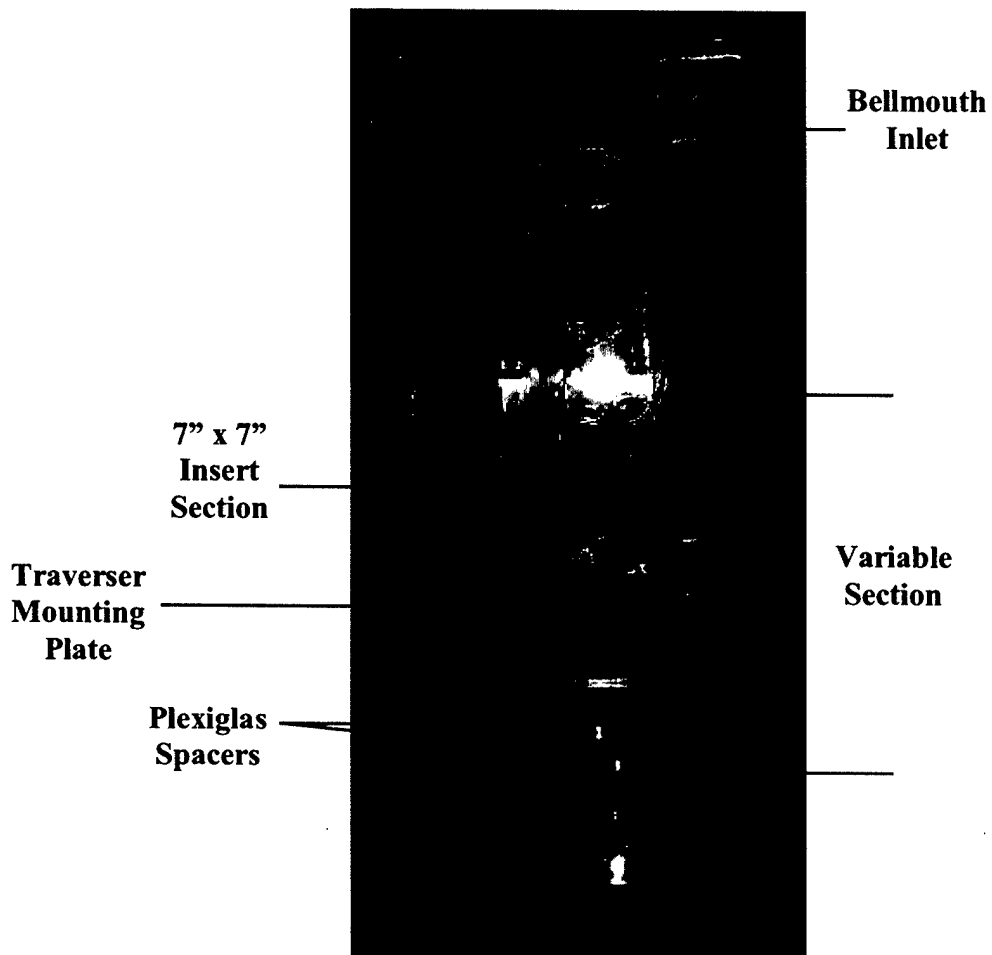


*Figure 2-5: 2D Test Section – Top Wall Shown*

The 2D test section has 12 static pressure taps, three equally spaced on each wall, located 6.5 inches downstream of the bellmouth. All 12 taps feed into a plenum. A tube runs from the plenum to a pressure transducer. The ratio of the measured static pressure to measured total pressure (taken to be atmospheric pressure) determines the Mach number of the flow.

Using the Mach number, total pressure and total temperature (taken to be room temperature) the properties of the flow can be determined.

## 2.4 Injector Block

In order to allow various injector geometries to be tested, the injector block was developed. This piece seats either inside the flow separator bump (Section 2.5) or into a section machined out of the aircraft diffuser. It seals to the actuator to prevent injection air from escaping during the experiment. The injector block is held in place by the actuator during testing.

The injector block (Figure 2-6) was designed to provide versatility in injector type and injector exit location relative to the separation line. The injector block is 4.5 inches in span, designed to allow injection along the entire four-inch separation line while maintaining a quarter-inch of material on either end of the injection duct. The block is 1.25 inches wide. It extends 0.4 inches downstream of the separation line, limited by the need for actuator mounting bolt holes in the flow separator bump after the cut is made for the injector block. It extends 0.85 inches upstream of the separation line to provide room for the injector duct inside the block.

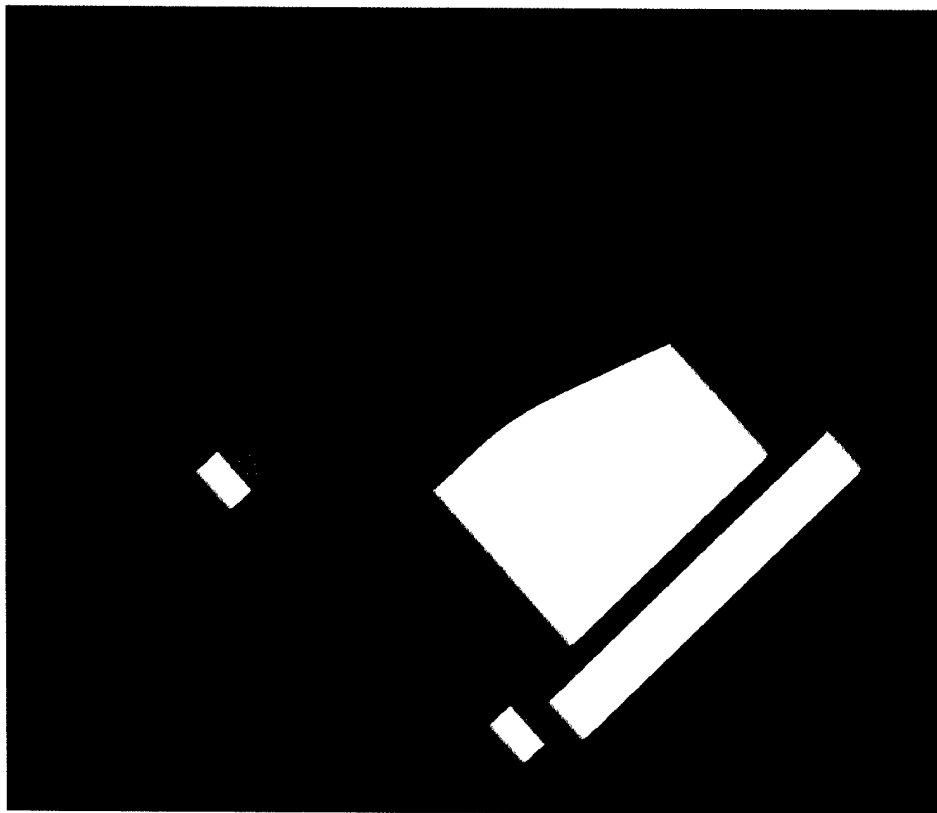


*Figure 2-6: Injector Block*

To ensure the flow surface of the injector block matches the flow surface of the diffuser it replaces, the injector block must be constrained in all three dimensions and fixed to prevent relative motion during experiments. The machined hole for the injector block constrains it in the axial and span-wise directions. A flange at the base of the injector block constrains it in the vertical direction. The flange is one-quarter inch thick and extends one-quarter inch from the rest of the block. Additionally, in order to prevent the injector block from being inserted incorrectly, there are two tabs on the downstream side. Each tab is one-quarter inch thick, one-quarter inch wide and one-half inch long. They fit into slots in the recess for the flange in the bump and diffuser.

The injector blocks can be manufactured using a stereolithography (SLA) or selective laser sintering (SLS) process. In both processes, the parts are created layer by layer. In SLA, the part is grown in an epoxy bath with a laser that solidifies thin sheets of epoxy to build the entire part. In SLS, a thin sheet of polymer particles is sprinkled in the growth

chamber. A laser melts particles to fuse them to the part. A new sheet of particles is required for each layer of the part.

The blocks tested in this thesis were grown in an SLS batch with the flow separator bump (Section 2.5). The SLS process left small pieces of the polymer material lodged in the injector ducts. Most of these pieces were easily removed by blowing high-pressure air through the duct. More pieces were removed by running a strip of paper through the slot. Unfortunately, a few large pieces still remained lodged in the duct (as evidenced by asymmetric total pressure deficits during steady injection). These last few pieces were removed using 600-grit sandpaper. The sandpaper slightly changed the geometry of the injector duct, opening up the cross-sectional area at the point of sanding. The results of this expansion will be discussed in Section 3.7.1.

The initial injectors were based on the NASA-optimized Coanda geometry. They were designed to inject a maximum of two and four percent of the aircraft diffuser's core flow of 3.1 pounds per second at cruise conditions. The Coanda geometry is designed to deliver high velocity flow that exits tangential to the wall. The injector relies on the Coanda effect to make the injection jet stick to the wall as it progresses downstream. The core flow through the diffuser is high subsonic (approximately Mach 0.65). Consequently, the average Mach number of the injection flow should be high as well. The injection stream also needed to be close to tangential to the wall, or it would shed a wake and possibly enhance the separation [7]. The injection was chosen to be exactly tangential in order to maximize the oscillatory component's ability to interact with the boundary layer in order to weaken or eliminate the separation [8].

The Coanda geometry (Figure 2-7) consists of a large constant area supply duct that converges to a smaller duct formed by two concentric circles. The large supply duct is designed to keep the flow below Mach 0.15 to reduce flow losses. The convergent neck of the duct accelerates the flow to Mach 1 at the exit. One side of the supply duct is tangential to the larger concentric circle. This forms one side of the Coanda injector. The other side of the supply duct converges to the inner concentric circle through an arc of the same radius as the inner concentric circle, with the opposite direction of curvature. In the

current set of injector designs, the inner concentric circle is placed tangent to the flow surface at the separation line (Figure 2-8).

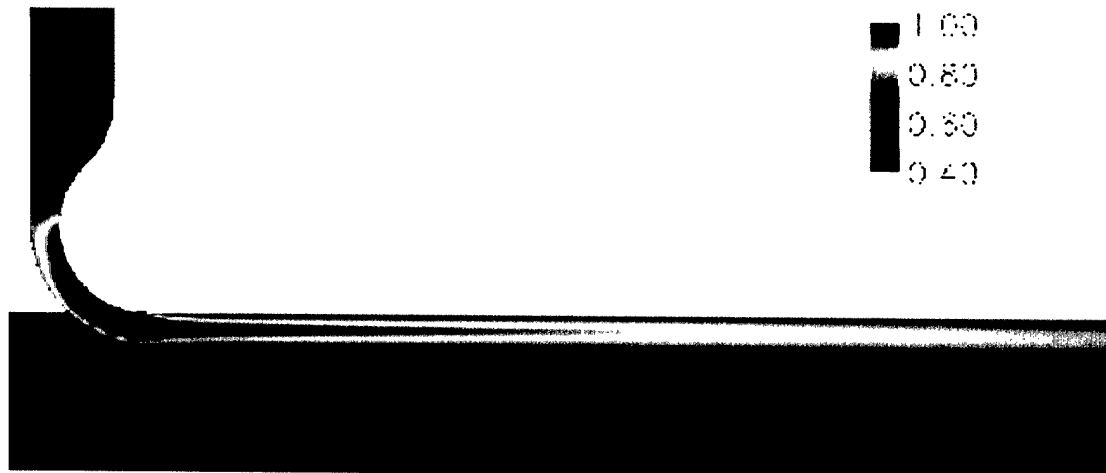


Figure 2-7: CFD of Coanda Injector (Flow Mach Number)

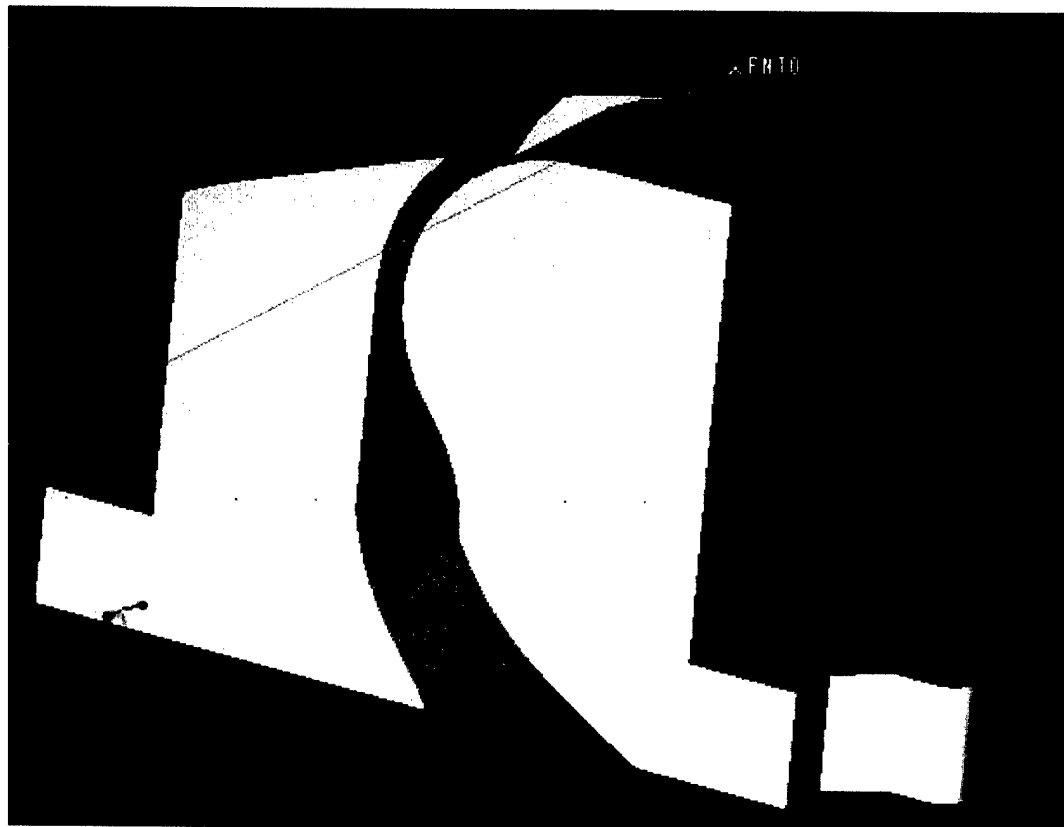
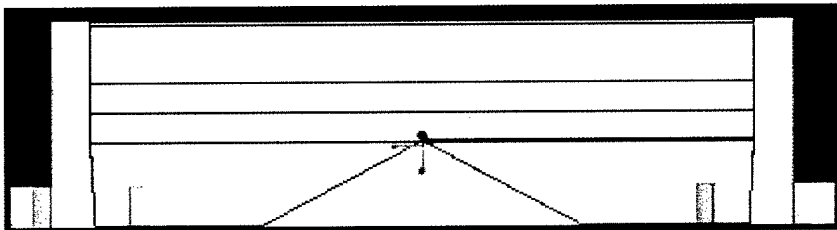
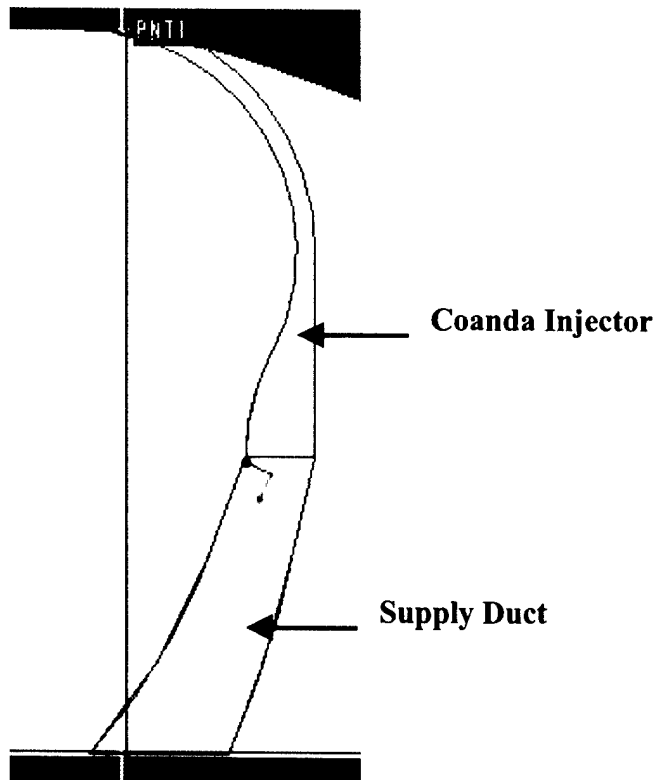


Figure 2-8: 4-percent Core Flow Coanda Injector

Due to the geometry of a proposed actuator from Honeywell (that was not subsequently used), the constant area supply duct changed shape between the exit of the actuator and the beginning of the duct convergence. The Honeywell actuator footprint allows air to be supplied at two locations, each from 0.97 to 1.97 inches from the centerline. The width of this supply area is 0.2442 inches for the 2-percent core flow injector and 0.4884 inches for the 4-percent core flow injector. While holding the supply duct area constant, the side lengths are then varied linearly until they merge into a four-inch long slot that is 0.1221 inches wide in the 2-percent core flow injector and 0.2442 inches wide in the 4-percent core flow injector. As shown in Figure 2-9, the separate slots merge into a single four-inch slot at the point where the duct begins to converge, creating a triangular divider in the center of the flow path. The short sides of the supply duct shift linearly from 1.97 inches to 2.00 inches off the centerline on the outside, and from 0.97 inches zero (merged) on the inside (Figure 2-9). The other sides of the supply duct shift in a smoother fashion in moving upstream of their initial location (Figure 2-10).



*Figure 2-9: Front View of Supply Ducts*



*Figure 2-10: Side View of Supply Ducts*

The injector block is sealed to the rotary valve by placing vacuum tape<sup>1</sup> around the air supplies. When the rotary valve bolts into position, the vacuum tape fills the leak passages between the injector block and the rotary valve, sealing the injection flow path. The vacuum tape seals up to approximately 100 psi pressure difference between supply pressure and ambient pressure [9].

## 2.5 2D Flow Separator Bump

Several considerations motivated testing in a 2D approximation of the aircraft diffuser environment. First, the aircraft diffuser is made from an almost opaque epoxy, eliminating any possibility of visualizing the flow in real time. Also, the instrumentation of the diffuser is restricted to a limited set of static pressure ports and measurements at the AIP.

<sup>1</sup> Vacuum tape is a strip of very viscous material, similar to clay but denser and more elastic. It conforms to surface geometry under compressive loading and adheres to the surface, preventing leaks across the seal.

Therefore, the 2D flow separator bump was designed to match the part of the diffuser that causes separation, while allowing visual access to the flow in real time. The design also allows instruments to be placed closer to the separation line and in varying positions for more detailed data acquisition.

The flow separator bump is a two dimensional representation of the centerline profile of the aircraft diffuser (Figure 2-11). The shape extends across the entire 7-inch span of the test section. It was created in Pro/Engineer (ProE) by extruding the centerline of the aircraft diffuser into a block the width of the 2D test section. The plane forming the bottom of this extrusion is parallel to the interface between the top and bottom halves of the aircraft diffuser. The protrusion is 2.33 inches high. The test section wall thickness is 0.94 inches, leaving 1.39 inches to contract the test section. At test conditions, this bump accelerates the flow from Mach 0.49 at the inlet to Mach 0.70 at the top of bump. The area reduction introduced by the bump was calculated using the compressible Mach relations in Equation 2-2:

$$\frac{A}{A^*} = \sqrt{\frac{1}{M^2} \left[ \frac{2}{\gamma+1} \left( 1 + \frac{\gamma-1}{2} M^2 \right) \right]^{\frac{\gamma+1}{\gamma-1}}} \quad (2-2)$$

This relation assumes constant velocity distribution across the cross-sectional area. The flow surface was built up at the ends of the protrusion to make the flow surface flush with the test section walls. This resulted in a mismatch between the flow surface and the 3D centerline profile at the ends of the bump (Figure 2-11). Threaded bolt holes were placed in the corners to allow the plug to be secured in the test section.

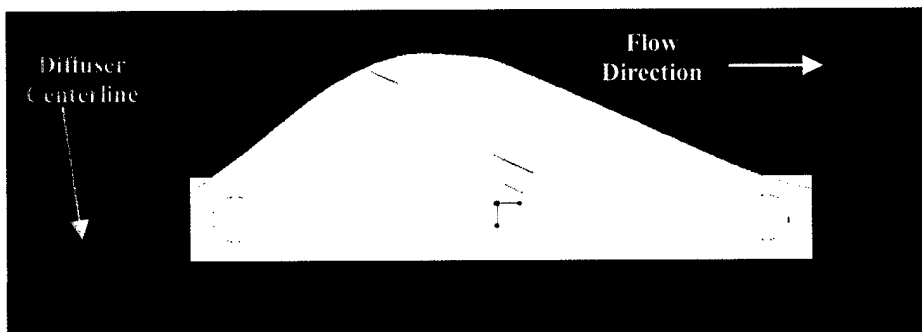
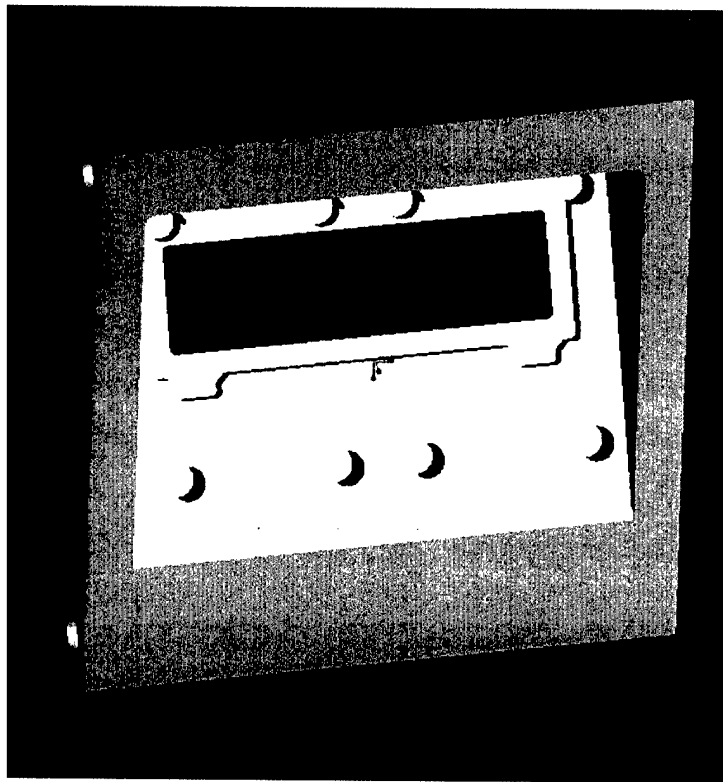


Figure 2-11: 2D Flow Separator Bump and Diffuser Centerline Profile

The 2D flow separator bump was also designed to house the injector block and actuator. To do this, a cutout was created in the bump to allow space for an actuator mounting (Figure 2-12). This section was placed parallel to the angled rear face of the flow separator bump, extending forward until the front edge of the section was one-quarter inch from the flow path [10]. Due to material limitations of the epoxy the diffuser is made from, at least one-quarter inch of material must be left around any cut into the diffuser. A section of the bump was then cut away to allow an interchangeable injector block (see Section 2.4) to be inserted. Holes were also added to allow two Honeywell 2 kHz actuators to bolt securely into the bump. The design incorporates two actuators instead of one to increase control authority and provide better span-wise spreading of the injection flow. Once the design was completed in ProE, a .STL file was generated and sent to NASA Glenn for fabrication using an SLS process.



*Figure 2-12: Actuator and Injector Block Mountings on Back of Flow Separator Bump*

When the bump arrived at MIT, threaded metal inserts were imbedded in the bolt holes to provide a reusable interface with the reinforcement provided by the inserts. The material

the SLS process uses would be crushed, stretched, cracked and broken during the repeated tightening of bolts throughout the experimental program. The bump also underwent post-manufacture machining to add instrumentation. Since the duct only converges on the side containing the flow separator, the flow above the bump will not be at uniform velocity. The one-sided contraction causes the flow closer to the bump to accelerate more than the flow on the far wall of the test section. The actual Mach number past the bump will be higher than 0.70 when the inlet reads pressures corresponding to Mach 0.49. For this reason, a static pressure tap (Figure 2-13) was placed at the highest portion of the bump to determine the actual flow Mach number. This tap is one-quarter inch from the wall to avoid interactions with the injector block slot.

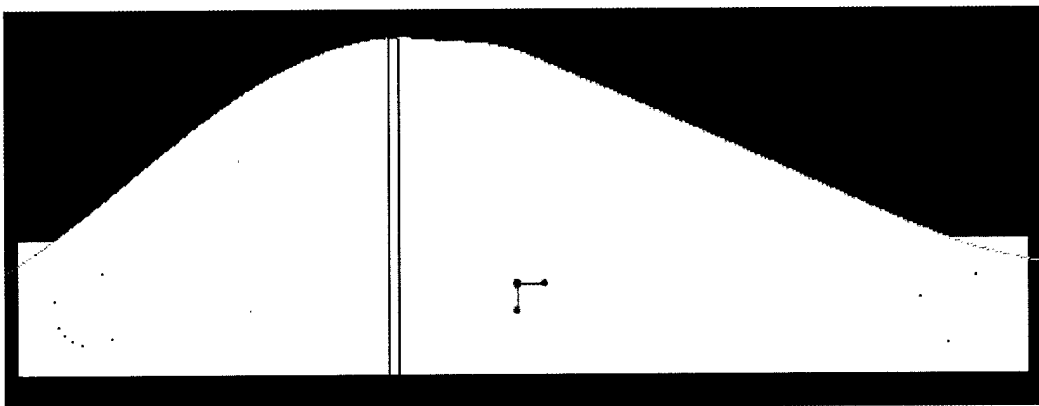
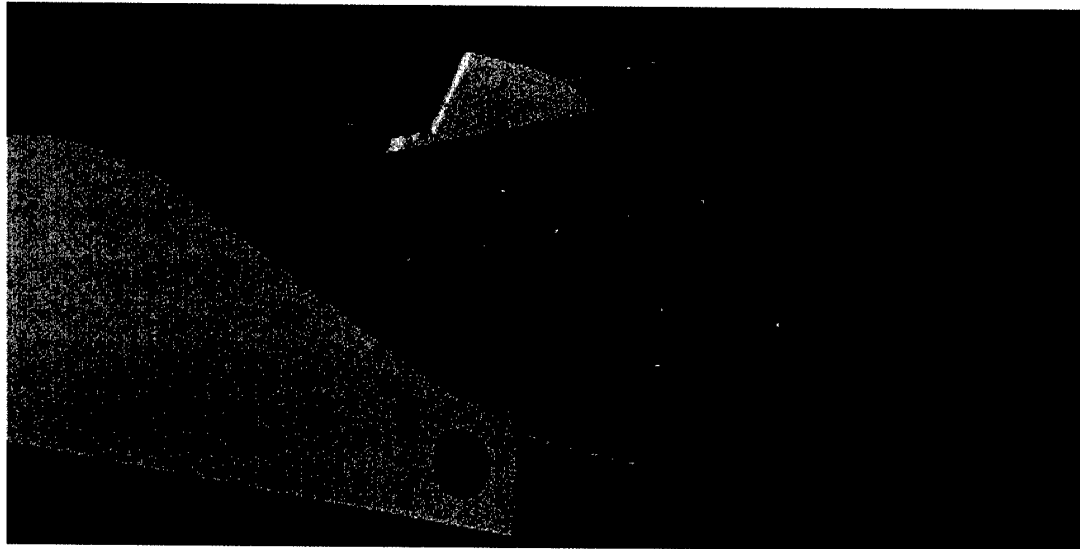


Figure 2-13: Static Pressure Tap for Mach Number Determination

Static pressure taps were also added to measure the effects of injection on downstream static pressure at the wall (Figure 2-14). Six of these taps are spaced at half-inch increments axially along the centerline of the flow separator bump, starting at 0.64 inches from the exit of the injector. This location corresponds to 20 slot widths downstream, the location chosen as a reference for the spatial uniformity of the injection flow. At 1.64 inches, there are four more taps, located one and two inches to either side of the centerline of the bump. At 3.02 inches, there is a tap one inch to the right of the centerline (measured facing the flow surface). At 3.27 inches, there is a tap one inch to the left of the centerline. All the taps except the centerline tap at 3.14 inches are perpendicular to the flow surface. The tap at 3.14 inches falls on the interface line between the angled rear face of the bump and the test section wall. The tap was placed at the angle halfway between the

perpendicular vectors of both surfaces. Additionally, another tap was added in the Plexiglas section immediately downstream of the bump at 4.14 inches downstream of the injector exit.



*Figure 2-14: Static Pressure Taps on Flow Separator Bump*

## 2.6 Rotary Valve

After NASA built the initial injector blocks, it became clear that the 2 kHz actuators from Honeywell would not be available. The rotary valve was designed as a replacement. It distributes air from a central plenum to the two supply ducts at a frequency set by the speed of the motor driving the rotor.

There are several requirements that must be met by the design of the rotary valve. It must attach to the Honeywell actuator footprint. It must also fit into the flow separator bump. The air exit passage must line up with the supply duct on the injector block. It must output a usable signal at 2kHz. It was designed to use an AstroFlight Model 640 Cobalt-40 motor. The motor is capable of delivering up to 600 W at a static speed of 12000 - 15000 RPM [11]. It will operate at higher speeds but will deliver less than the maximum 600 W. The motor already has a mounting brace and a 16-tooth sprocket mounted on it for rotational speed measurements.

The basic design of the rotary valve was chosen to be a rotor spinning in a round chamber with tight clearances. The air supply enters the valve body on one side of the rotor chamber. It passes through a transfer channel near the bottom of the rotor and enters the rotor through the bottom. The air then resides in a plenum inside the rotor until radial holes drilled in the rotor line up with slots in the valve body. When the holes and slots are aligned, air is ejected into exit channels. There are ten holes in the rotor, allowing the rotor to turn at 12000 RPM while the valve produces a signal at 2 kHz. The air then flows through the exit channels into the injector block. The rotor is held in place by a top plate that bolts to the valve body.

### **2.6.1 Valve Body**

In order to meet the requirements while maintaining the ability to dynamically change the model, the rotary valve was designed in ProE. It started as a 5.75 x 3.50 inch block of variable thickness. The attachment bolt holes were placed according to the pattern already designed into the flow separator bump. With the bolt holes in place, the ejection slots were placed. The edge of the slot is placed 0.911 inches from the line through the center of the bolts on the appropriate side of the rotary valve. The slots are 1.328 inches deep to allow the bottom 0.317 inches of the rotor disk to be used for flow ejection (with the bottom 0.091 inch reserved for structural integrity). The top 0.091 inch was reserved to provide structural integrity of the disk while preventing the injection flow from leaking out through the top of the valve. The slots can extend to 1.577 inches to allow the remaining 0.249 inches of rotor disk to be used, but the slots are currently 1.328 inches to preserve as much frequency response as possible. The slots were designed as 3/16-inch wide in order to retain as much frequency response as possible by minimizing the volume of the exit slot. 3/16-inch is the minimum possible slot width, since the smallest end mill with the 1.328 inch reach necessary to cut the slot is 3/16-inch in diameter. The center of the end mill is 1.876 inches from the centerline at the outer end of the cut. At the inner end of the cut, a one-quarter inch end mill is used to increase the width of the slot to allow the hole in the rotor to fully open when they are aligned at maximum injection. The center of the one-quarter inch end mill is 0.867 inches from the centerline at the outer end of its cut and 0.717 inches from the centerline at the inner end of the cut.

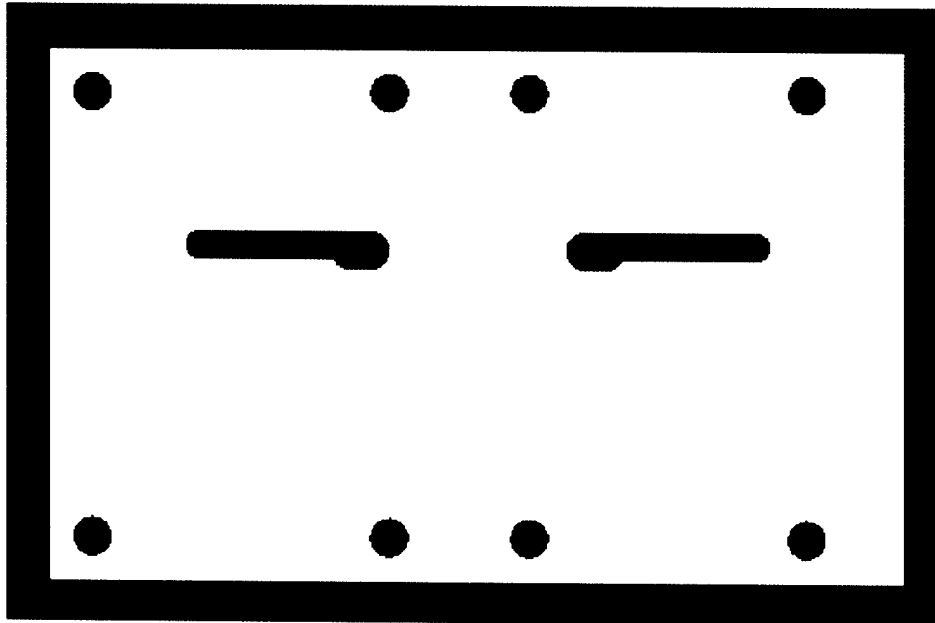


*Figure 2-15: Bottom of Rotary Valve Body*

Next, the round chamber for the rotor was cut into the valve body. The center of the holes is placed such that holes on the rotor will perfectly align with each ejection slot at the same time. In order to provide the proper spacing, the center of the round chamber is set 0.702 inches from the straight edge of the ejection slots. The chamber consists of four concentric holes. The first hole is 0.986 inches in diameter and extends through all but the last 0.100 inch of the valve body. This ensures it passes through the entire transfer channel while providing a tight clearance around the 0.9843 inch diameter rotor shaft in order to minimize leakage flow. The second hole is 1.40 inches in diameter and 1.646 deep. It is a bearing shelf 0.005 high that allows the bearing to compress to the appropriate preload as the valve is closed. The third hole is 1.8504 inches in diameter and 1.641 inches deep. It is intended to slide fit a Torrington Fafnir 2MM9105WI-DUL Superprecision ball bearing capable of operating at a DN of 1,000,000 mm x RPM when it is grease packed (the actual DN must be scaled up by a factor of 1.3 to account for the small size of the bearing) [12]. The bearing is at a DN of 390,000 mm x RPM when it is creating a 2 kHz signal (25 mm inner diameter at 12000 RPM with an additional size factor of 1.3). The fourth hole is 2.001 inches in diameter and 1.169 inches deep. It is designed to be the inner surface of the round chamber the rotor spins in.

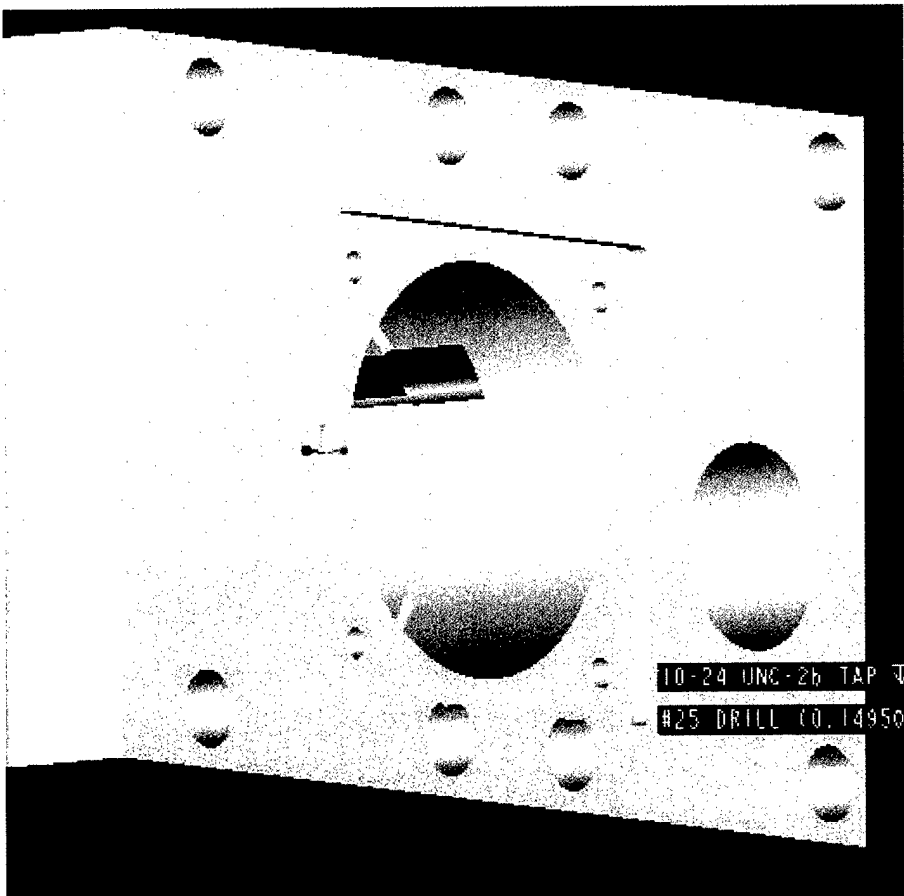


*Figure 2-16: Top of Rotary Valve Body*

Once the rotor chamber was defined, the recess for the top plate was created. The recess for the top plate is 2.400 inches wide and 2.300 inches high with a 1/16-inch radius in the corners. It is centered on the concentric holes with the longer dimension along the longer dimension of the valve body. It is 0.100 inches deep. There are threaded holes for 10-24 screws 0.95 inches from the centerline of the valve body and 0.90 inches forward and aft of the center of the concentric holes. The holes are 0.360 inches deep to prevent them from extending into the ejection chamber.

The air supply into the valve body is located 2.00 inches to the side and 0.222 inches forward from the center of the round chamber. This prevents interference between the motor driving the rotary valve and the air supply piping. The hole is 1.000 inch in diameter and extends through all but the last 0.100 inch of the valve body to ensure it

passes through the entire transfer channel. The top of the hole is threaded for a one-inch pipe fitting.

The transfer channel carries the air from the supply to the injection plenum inside the rotor. It is a slot one-quarter inch wide and 1.195 inches long. The center of the slot is offset 0.225 inches aft the center of the rotor chamber to prevent interference between the air supply and the ejection slots. The bottom edge of the slot is 0.100 inch from the bottom of the valve body, ensuring the structural integrity of the valve body without support for the bottom of the body. It is milled from the end of the body and then capped to prevent air from escaping from the valve.

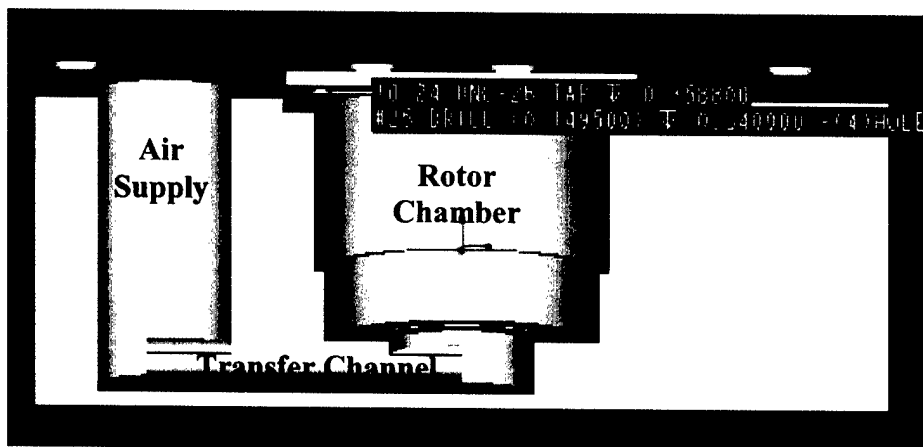
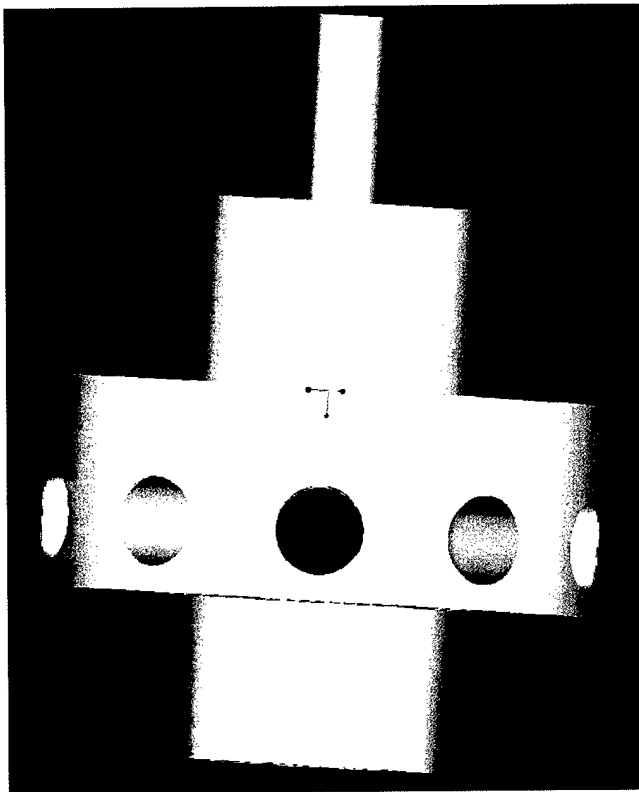


Figure 2-17: Cut-away View of Flow Path through Rotary Valve Body

### 2.6.2 Valve Rotor

The valve rotor is designed as a combination seal and air source. The rotor consists of six sections.



*Figure 2-18: Rotary Valve Rotor*

The bottom section is 0.9843 inches in diameter and 0.579 inches long. It is designed to slide fit into the bearing and extend another 0.107 inches to be nearly flush with the edge of the transfer channel. The extra length beyond the bearing creates a 0.001 inch gap between the valve body and the rotor that air can leak through.

The next section is a bearing shelf 1.30 inches in diameter that was designed as 0.002 inches high but expanded to 0.007 inches when the bearings seized in it during preloading.

The next section is the rotor disk, 1.997 inches in diameter and 0.740 inches thick (machined down from an original 0.750 inch thickness). The disk grows to 2.000 inches in diameter due to centrifugal loading at 2 kHz actuation. The 0.740 inch thick disk allows up to 0.568 inches to be used for vent holes in the rotor. 0.091 inches on each side must be maintained for structural integrity of the disk. The holes are placed at 36 degree spacing, allowing ten holes around the circumference. The holes are 0.3165 inches in diameter. This diameter yields and choking area 123% of the injector exit area. The flow through the vent

holes will experience a vena contracta, causing the effective area to be less than the actual area. A coefficient of discharge of 0.8 was assumed in order to offset the vena contracta effect.

Next is another bearing shelf identical to the first shelf.

Above the second shelf is another section 0.9843 inches in diameter designed to slide fit into the top bearing. It is 0.658 inches long, extending through the bearing and into the top plate.

The top section is 0.250 inches in diameter and 0.66 inches long. It has a dimple to allow a set-screw to join the motor shaft to the rotor via a flexible coupling. The set-screw dimple prevents the rotor from oscillating about the motor speed by preventing it from twisting with respect to the motor shaft.

The center of the shaft is bored out from the bottom to 0.80 inches in diameter. The bore is 1.29 inches deep to create the supply plenum inside the rotor.

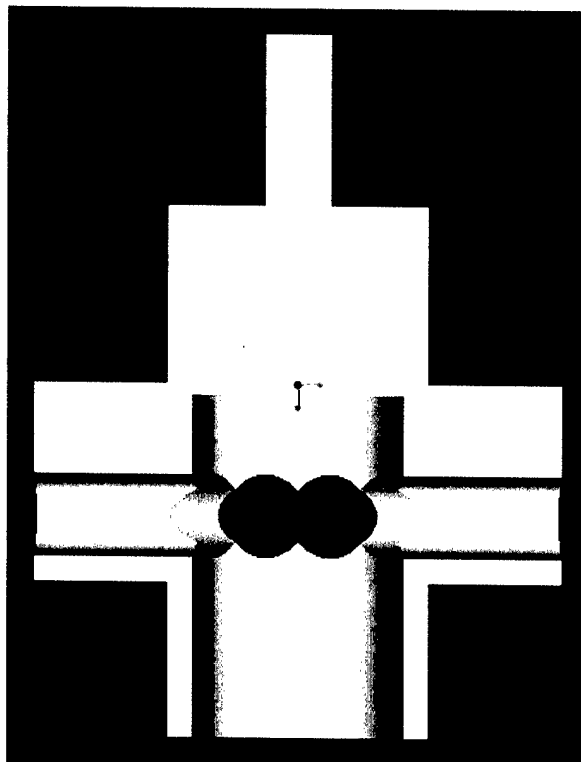


Figure 2-19: Cut-away View of Rotary Valve Rotor

### 2.6.3 Top Plate

The top plate seals the chamber and preloads the bearings when it is bolted to the valve body. The base is 2.398 inches wide, 2.298 inches high and 0.50 inches deep. The corners are tapered at a 45-degree angle for the last 0.10 inch of each side. This allows the top plate to fit easily inside the recess in the valve body. There are 0.140 inch diameter pass-through holes that match up with the bolt holes in the valve body. There is a circular protrusion 2.000 inches in diameter and 0.315 inches deep on the underside that fits into the rotor cavity. From this protrusion, three concentric holes are cut. The first is 1.8504 inches in diameter and 0.4724 inches deep to hold the top bearing. The second is 1.40 inches in diameter and 0.005 inches deeper than the first in order to provide a bearing shelf. The third is 0.991 inches in diameter and is a through hole to allow the motor brace to properly mount to the top plate. There are four 4-40 bolt holes located at 90-degree intervals 0.676 inches from the center of the through hole for the motor brace to bolt to the top plate. The top plate seals to the valve body by compressing a 2-034 O-ring in a channel 0.052 inches deep between circles of 2.254 and 2.082 inches in diameter, centered on the three concentric holes.

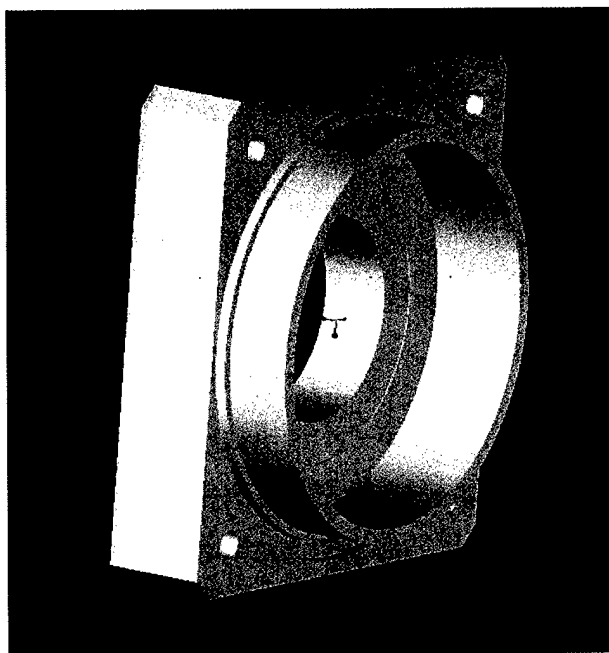
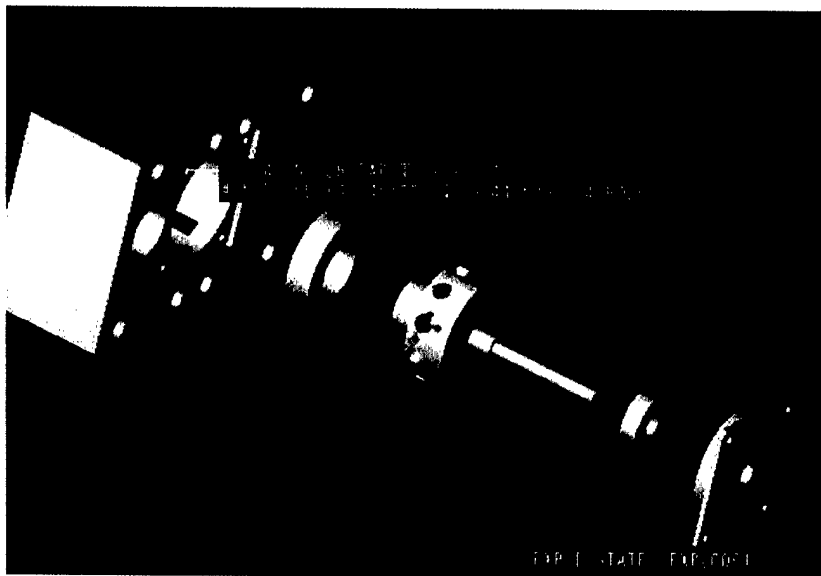
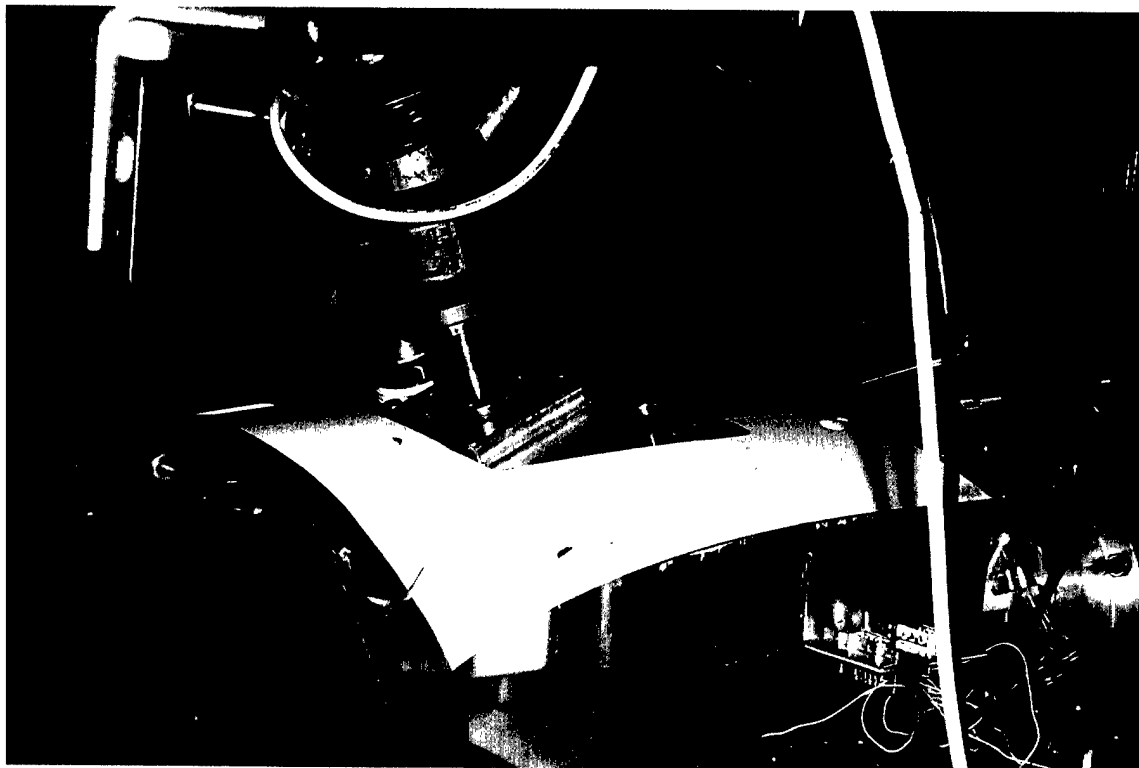


Figure 2-20: Bottom of Rotary Valve Top Plate

Figure 2-21 shows how all the parts fit together to form the rotary valve. Figure 2-22 shows the completed rotary valve assembled and mounted in the aircraft diffuser.



*Figure 2-21: Rotary Valve Components in Proper Arrangement*



*Figure 2-22: Rotary Valve Installed in Aircraft Diffuser*

Rotary valve performance below 50 Hz actuation frequency is sporadic as the motor cannot idle slowly enough to turn at a constant rate at such low speed.

## 2.7 Unsteady Total Pressure Probe

Bench testing started using a total pressure probe developed by Zachary Warfield [6]. It consisted of a six-inch tube with an XCQ-062-50G, 50 psi gauge pressure, Kulite pressure transducer mounted in a special fitting on the end. When used in the aircraft inlet, the probes have a natural frequency of approximately 1.5 kHz. However, when tested on the bench, the natural frequency was determined to be approximately 650 Hz (Figure 2-23). To be able to measure signals up to 2 kHz, a new probe was needed.

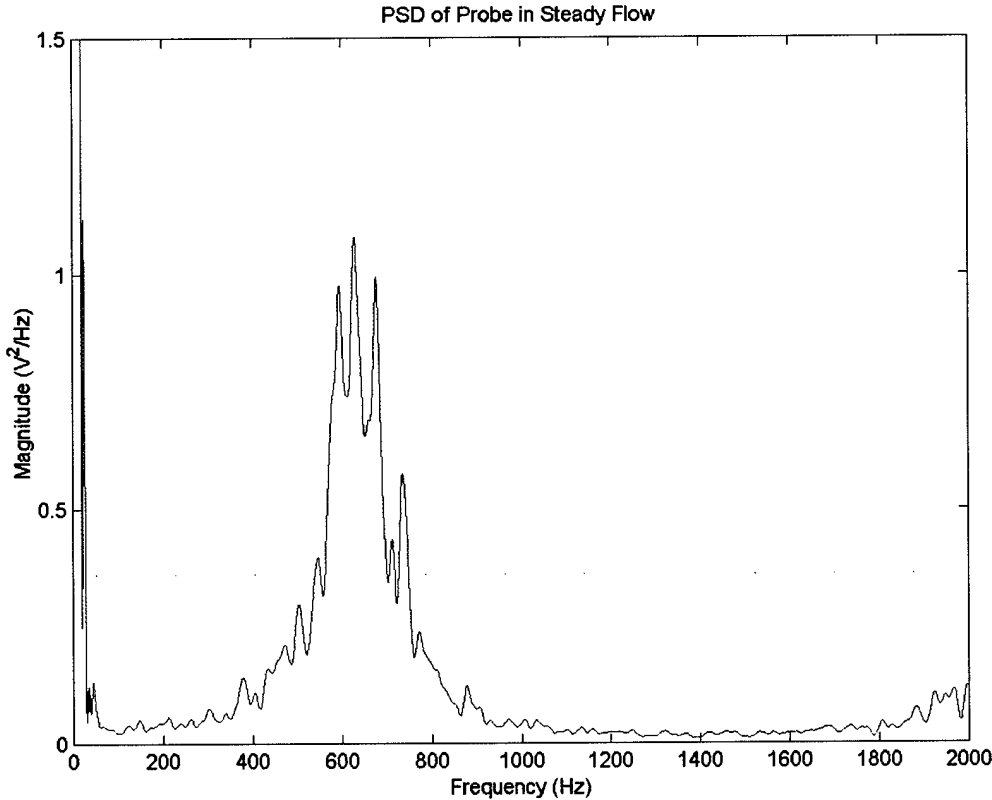


Figure 2-23: PSD of Warfield's Probe on Bench Mount

This new probe was designed to meet several requirements. The usable bandwidth was designed to allow measurement of signals to at least 2 kHz. The size was chosen so as to

not disturb the surrounding flow excessively. The probe was made structurally sound for Mach 0.70 flow in the 2D test section. It fits smoothly through the traverse slot in the test section to allow traverse of the flow while the test section is running. The desired reach of the probe is 4.040 inches upstream of the traverse slot. This matches the 0.64 inch location of the bench test.

In order to meet the 2 kHz bandwidth, the transducer must be very close to the flow. The duct length of a 2 kHz resonator is approximately 1.5 inches (Equation 2-3), assuming a quarter-wavelength resonance (corresponding to a duct with one end closed, the other end open).

$$L = \frac{\lambda}{4} = \frac{c_o}{4 * f} \quad (2-3)$$

For this reason, the Kulite transducer is mounted inside the probe, immersed in the flow. The ductwork leading to the Kulite is a 0.030 inch diameter duct 0.400 inches long that expands to 0.063 inches at the end of the duct. This expansion is to allow the flow to fully impinge upon the face of the Kulite. (The smallest Kulite transducer is 0.063 inches in diameter.) Calculations yield an acoustic natural frequency of approximately 7.8 kHz and a Helmholtz natural frequency of approximately 5.1 kHz (Equation 2-4) [13].

$$f = \frac{c_o}{2\pi} \sqrt{\frac{A}{L'V}} \quad (2-4)$$

To disturb the flow as little as possible, the head of the probe should grow at a five-degree angle to the flow [14]. Since the probe is designed to reach 4.040 inches upstream of the traverse slot, the five-degree angle was not a problem.

In order to fit through the traverse slot, the probe diameter was limited to 0.218 inches. The slot is 0.250 inches, but due to a 0.020 inch mismatch between the Plexiglas flow surface and the aluminum backing plate, the probe would seize in the traverse slot if it was larger than 0.230 inches. To keep construction simple, standard 7/32-inch outer diameter stainless steel tubing (one-quarter inch inner diameter) was chosen. If the probe proved to be too weak, a brace would be added between the head of the probe and the upright holding

it in the flow. After testing, the probe withstood flow up to Mach 0.76 without failing or deforming.

In order to get the probe into the test section and the Kulite into the probe, the probe was built in five stainless steel pieces. The first two are the tapered section at the head of the probe. These two sections allow visual inspection of the Kulite after it is installed. The nose cone is 0.675 inches long and contains the 0.030 inch diameter duct that opens into a 0.067 inch diameter hole that is 0.25 inches long that the Kulite mounts in. The Kulite is 0.350 inches long, allowing access to the last 0.10 inch of Kulite after it has been epoxied in place. The epoxy seal can be inspected, ensuring the integrity of the seal. The side of the piece tapers at a five-degree angle from 0.030 to 0.126 inches in diameter over the first 0.550 inches of the piece. The last 0.125 inches of the nose cone are cut to 0.093 inches in diameter to mount inside the second piece.

The nose cone is too small to fit inside the inner diameter of the tubing, so a second piece mates the two together. The second piece has a 0.093 hole running through the center. The sides taper at five degrees from 0.126 to 0.218 inches in diameter over 0.527 inches. After that, the last quarter-inch of the part is cut to 0.218 inches in diameter to mate inside the tubing.

The third piece is an extension from the rear of the tapered pieces to the upright holding them in the test section. It is 3.072 inches long and has a 0.2 inch notch bored out of the top and bottom sections at the rear of the piece to braise it to the upright and allow the Kulite installation.

The fourth piece is the upright. It is 10.0 inches long and is braised to the extension piece at the top and set-screwed to the base at the other end. The upright center is counter-bored for the bottom 2.0 inches to 0.180 inches in diameter to allow the temperature compensation barrel of the Kulite and the backpressure tube to sit inside the bottom of the upright.

The fifth piece is the base. It is 0.500 inches in diameter and clamps over the bottom 2.0 inches of the upright. It securely holds the upright via two set-screws. The wires from the

Kulite are soldered onto a LEMO connector mounted inside the bottom of the base. This protects the Kulite wires from being stressed and breaking. The backpressure tube exits the base through a separate hole next to the LEMO connector.

The following steps assemble the probe. First, braise the upright and the extension piece together. Thread the Kulite (with backpressure tubing attached) through the upright, extension and mating piece, then epoxy it into the nose cone. Once the epoxy sets and the seal is validated, epoxy the nose cone into the mating piece and the mating piece into the extension piece. When those set, add RTV into the exposed section where the extension piece and the upright are braised to prevent wind from blowing in and damaging the wires and tubing. Thread the backpressure tubing and the wires from the temperature compensator through the base piece, ensuring the backpressure tubing goes through its separate hole. Solder the wires to a LEMO fitting by GTL standard wiring procedure [15]. Place the temperature compensator inside the upright and draw all the wires through the base, then set-screw the base onto the upright. Gently coil the wires and place them inside the base such that the LEMO connector sits in place, flush with the bottom of the base. Set-screw the LEMO connector in place to complete the probe.

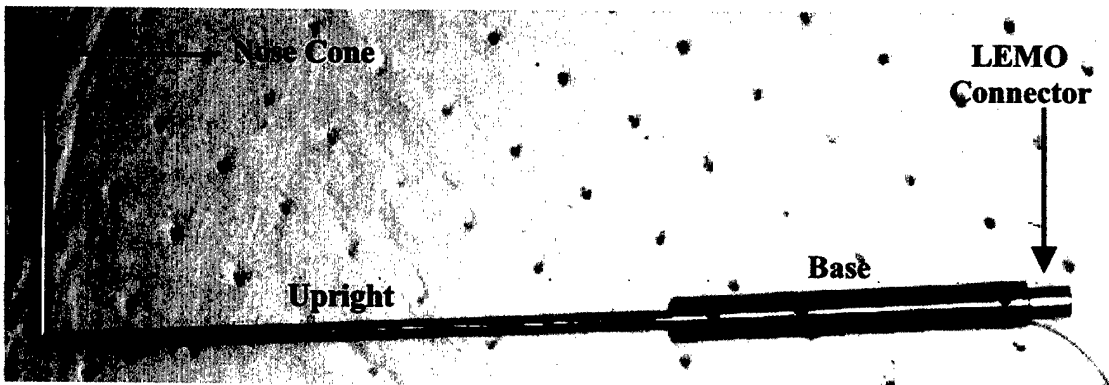
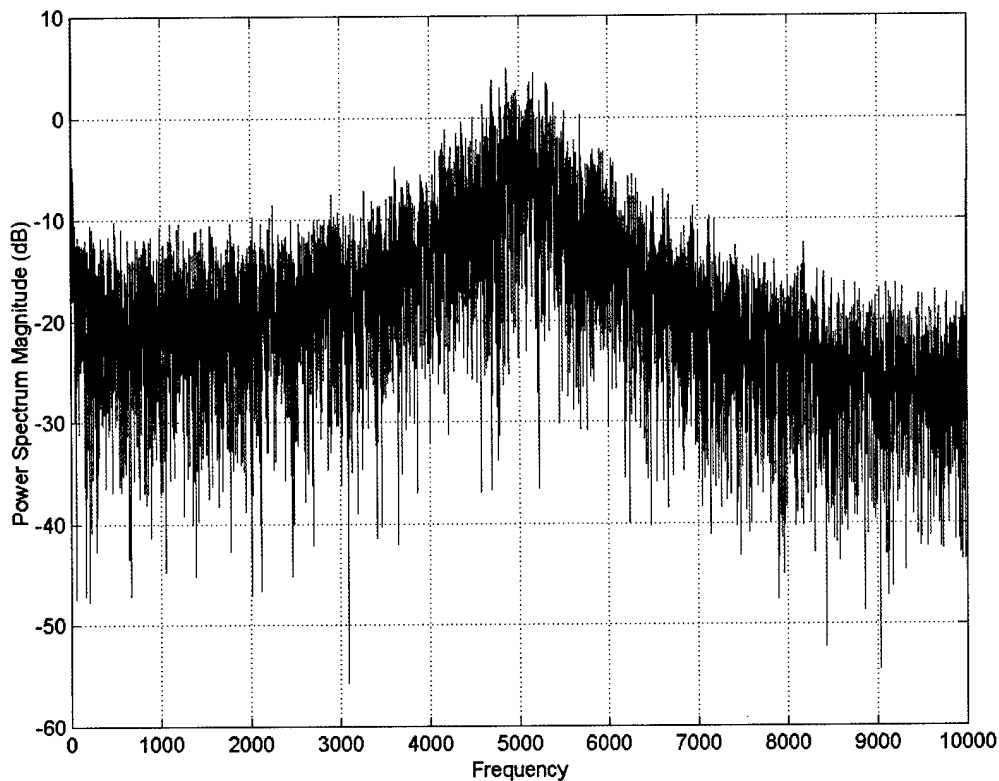


Figure 2-24: Completed Unsteady Total Pressure Probe

The Kulite used in the probe was a Model VCS-062-15G. It is a 15 psi gage transducer with a B screen across the Kulite face, Serial Number 4761-1A-121. The Kulite head is 0.067 inches in diameter. The sensitivity is 11.248 mV/psig at 15 VDC excitation. It is temperature compensated between 80 °F and 180 °F. The output impedance is 917 Ω, and the input impedance is 1999 Ω.

The completed unsteady total pressure probe was tested in the same bench test setup as Warfield's probe. The natural frequency was determined to be 5 kHz, guaranteeing the necessary signal resolution up to 2 kHz.



*Figure 2-25: PSD of Unsteady Total Pressure Probe on Bench Mount*



## **3 Bench Test**

### **3.1 Objective**

The bench test was designed to characterize the injection system before it was placed in the 2D test section or aircraft inlet tests. First, the injector was tested for span-wise uniformity during steady injection. Then the unsteady output at different frequencies and span-wise locations was measured.

### **3.2 Setup**

For this test, the actuator was fastened to the table using tube clamps around the air supply pipe. These clamps were mounted on threaded posts bolted through the bench top. The injector block was placed inside the flow separator bump. Vacuum tape<sup>1</sup> was placed around the ejection ports of the actuator. The bump was then bolted to the actuator, sealing the flow paths from the actuator to the injector block and firmly seating the injector block in place as the vacuum tape spread under the compressive force.

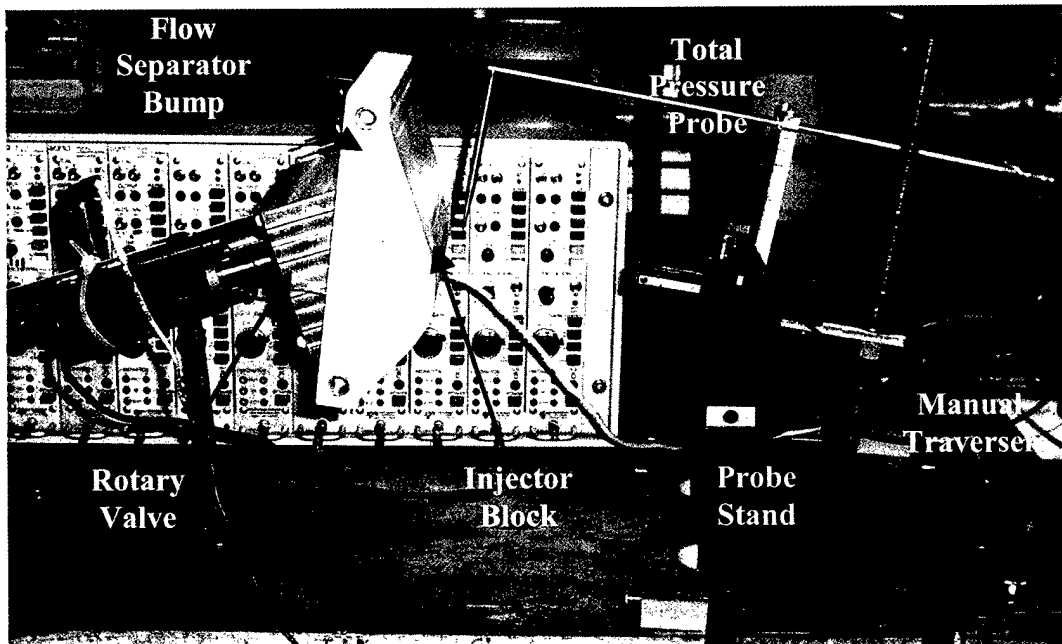


*Figure 3-1: Bench Test Setup*

The supply air came from a 100 psi compressor in the basement of Building 31. The air was compressed and dried, then stored in large settling tanks to eliminate perturbations and maintain air temperature during the test. The air passed through two valves when it arrived on the second floor of Building 31 where the test was conducted. It then passed through a particle filter, a pressure regulator and a flow meter with a thermocouple before entering the supply line to the actuator. Setting the regulator discharge pressure controlled the flow. This pressure combined with the flow meter and thermocouple readings was used to calculate the actual injection flow. The injection mass flow was calculated using Equation 3-1 (derived in Appendix A).

$$\dot{m} = 0.26708 (\% \text{ Flow}) \left( \frac{14.7 + P}{T_a + 460} \right)^{1.5} \left[ \frac{\text{lb}_m}{\text{sec}} \right] \quad (3-1)$$

It relates regulator pressure in psi (P), thermocouple reading in °F ( $T_a$ ), and flow meter reading to the mass flow through the injector.

Measurements were taken with a total pressure probe. The probe was mounted on a manual traverse that provided motion span-wise across the injection slot and through the thickness of the injection layer during each test. The traverse was mounted to a stand and locked in place by nuts on either side of the traverse mounting plate (Figure 3-2). The traverse could be moved vertically on the stand (corresponding to distance from the injector exit) between tests but not during a single test. The traverse has vernier measurement increments accurate to 0.1 mm. This allowed position accuracy of 0.1 mm for distance from the wall since the probe could be zeroed at each span-wise location to accommodate variation in the surface of the injector block and bump. The span-wise accuracy was 1 mm due to the height adjustment of the traverse mounting plate. When the traverse height was adjusted, the traverse was free to spin about the stand, introducing inaccuracy in the placement and alignment of the traverse with respect to the injector block and bump.

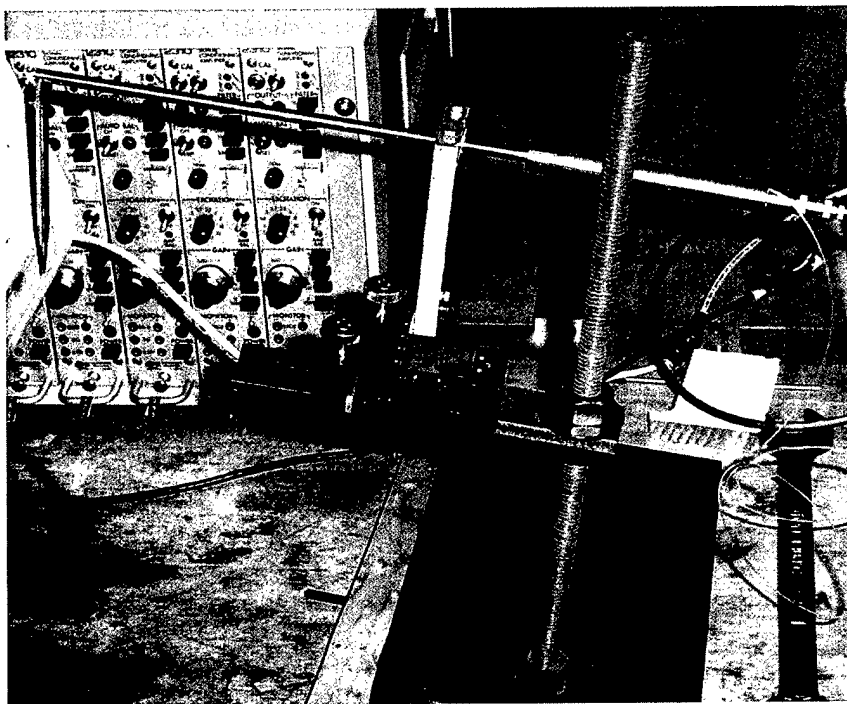


Figure 3-2: Total Pressure Probe on Probe Stand

### 3.3 Instrumentation

Two types of instrumentation were used in the bench tests. One set compiled steady data to verify span-wise uniformity of the injection flow. The other set measured the frequency- and location-dependent output of the injector under various operating conditions.

#### 3.3.1 Unsteady Instrumentation

Unsteady data was taken using the unsteady total pressure probe described in Section 2.7. The probe was connected to an amplifier. The amplifier was connected via a BNC cable to a data acquisition system.

To set and monitor the injection frequency, a Hewlett Packard Infinium oscilloscope was connected to an inductor placed in close proximity to the 16-tooth gear mounted on the motor of the rotary valve. The oscilloscope was set to calculate the instantaneous frequency of the teeth passing. This frequency was set to 1.6 times the desired actuation frequency (to account for the 16 teeth and the ten holes on the rotor). The oscilloscope

measurements would vary up to 40 Hz about an average value, partly due to variations in motor speed and partly due to the measurement procedure the oscilloscope uses. This led to differences between the desired and actual frequency of actuation. In general, the actual frequency was within 1% of the desired value. In all cases, the actual frequency was no more than 3% off of the desired value.

### ***3.3.2 Steady Instrumentation***

To take steady measurements, a total pressure probe and a 0-100 psia absolute Setra were used. The total pressure probe consisted of a 1/16-inch diameter tube to measure the flow. The tube was 1.6 inches long and had a 90° bend in the center. This tube was brazed into a 1.8 inch long, 1/8-inch diameter tube (Figure 3-3). A piece of flexible tubing ran from the end of the 1/8-inch tube to a 0-100 psia Setra. The Setra averaged pressure measurements to arrive at a value with 0.002 psia precision. The Setra has an "OK" indicator in the display to indicate when the displayed value is a reliable indication of the actual pressure (ie the variance of individual measurements is small enough to yield an accurate average reading). In very high injection flow conditions, the Setra was unable to measure an accurate average total pressure because of shocks present in the flow. In these cases, the investigator conducting the test manually averaged the values the Setra indicated. The precision of the recorded measurements reflected the amount of variation in the pressure readings.

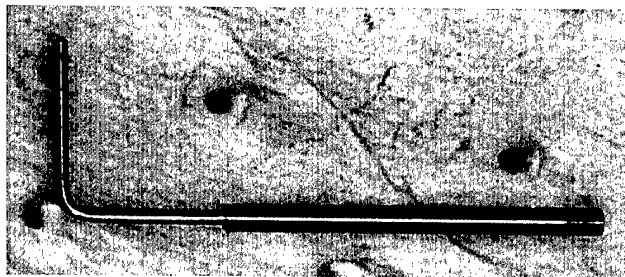


*Figure 3-3: Steady Total Pressure Probe*

## **3.4 Data Acquisition**

Two forms of data acquisition were used. Unsteady data was sampled with the unsteady total pressure probe, amplified and recorded on a PC. Steady data was sampled and averaged by the Setra and recorded manually in a lab notebook.

### ***3.4.1 Unsteady Data Acquisition***

The Kulite in the total pressure probe measured the total pressure. The signals from the Kulite were amplified by the signal conditioning amplifier and sent to the A/D board in the PC. The A/D board sent the information to a LabView VI (Virtual Instrument). The VI saved the information as an ASCII text file with a column vector of data for every channel of data taken.

#### **3.4.1.1 Hardware**

The hardware consisted of the unsteady total pressure probe, amplifier and a National Instruments PCI-6071E analog-to-digital data acquisition board. The total pressure probe is described in Section 2.7. The amplifier was a Vishay Measurements Group model 2310 signal conditioning amplifier. It output a differential signal up to ten volts in magnitude. This limitation led to different calibrations to prevent signal saturation depending on expected pressure measurements.

The National Instruments PCI-6071E A/D board was supported by two other components. The first was a 100 lead AT-MIO-64E-3 terminal block. It was mounted inside a case with 64 leads soldered to 32 BNC connections on the front panel of the case, providing up to 32 simultaneous differential measurements. The PCI-6071E board did not use the other 36 leads. A shielded cable, 182853C-01, transferred the data from the terminal block to the PCI-6071E in the computer.

The PCI-6071E is capable of measuring single-ended signals on 64 channels, or differential signals on 32 channels. The maximum sample rate is 1.25 megasamples per second over all channels. These tests were connected with the PCI-6071E measuring differential signals at a 20 kHz rate on at most two channels, well within the capability of

the board. The board distinguishes between signals at 0.005 volt increments, setting the accuracy of the data recorded using the board.

#### 3.4.1.2 Software

A LabView VI, “bench.vi” developed by Andrew Luers, triggered the data acquisition by the PCI-6071E when commanded by the investigator. The VI commands the card to acquire a number of samples from specific channels and then report the results back to the VI. The VI then places the data in an array of column vectors, one column for each channel. The data is saved in ASCII format in a text file. The data sampling rate was 20 kHz, ensuring ten data points per cycle at 2 kHz for waveform resolution. In most tests, data was taken for 0.5 seconds, capturing 25 cycles at 50 Hz up to 1000 cycles at 2 kHz.

#### 3.4.2 Steady Data Acquisition

For the steady data, the probe was moved to the desired position. The investigator waited a short period of time (approximately one second) for the transients to subside. Then the Setra averaged the pressure reading and indicated the acceptability of the reading by displaying the “OK” symbol. The investigator recorded the value in a lab notebook. At high mass flows, the flow would expand supersonically after it exited the duct. This would cause a shock to develop between the injector exit and the probe. The shock strength varied significantly, causing large variations (up to 0.3 psi oscillations) in pressure measurements by the Setra. In these cases, the investigator averaged the pressure readings manually and recorded the value in the notebook, noting the precision of the value recorded by the amount of variation in the pressure reading.

### 3.5 Actuation System

Tests were conducted using two separate actuators. Steady injection used a steady plenum to deliver the air to the injector block. Unsteady injection passed the air through the rotary valve to produce the unsteady signal for the injection.

### 3.5.1 Steady Plenum

The steady plenum (Figure 3-4) is a collection of copper pipe fittings that provides air to the injector. The plenum takes the air in through a two-inch threaded pipe connection, reduces it to a 1 1/8-inch pipe, splits the flow through a specially made connector and delivers it to the inlets to the injector duct. The reduction in pipe size allows the steady plenum to be attached to the bench via the tube clamps and threaded rods described in Section 3.2. The cross section of the steady plenum also ensures the flow is relatively low velocity, minimizing flow losses upstream of the injector.

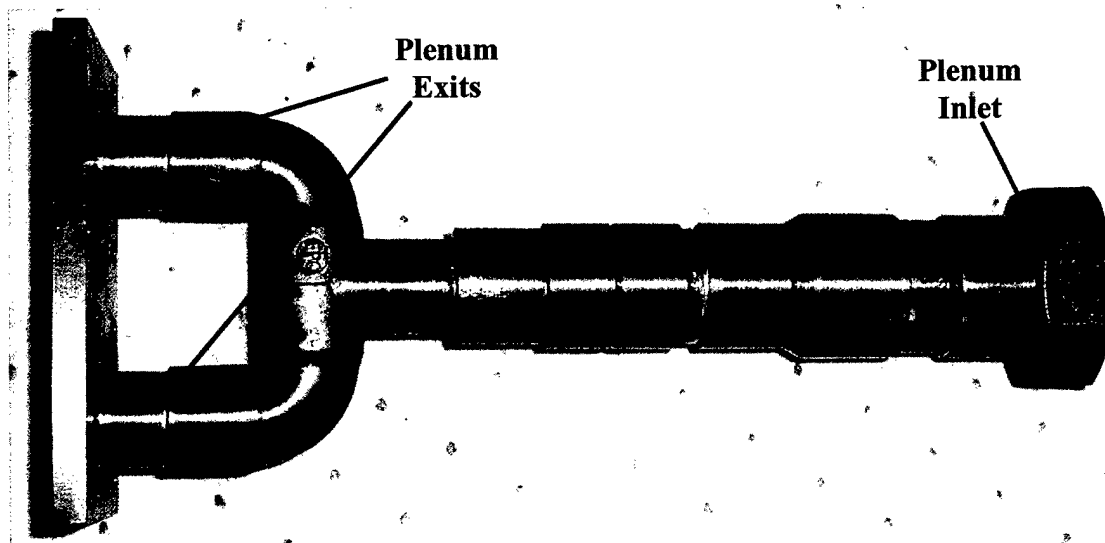
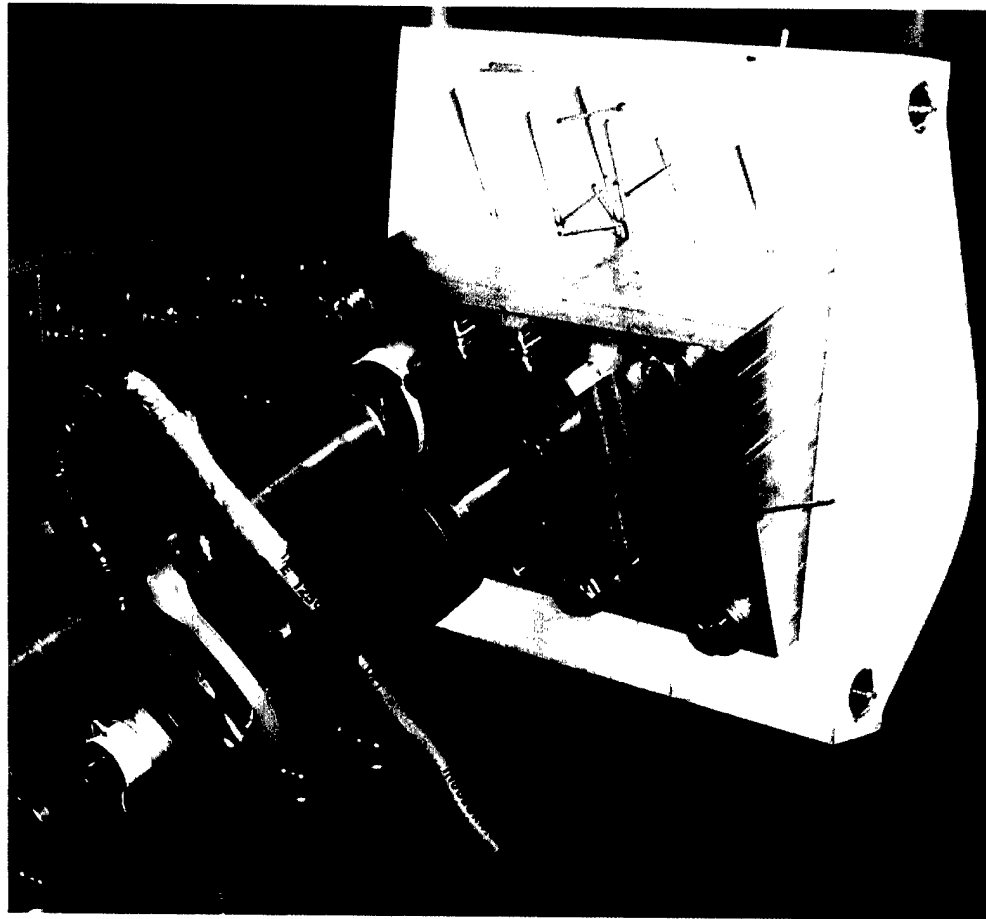


Figure 3-4: Steady Plenum

### 3.5.2 Rotary Valve

The rotary valve (Section 2.6) air supply mounts to the bench using the tube clamps and threaded rod described in Section 3.2. The valve body is cantilevered off the air supply, using torque on the air supply pipe to support the rotary valve, injector block and flow separator bump (Figure 3-5). This configuration allows the rotary valve to develop an oscillation in angular displacement about the center of the air supply pipe. Fortunately, this oscillation occurs at very low injection frequency and abates before the minimum tested frequency of 50 Hz.



*Figure 3-5: Rotary Valve Mounted in Bench Test*

### **3.6 Calibration**

The Kulite in the unsteady total pressure probe was calibrated before testing began each day. The calibration procedure was:

1. Allow the amplifier to warm up for at least 30 minutes with the excitation voltage off.
2. Turn the excitation on and allow the Kulite to warm up for 5 minutes.
3. While the Kulite is warming up, attach the foot pump and air tank to the Setra via the Swagelok fitting and the nose cone via the flexible tubing.

4. Allow the pressure inside the system to stabilize, then zero the Kulite output and record the Setra reading. Verify the Kulite is zeroed with the amplifier output fed into a voltmeter.
5. Pressurize the system to at least 1 psi overpressure.
6. Wait for the pressure to stabilize. Set the gain of the amplifier to the proper multiple of the difference between the current reading of the Setra and the initial reading. Lock the gain.
7. Bleed 25 - 50% of the overpressure out of the system via the bleed valve next to the air tank.
8. Allow the system to equalize pressure, then verify the Kulite output agrees with the Setra pressure difference.

## 3.7 Results

### 3.7.1 Steady Results

The injector block that was designed to eject a maximum of two percent of the inlet core flow was tested for flow uniformity across the span using steady injection flow. The results for two percent core flow injection and four percent core flow injection are plotted in Figures Figure 3-6 and Figure 3-7 respectively. These measurements were taken 0.16 inches (five slot widths) downstream of the injector exit. The measurements were taken in 0.5 mm increments through the injection sheet thickness and 5 mm increments along the sheet width. The total pressure probe head was centered 1 mm off the wall when the probe touched the wall, therefore the data points extend from 1 mm to 3 mm off the wall where the effect of the injection is negligible.

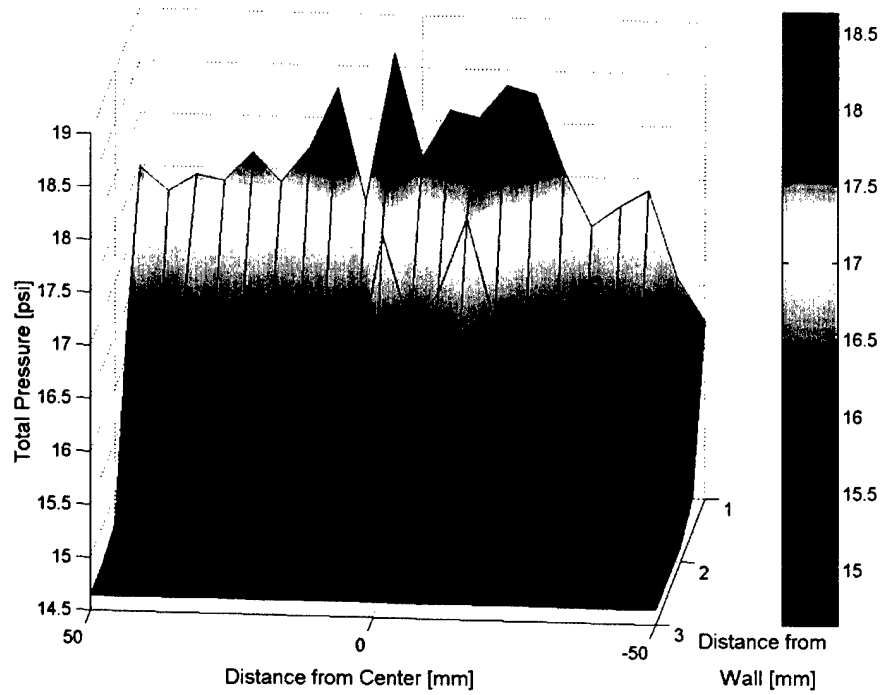


*Figure 3-6: Total Pressure Profile with 2% Core Flow Steady Injection*

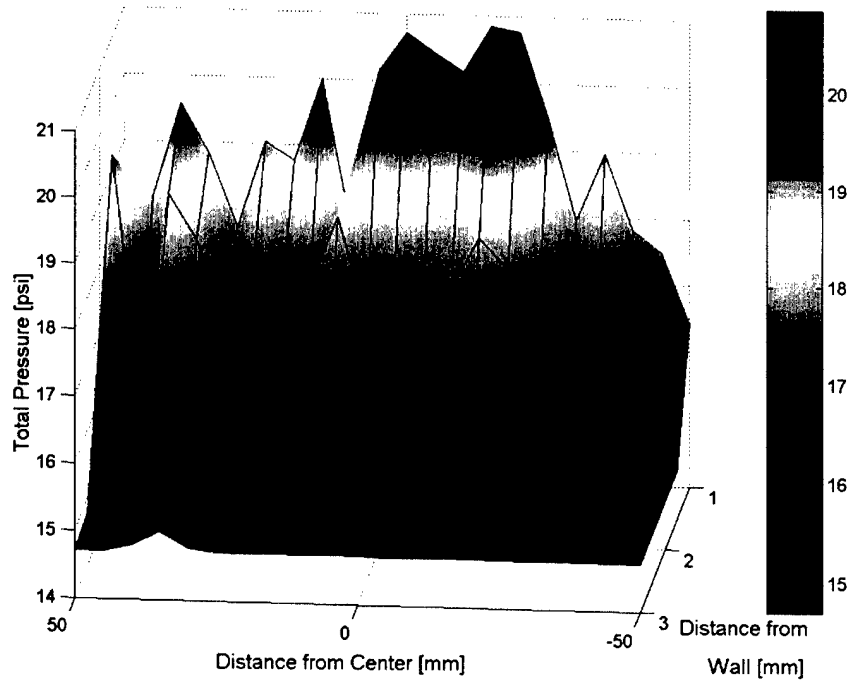


*Figure 3-7: Total Pressure Profile with 4% Core Flow Steady Injection*

In both cases, the span-wise uniformity was sufficient. The total pressure was highest in the span-wise range from -20 mm to the centerline. This higher pressure was due to the duct being slightly wider and smoother after sanding to remove a particle blocking the flow as described in Section 2.4. The range from -50 mm to -40 mm was lower than the corresponding positions on the opposite side since part of the flow from this lower pressure region was diverted into the higher-pressure region from -20 mm to the centerline.

These graphs also demonstrated that the injection flow was following the Coanda effect and remained attached to the wall as it rounded the turn immediately following the injector exit. If the flow was not attached to the wall, the peak of the pressure would have been approximately 1.6 inches from the wall. The total pressures were highest 1 mm from the wall, indicating that the flow turned.

### ***3.7.2 Unsteady Results***

Once the spatial uniformity was confirmed, the injector's unsteady performance was tested. The injector block that was designed to eject a maximum of two percent of the inlet core flow was bench tested with an average of 2.50 % core flow ejection. 2.50 % core flow was chosen to allow 1% steady offset for leakage flow and allow oscillations up to 4 % core flow. Measurements were taken in 5 mm increments from the centerline to 50 mm. All measurements were taken 1 mm off the wall, the location of the highest total pressures in the steady bench tests. The measurements were taken 0.64 inches downstream of the injector.

The data was then reduced in Matlab using a least squares fit to an offset and sine and cosine functions of a single frequency. The data reduction m-file, maxamp.m, can be found in Appendix A.

The total pressure amplitude at each span-wise location is plotted versus actuation frequency in Figure 3-8. Figure 3-9 plots the average maximum and minimum total pressure as well as the average offset total pressure.

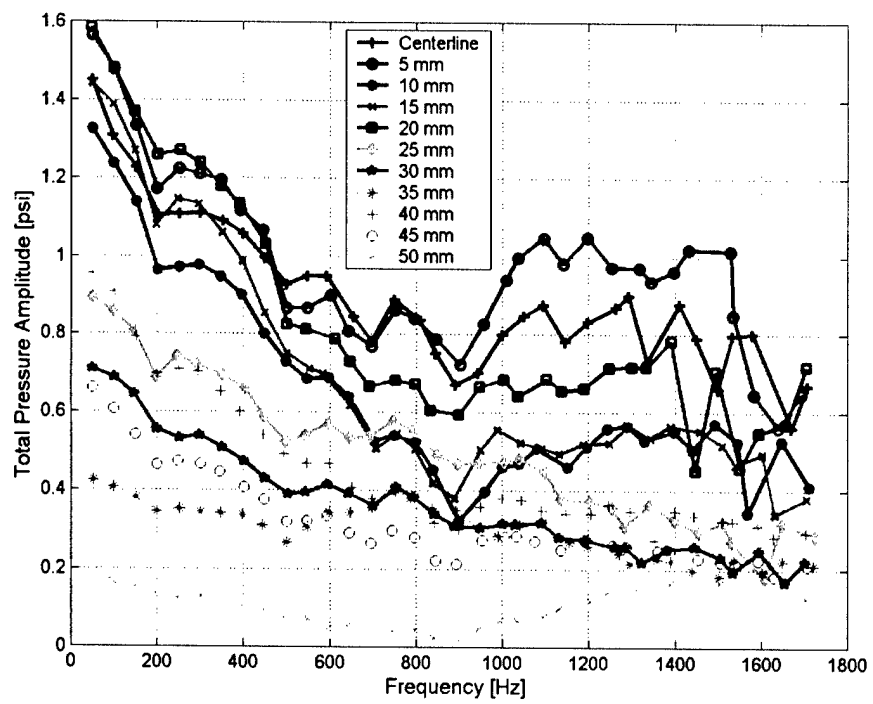


Figure 3-8: Total Pressure Amplitude Peak to Peak vs Actuation Frequency and Spanwise Location

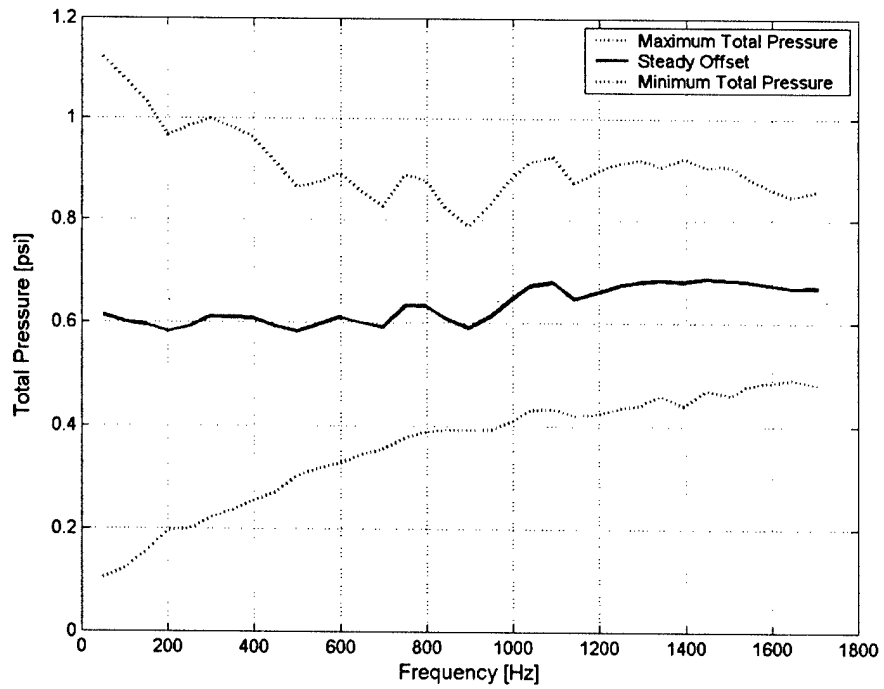


Figure 3-9: Average Total Pressure Oscillation Envelope and Offset

It is evident from Figure 3-8 that the flow at the edges of the duct is different from the flow at center of the duct. One possible explanation for this difference is that losses at the edge of the duct were worse, causing the signal to damp out more at the sides of the injector. Another possibility is that the flow was mixing with the air at the edges of the injected sheet more than at the center of the injected sheet.

In order to non-dimensionalize the injection conditions and investigate the roll off at the edges of the sheet, unsteady total pressure measurements were taken at the exit of the duct. The unsteady total pressure probe head diameter is approximately the width of the exit slot, allowing only one measurement position at each span-wise location. Tests were conducted at 5 mm increments from the centerline out to 50 mm at 13 psi supply pressure. Tests were conducted at 10 mm increments from the centerline out the 50 mm at 15, 19, 23 and 28 psi supply pressure.

The data was reduced using an ensemble average and a Savitzky-Golay FIR smoothing filter. The maximum and minimum of the filtered data were taken to be the maximum and minimum of total pressure.

The maximum and minimum total pressures were then converted into  $C_\mu$ . First, the total pressures were converted into Mach numbers using Equation 3-3 where  $P_T$  is the total pressure and  $P_s$  is the static pressure at the exit.

$$M = \sqrt{\frac{2}{\gamma-1} \left[ \left( \frac{P_T}{P_s} \right)^{\frac{\gamma-1}{\gamma}} - 1 \right]} \quad (3-2)$$

The Mach numbers were used to determine velocities using Equation 3-4 where  $T_T$  is the total temperature of the injection flow.

$$V = M \sqrt{\gamma R \frac{T_T}{1 + \frac{\gamma-1}{2} M^2}} \quad (3-3)$$

The injection air density is determined from ambient pressure and exit Mach number (Equation 3-5).

$$\rho = \frac{P_s}{R \left( \frac{T_T}{1 + \frac{\gamma - 1}{2} M^2} \right)} \quad (3-4)$$

The injector exit area,  $A_{inj}$ , was 0.128 square inches (4 inch span and 0.032 inch width). The core flow through the inlet during cruise (3.1 lbs/sec scaled) is at  $M = 0.65$ . This Mach number is used to determine the velocity and density of the flow using Equations 3-4 and 3-5. The separation area in the full-scale inlet is estimated to be 0.25 square meters. This scales to a separated area,  $A_s$ , of 0.0069 square meters or 10.764 square inches in the 1/6 scale inlet. These values were used to calculate  $C_\mu$  for the injector at each location and pressure ratio (supply pressure versus exit static pressure) using Equation 3-6.

$$C_\mu = \frac{\rho_{inj} A_{inj} \langle v_{inj}^2 \rangle}{\rho_{core} A_s V_{core}^2} \quad (3-5)$$

The results were then averaged across the injector. The average  $C_\mu$  for each pressure ratio and actuation frequency is plotted in Figure 3-10 and Figure 3-11.

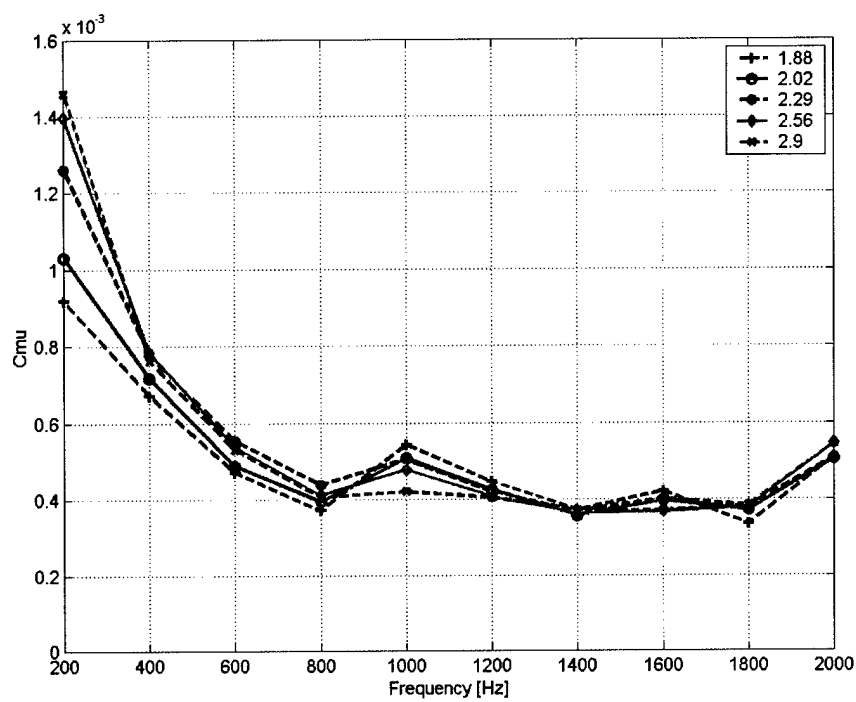


Figure 3-10:  $C_\mu$  vs Frequency and Pressure Ratio

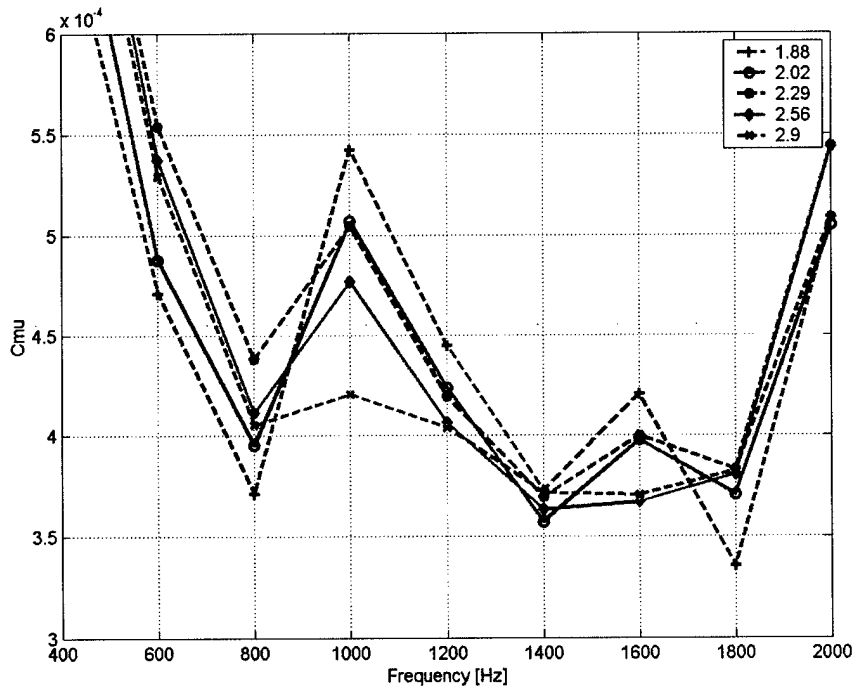


Figure 3-11:  $C_\mu$  vs Frequency and Pressure Ratio Above 400 Hz

The higher  $C_\mu$  values at low and high frequencies were largely due to higher maximum velocities indicated by higher maximum total pressure than in middle frequencies (Figure 4-12).  $C_\mu$  was highest at low frequency because the minimum velocity is lower than in middle and high frequency cases.

$C_\mu$  was relatively insensitive to pressure ratio because the larger pressure oscillations at high frequencies were offset by the higher mean total pressure as follows. If one holds static pressure constant, increasing total pressure amplitude at a fixed mean total pressure results in higher velocity oscillations. However, if mean total pressure increases, the velocity oscillation for a given total pressure amplitude decreases due to the larger average dynamic pressure (since dynamic pressure depends on the square of velocity). Since higher supply pressure increases both total pressure amplitude and mean total pressure (Figure 3-12 and Figure 3-13),  $C_\mu$  values calculated from the oscillatory velocity component remain roughly constant as pressure ratio increased across the actuator and injector.

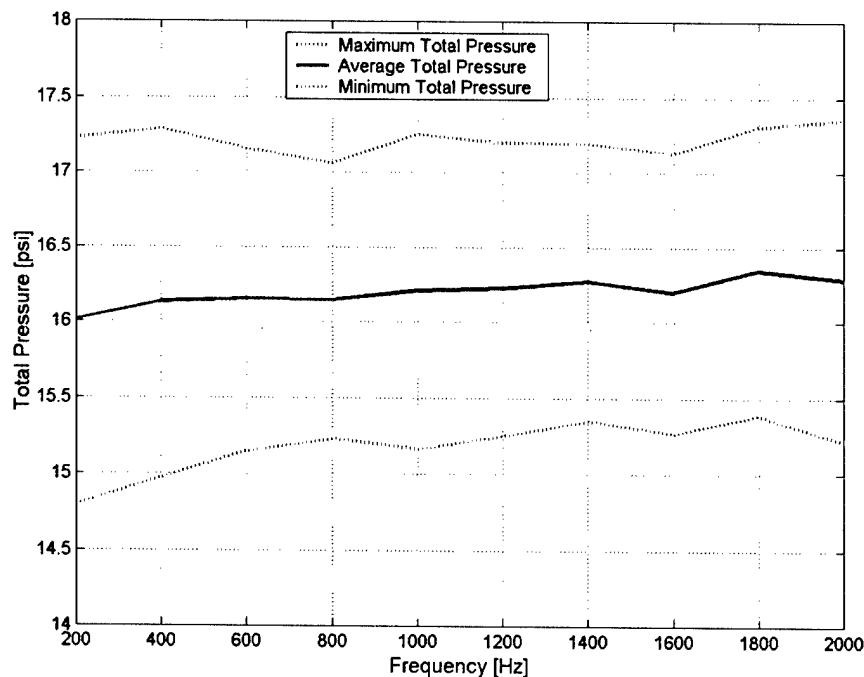


Figure 3-12: Total Pressure Envelope at 2.02 Pressure Ratio

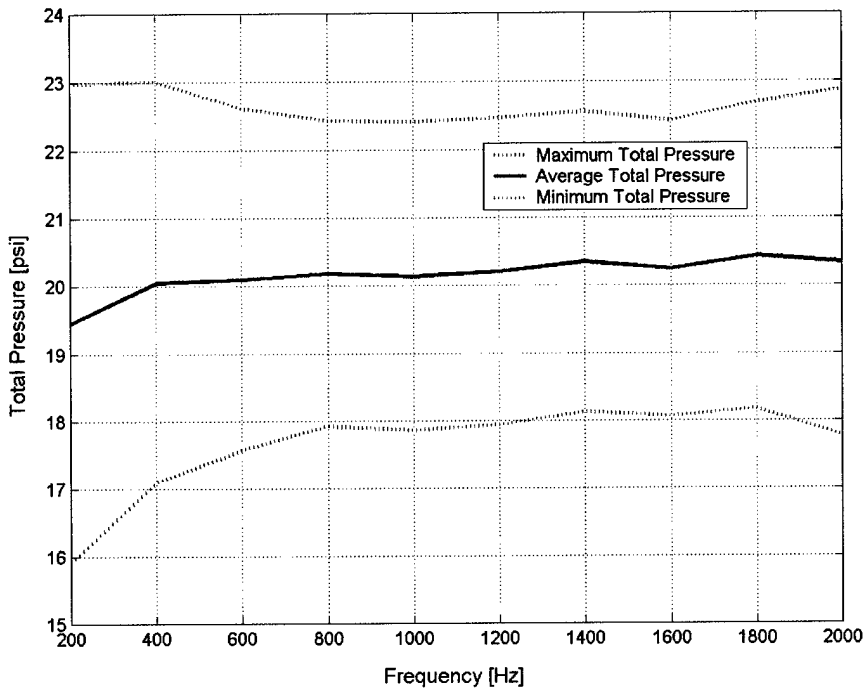


Figure 3-13: Total Pressure Envelope at 2.9 Pressure Ratio

The behavior of  $C_\mu$  at pressure ratios up to 4.1 was investigated at 2 kHz actuation frequency. At pressure ratios above 3.4, the injection jet chokes at the injector exit during the cycle peak. This caused a bow shock in front of the probe, altering the total pressure the probe measured. The total pressure loss due to the bow shock appears to be negligible. The maximum exit Mach number was approximately 1.19, resulting in a 0.63% loss in total pressure across the shock. To convert the calculated  $C_\mu$  based on the supersonic flow into actual conditions at the choking point in the injector exit, the flow properties were adjusted to equivalent flow at Mach 1 using isentropic relations. This resulted in a maximum increase in  $C_\mu$  of approximately  $3 \times 10^{-5}$  at 10 mm from the centerline and a pressure ratio of 4.1. When averaged across the span of the injector, the increase in  $C_\mu$  was less than  $1.5 \times 10^{-5}$ . Figure 3-14 shows the dependence of  $C_\mu$  upon the supply-to-exit static pressure ratio.

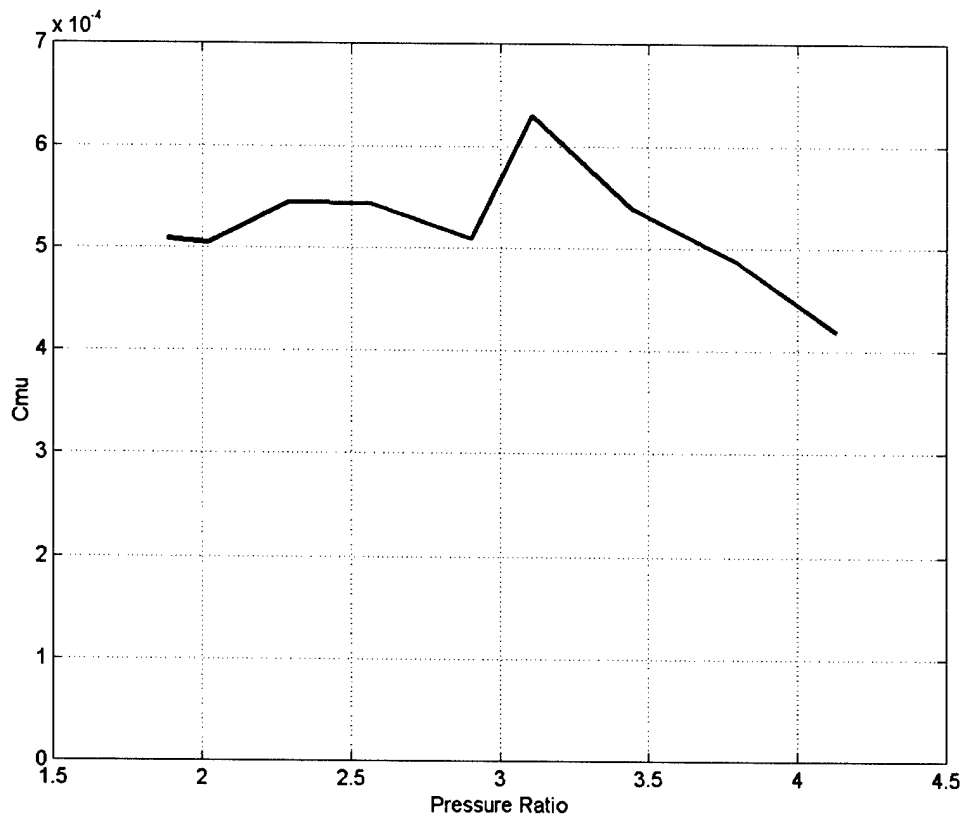


Figure 3-14:  $C_\mu$  vs Pressure Ratio at 2 kHz Actuation

$C_\mu$  remained constant with increasing pressure ratio. Once a pressure ratio of 3.5 was exceeded,  $C_\mu$  decreased slowly with increasing pressure ratio. The amplitude of the total pressure oscillations continued to increase, but the compressibility of the flow began to dominate. The large fluctuations in total pressure did not produce large changes in velocity. As the amplitude of the velocity oscillations dropped,  $C_\mu$  decreased as well. The  $C_\mu$  for a pressure ratio of 3.1 was abnormally high because the average total pressure at two of the data points was approximately 1.5 psi lower than at the other four points. This lower average total pressure caused the abnormally high local values of  $C_\mu$ , which increased the average  $C_\mu$ . Figure 3-15 plots local  $C_\mu$  versus span-wise location for pressure ratios of 2.9 and 3.1.

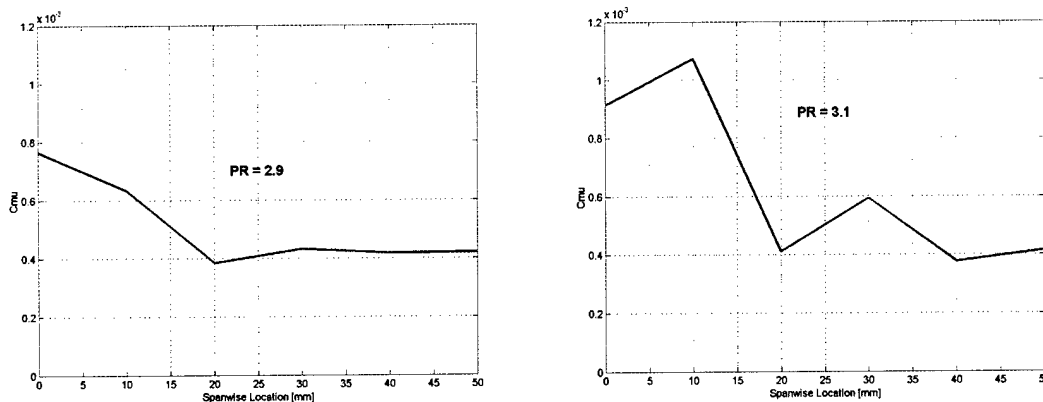


Figure 3-15:  $C_\mu$  vs Span-wise Location for Pressure Ratios 2.9 and 3.1

The steady  $C_\mu$  for injection at 2 kHz was calculated using the mean total pressure and Equations 3-2, 3-3, 3-4 and 3-6.

$$C_{\mu \text{ steady}} = \frac{\rho_{\text{inj}} A_{\text{inj}} \bar{V}_{\text{inj}}^2}{\rho_{\text{core}} A_s V_{\text{core}}^2} \quad (3-6)$$

Figure 3-16 demonstrates that steady  $C_\mu$  increased linearly with increasing pressure ratio.

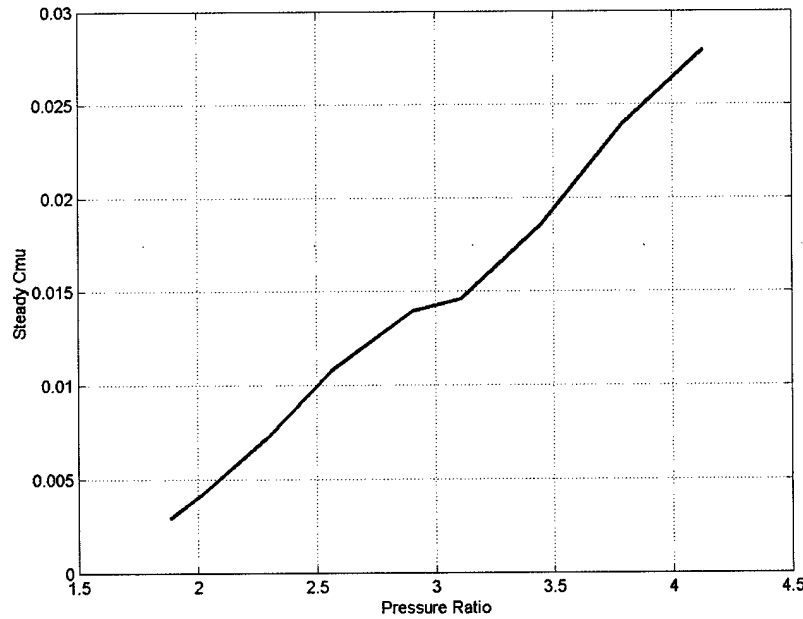


Figure 3-16: Steady  $C_\mu$  vs Pressure Ratio



---

## **4 2D Test Section Tests**

---

### **4.1 Objective**

The 2D test section tests were designed to simulate conditions in the tactical aircraft diffuser while allowing better access for measurements and flow visualization. The 2D test section also runs at a lower pressure ratio than the aircraft inlet, allowing the De Laval to run for longer periods of time before the oil temperature rises too high to continue testing.

### **4.2 Setup**

For this test, the 2D test section was mounted onto the inlet to the De Laval compressor with the removable sections on top of the test section (Figure 4-1). The flow separator bump was mounted in the first seven inches of the replaceable segments. The next thirteen inches were filled with the traverse plates and two Plexiglas inserts. The order of the traverse plates and Plexiglas inserts was changed to obtain difference axial measurement locations.

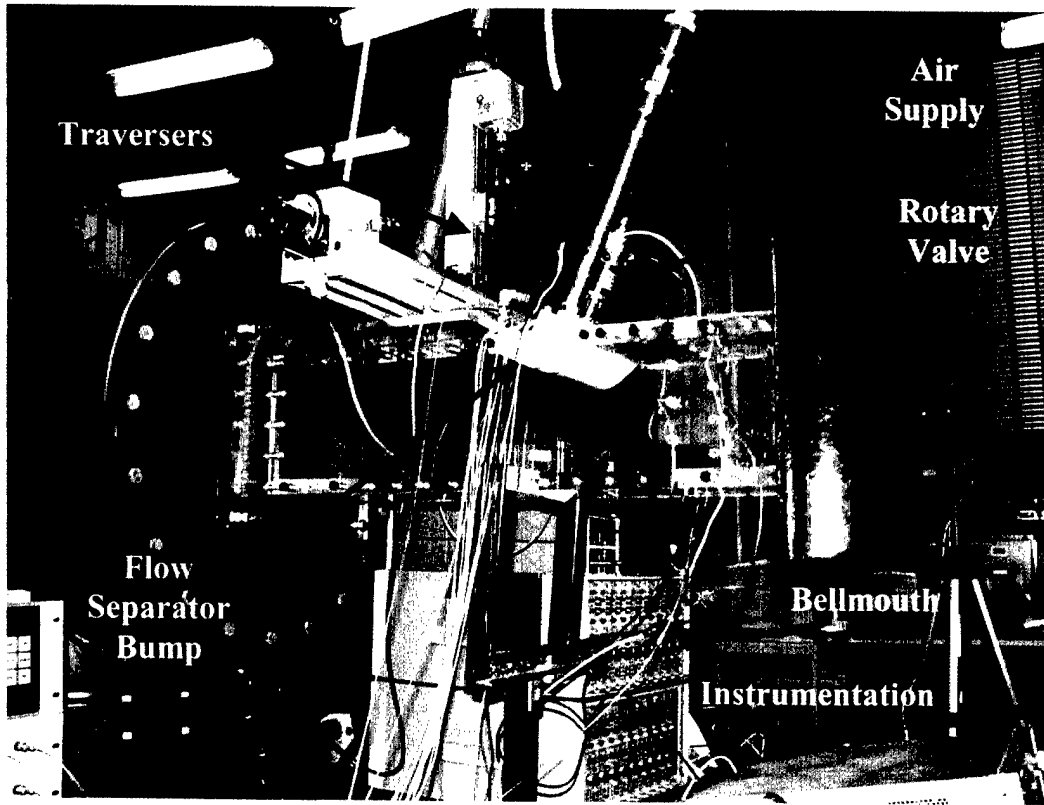


Figure 4-1: 2D Test Section Setup

The injector block was placed in position and the actuator was bolted to the bump, securing the injector block in place and sealing to it with vacuum tape as the bolts were tightened. In cases where no injection flow was applied, an aluminum plate was bolted to the backside of a blank injector block with vacuum tape between the two to press the injector block into position. The injection air came from the same source as listed in Section 3.2.

A three-foot traverse with a stepper motor driver was mounted to the aluminum backing plate, parallel to the slot to provide span-wise traverse capability. This traverse has 200 steps per turn with a 20 thread per inch screw drive for a total of 4000 steps per inch of traverse. This is equivalent to 157 steps per millimeter. A one-foot traverse with a stepper motor driver was mounted to the traverse plate, allowing vertical traverses into the test section. This traverse has 400 steps per turn with a 20 thread per inch screw drive for a total of 8000 steps per inch, equivalent to 315 steps per millimeter. A clamp for the unsteady total pressure probe is mounted on this traverse plate. The clamp consists of two

plates of aluminum with a hole 0.001 inch smaller than the diameter of the base of the probe drilled out between them. The hole creates a 1.7 inch long grip that prevents the probe from moving or twisting in the high subsonic flow.

An NF-90 controller runs the traverses. It can be controlled manually through a handheld control box or automatically through connection to a serial port. The initial location of the probe in the test section was set by hand. A LabView Virtual Instrument (VI) controlled the traverse while data was collected.

Measurements were taken at several distances from the separation line. These distances were measured along the 2D test section. The zero of these axial measurements is placed at the separation line. Figure 4-2 illustrates the geometry following the separation line (positive axial distances). The distance and height were normalized by the separation length and bump height respectively (see Section 4.7.2).

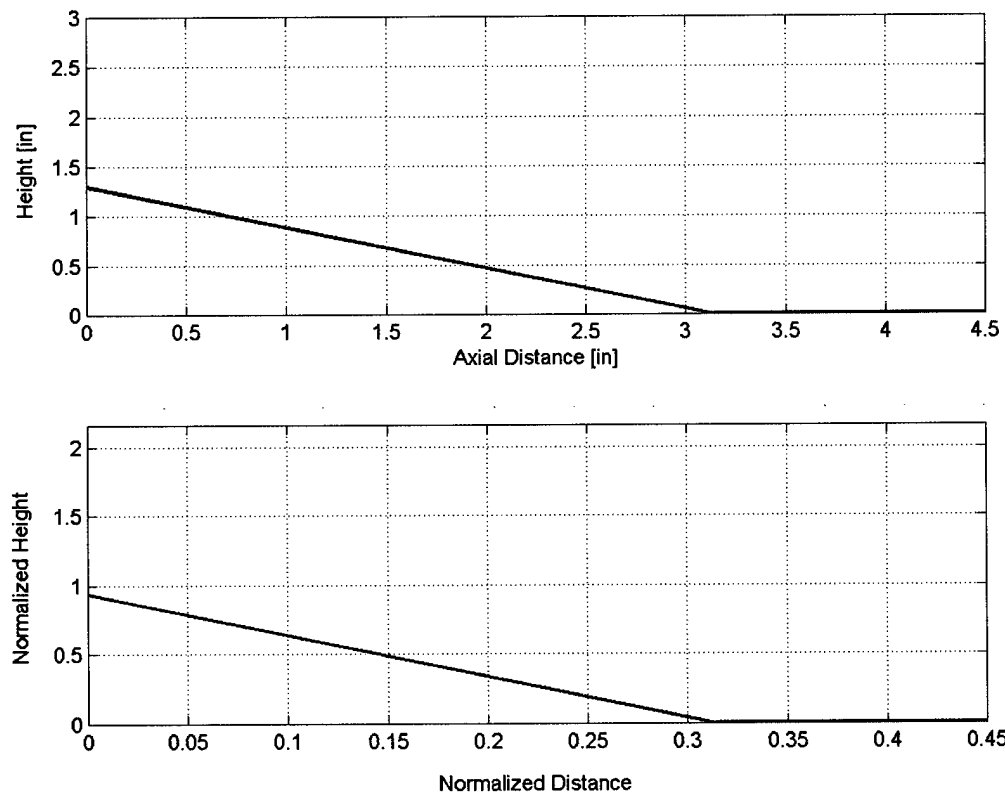


Figure 4-2: Geometry vs Axial Distance

## **4.3 Instrumentation**

In this test, the unsteady total pressure probe took measurements in the flow. Steady flow values were obtained by averaging the data taken by the probe. Unsteady data reduction could not be performed in real time. Steady static pressure taps on the flow separator bump measured the effect of injection on the wall to provide a real time measurement of the effect of the injection on static pressure in the separated region and provide an indirect indication of pressure recovery. The static pressure in the separated region is, to first order, inversely related to the severity of the separation. Stronger separations cause more total pressure loss, decreasing pressure recovery. Therefore, increased static pressure in the separated region indicates a weaker separation and, subsequently, improved pressure recovery.

### *4.3.1 Unsteady Instrumentation*

The unsteady data instrumentation was identical to the instrumentation listed in Section 3.3.1.

### *4.3.2 Steady Instrumentation*

The steady static pressure tap locations are described in Section 2.5. These taps were connected to a 48-port Scanivalve unit. The Scanivalve was controlled by the SDIU (Scanivalve Digital Interface Unit). The SDIU was triggered by a command from a data acquisition computer over a GPIB interface.

A Scanivalve scan was run when the De Laval compressor was operating at the desired run conditions to check the actual Mach number past the top of the bump. If the Mach number was not correct, the De Laval was adjusted to compensate. This iteration was repeated until the proper run conditions were achieved. While conducting the tests, scans were run at each data point.

## **4.4 Data Acquisition**

Both the unsteady and steady data were taken on computers for the 2D test section tests. One computer controlled the traverse and took the unsteady data. The other computer sampled the steady data when triggered by one of the investigators.

### ***4.4.1 Unsteady Data Acquisition***

The unsteady data was collected using “tunnel.vi”, created by Andrew Luers. This LabView VI automated the data collection by controlling the traversers, commanding the PCI-6071E board to collect data and saving the data to a text file.

#### **4.4.1.1 Hardware**

The unsteady total pressure probe is described in Section 2.7.

The PCI-6071E board is described in Section 3.4.1.1.

The traversers are described in Section 4.2.

#### **4.4.1.2 Software**

To set up the VI, the commands for the NF-90 were input on the front screen of the VI. The grid scan increments, both span-wise and radial, were input as the number of stepper motor steps. Corrections for the initial location of the probe were also input into the VI. The numbers of steps span-wise and radially were also set. These commands were of the form “C,I1M2000,R” which commands motor number 1 (span-wise in these tests) to move 2000 steps clockwise. The “C” tells the NF-90 that a command is coming. The “R” tells the NF-90 to execute the command. A time delay is built into the VI to account for the time it takes to traverse the commanded distance. This time delay was set manually in the VI and based on the 1000 step per second speed the stepper motors run at. This speed can be changed using commands to the NF-90, but 1000 steps per second was sufficient for the 2D test section tests.

If desired, the sampling rate and length could be altered in the diagram of the VI. For the purposes of these tests, the rate was always 20 kHz and data was taken for 0.5 seconds.

Once the test section was running at the desired conditions, the VI was configured and the probe was at the desired starting location, the “Go” button on the LabView VI could be pressed. Starting the VI initialized the serial port to the communications settings required by the NF-90 (1200 bits per second, 7 data bits, even parity, 2 stop bits and no flow control). It then sent an “F”, putting the NF-90 in remote control mode with no reply to commands. Then the VI moved the probe as prescribed by the two initial location correction commands. At that point, the VI would start the scan pattern: first moving one span-wise increment, moving the entire radial distance away from the wall, moving one radial step back in, then scanning the first data point. It would continue moving in and pausing to take data until it reached the closest point to the wall. Then it would move one span-wise step and traverse out to start another vertical scan. It progressed across the desired scan pattern in this manner until it reached the end of the pattern. When performing multiple scans during the same run, the initial movement was prescribed to translate the probe from one end of the scan pattern to one span-wise step offset from the starting position, to allow the VI to start the scan with the probe at the final data point.

The VI saves each data set to a separate filename. It has two integer counters that start at 0 and count up with each successive data point. One counter records the radial position and counts up as the probe approaches the wall. This counter is reset each time the traverse moves away from the wall. The other traverse records the span-wise position and counts up as the probe crosses the duct. For these tests, the counter started at the right side (facing into the 2D test section from the front) and counted up as the probe progressed to the left.

#### ***4.4.2 Steady Data Acquisition***

For the steady data acquisition, the Scanivalve sampled the static pressure taps on the command of the data acquisition computer via the SDIU. The command was issued by user input into scanmanw.exe.

#### 4.4.2.1 Hardware

The Scanivalve is a 48 port scanning unit that samples the ports by cycling the internal plumbing to connect each port to the single transducer. The pressure is allowed to equalize, then the transducer reads the pressure. The Scanivalve then steps to the next port and repeats the sampling process. It can be controlled manually using buttons on the front panel or automatically using either a serial port or GPIB connection.

The transducer is a 15-psi differential sensor. The backpressure on the transducer is normally vented to atmospheric but can be changed through a port on the left side of the unit.

#### 4.4.2.2 Software

The scanmanw.exe code commands the SDIU to step through the scanning cycle. The code prompts the user for current ambient conditions (pressure in psia and temperature in °F). It then homes the Scanivalve to port 0. When prompted by the investigator, the code sends the command to scan all 48 ports. It then retrieves the information from the Scanivalve and converts it into psia. The code also performs various calculations based on the data, but none of the calculations are useful for this test configuration.

The Scanivalve can read up to twelve ports per second. Scanmanw.exe sets the sample rate to two ports per second to allow sufficient time for the pressure at the transducer face to equalize before sampling the pressure. Similar codes have used up to four ports per second, but the tradeoff of speed versus accuracy dictated two ports per second for this project, as discussed in [6].

The code stores several sets of pressure data as it runs. When the investigator quits out of the program, it offers options to save the data in both .mat files for use in Matlab and ASCII text files for general use. The program is limited to at most fifteen scans before data sets become corrupted, but the investigator should not try to record more than thirteen sets in order to prevent data loss.

## **4.5 Actuation System**

The actuation systems are identical to the actuators in Section 3.5. In this test they were bolted to the flow separator bump.

The air supply hose was suspended from an eyehook in the ceiling to prevent the actuator and bump from carrying loads associated with holding the air supply in place above the test section (Figure 4-1).

## **4.6 Calibration**

The unsteady total pressure probe was calibrated according to the procedure listed in Section 3.6.

The Scanivalve is calibrated by the scanmanw.exe code as part of its startup procedures.

## **4.7 Results**

### ***4.7.1 Steady Results***

The first tests in the 2D test section used steady injection to determine the exit flow profile and compare to the steady bench test results in Section 3.7.1. The data was collected with the unsteady total pressure probe and then time-averaged. The probe traversed the flow 0.64 inches (20 slot heights) downstream of the injector in a grid pattern. The grid increments were 0.25 mm radially from the wall and 5 mm span-wise across the injection sheet. The data for each location was averaged to determine the steady total pressure. The results are plotted in Figure 4-3.

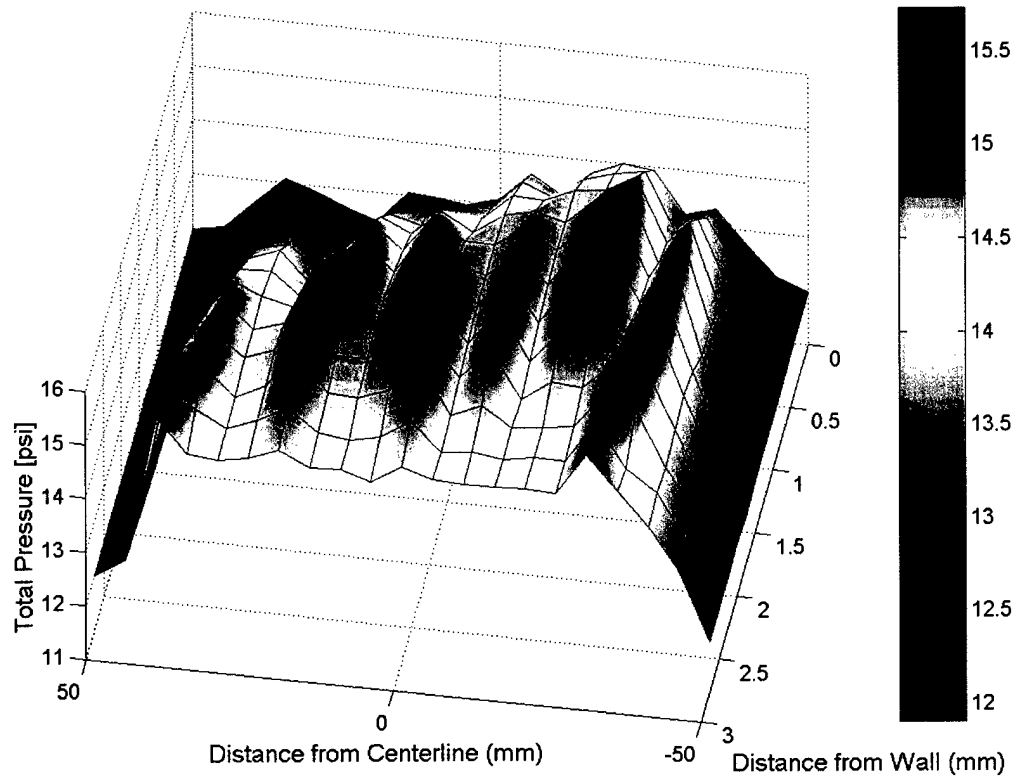


*Figure 4-3: Total Pressure Profile with 4.04% Core Flow Steady Injection in 2D Test Section*

The closest data point to the wall was 0.25 mm from the wall, because the center of the probe was 0.25 mm from the wall when the edge of the probe was resting on the wall.

The maximum total pressure is within 5 % of the mean for the center 80 % of the slot width. This level of uniformity was deemed adequate for further testing.. The flow separator bump and the traverser were misaligned slightly, causing the total pressure probe to contact the surface for the closest data point to the wall at -50 mm and the three closest data points at 50 mm. This angle caused the injection sheet to appear to lift off the wall on the positive side on the injector. Adjusting for this angle offset, the maximum total pressure lies between 1.5 and 2 mm from the wall. Since the total pressure decreased as the probe moved further from the wall (not shown in Figure 4-3), this maximum total pressure was the center of the injection jet. This indicated the flow exhibited the Coanda effect and rounded the turn downstream of the injector. If it had not turned, the highest total pressure would have been approximately 6.5 mm from the wall of the bump.

The region of higher total pressure was thicker than on the bench under similar injection flow (Figure 3-7). This indicated the injection sheet spreads more in the 2D test section than on the bench test. This thicker region also has lower values of average total pressure than on the bench test. The flow may have expanded to a larger thickness in filling in the lower static pressure of the separation bubble. The injection sheet may have also entrained more of the core flow from the test section, mixing at the edge of the sheet and spreading the higher total pressure further out into the test section.

#### **4.7.2 Unsteady Results**

Once the flow uniformity was verified, unsteady actuation tests commenced. In these tests, the unsteady total pressure probe traversed the flow and steady total pressure taps on the surface of the flow separator bump measured the wall static pressure in the separated region. A traverse of a single flow condition took up to ten minutes to run. A static pressure sweep took less than a minute. Initial tests were conducted primarily with the static pressure measurements. The results of these tests indicated the injection conditions that produced the best results. Unsteady total pressure traverses were then conducted at those injection conditions, to verify and quantify the pressure recovery improvement.

The static pressure measurements indicated that higher injection mass flow and higher frequency increased the static pressure in the separation bubble. In order to compare various data sets, the wall static pressure was normalized by the upstream static pressure and dynamic pressure ahead of the bump in the 2D test section. This normalized coefficient of pressure ( $C_p$ ) was calculated using Equation 4-1, using the pressure measurements at the upstream static pressure taps in the 2D test section as the reference condition. The dynamic pressure ( $q_{ref}$ ) was assumed to be the difference between the known total pressure (atmospheric pressure) and the measured static pressure ( $P_{ref}$ ).

$$C_p = \frac{P_s - P_{ref}}{q_{ref}} = \frac{P_s - P_{ref}}{P_{atm} - P_{ref}} \quad (4-1)$$

Figure 4-4 and Figure 4-5 show the dependence of the coefficient of pressure on injection mass flow at constant frequency. In Figure 4-5, frequency and distance are normalized by the approximate separation length, 10 inches, using Equations 4-2 and 4-3.

$$F^+ = \frac{f_{actuation} L_{separation}}{V_\infty} \quad (4-2)$$

$$\ell = \frac{x_{\text{axial}}}{L_{\text{separation}}} \quad (4-3)$$

The injection mass flow is normalized by 3.1 lbs/sec, which is the mass flow through the tactical aircraft inlet at cruise conditions. At low injection mass flows, the slope of  $C_p$  was shallow more than 2.5 inches downstream of the injector. As mass flow increased, this slope changed to a sharper slope at medium mass flows. At high injection mass flows, the slope was initially high but decreased at the end of the measured section. The slope between 3.14" and 4.14" actually became slightly negative at the highest injection mass flows. In general, increased injection mass flow increased the  $C_p$  calculated for the last three static pressure ports. This generalization breaks down at high injection mass flow when the  $C_p$  rises higher than  $C_p \sim -0.37$ . In those cases, the  $C_p$  increased to a maximum value at the static pressure port at the interface between the sloping face (on the back of the bump) and the test section wall, and then decreased at the last static pressure port. This implied that the flow had reattached to the bump and the highest value of  $C_p$  was due to streamline curvature away from the corner where the bump meets the section wall. Flow visualization tests (Section 4.8) confirmed this hypothesis accurately reflected the flow behavior.

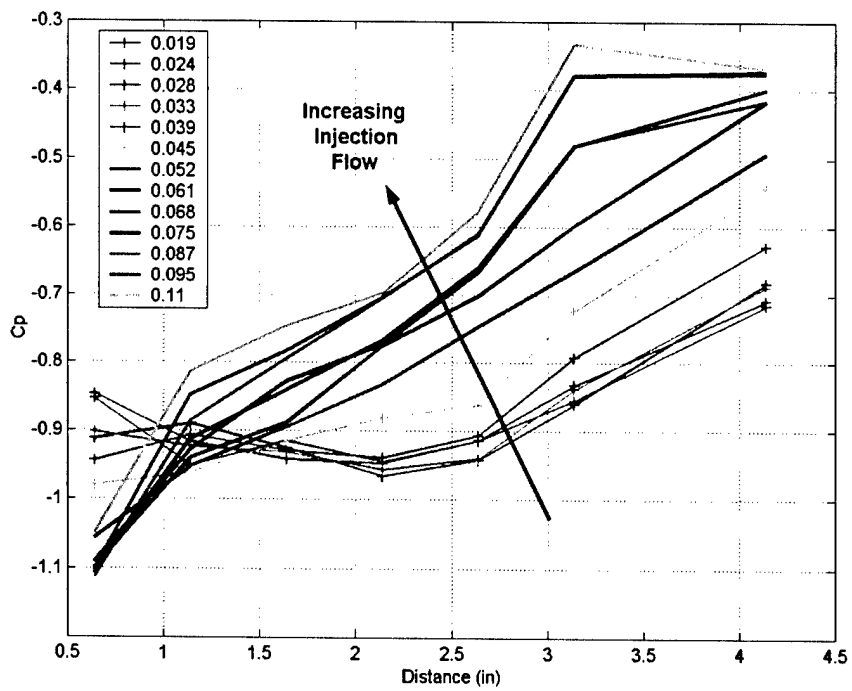


Figure 4-4:  $C_p$  vs Injection Mass Flow (1200 Hz actuation)

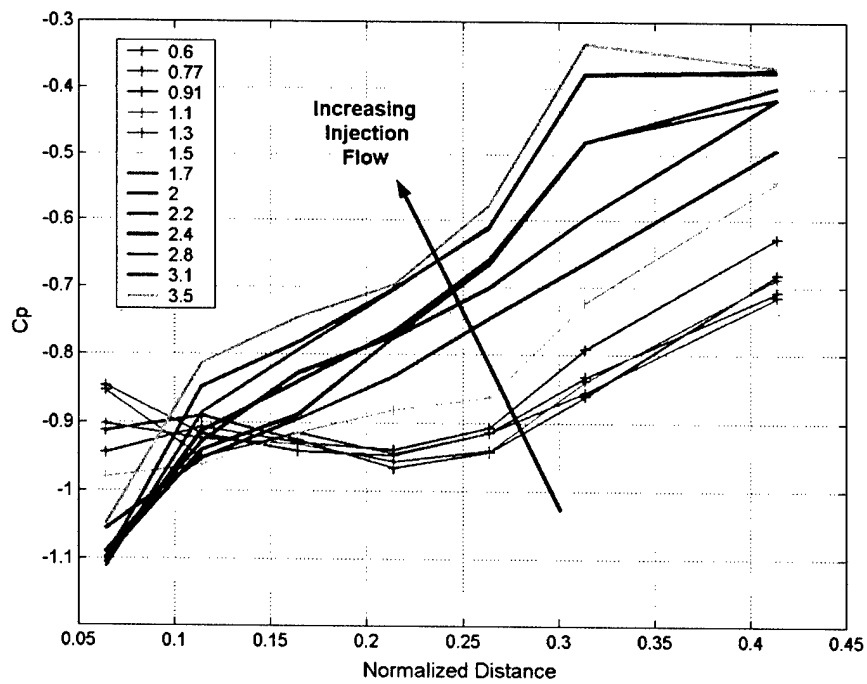


Figure 4-5:  $C_p$  vs Percent Injection Core Flow ( $F^+ = 1.37$ )

Figure 4-6 and Figure 4-7 shows the dependence of the coefficient of pressure on actuation frequency at constant injection mass flow. At low injection mass flows (0.018 lbs/sec or 0.60 % core flow) and at frequencies lower than approximately 900 Hz ( $F^+ = 1.03$ ), the slope of  $C_p$  was shallow throughout the measurement region. Above 900 Hz, the slope of  $C_p$  was much sharper, indicating that the severity of the separation bubble was lower at high actuation frequency. At higher injection mass flows, the dependence of the  $C_p$  profiles decreased on actuation frequency decreased. The higher injection mass flow made the separation insensitive to actuation frequency.

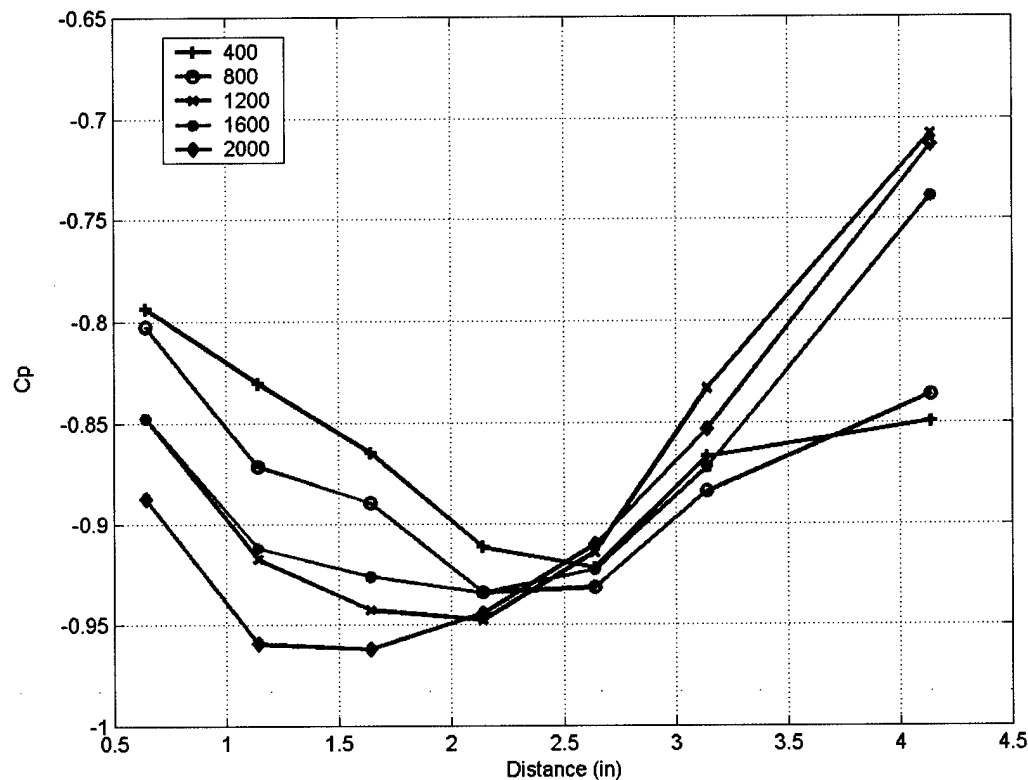
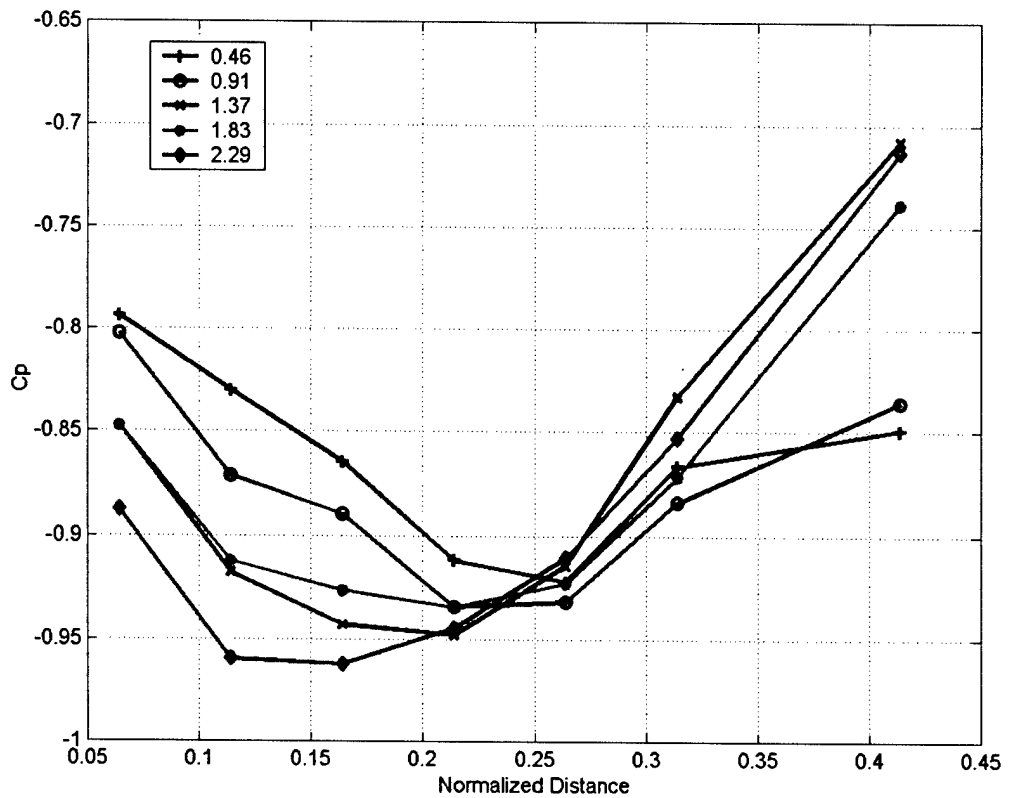
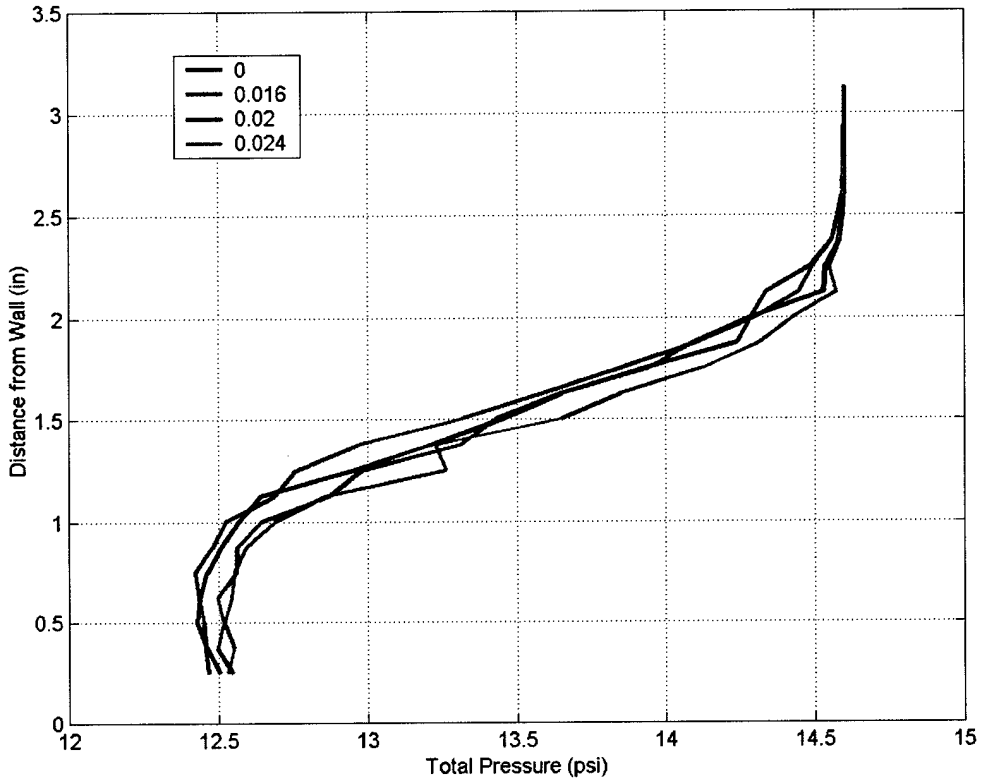


Figure 4-6:  $C_p$  vs Actuation Frequency (0.018 lb/sec injection mass flow)



*Figure 4-7:  $C_p$  vs  $F^+$  (0.60 % Core Flow)*

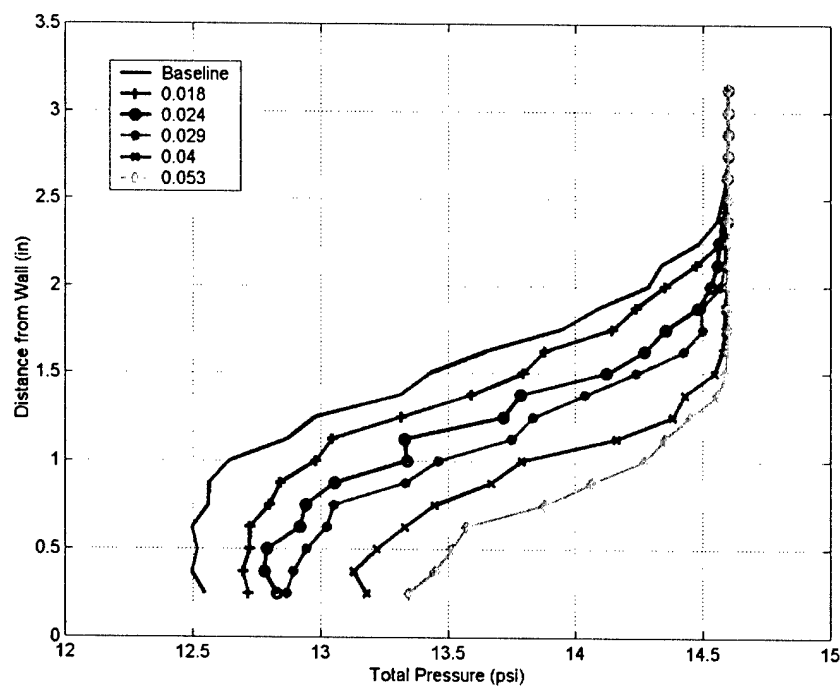
Vertical total pressure traverses were conducted along the centerline of the 2D test section to verify the implications of the static pressure profiles. The first traverses covered the span-wise centerline from 0.25 inches from the wall out to 3.125 inches from the wall at a location 3.64 inches downstream from the injector. Figure 4-8 shows the effect of steady injection at low mass flow. The injection mass flow is listed in lb/sec in the legend. The steady injection changes the total pressure profile only slightly at low injection mass flows.



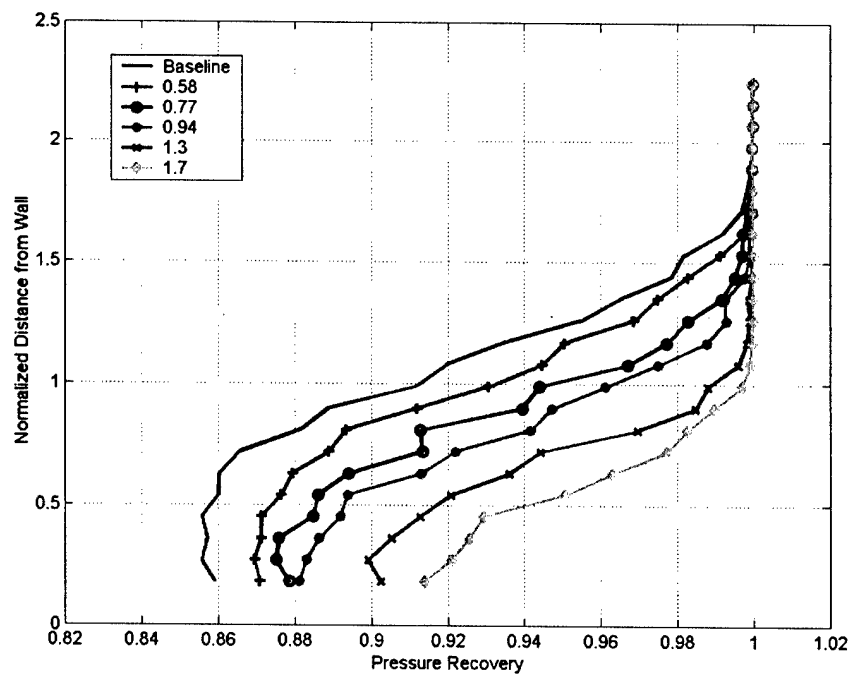
*Figure 4-8: Total Pressure Profile with Steady Injection*

Figure 4-9 and Figure 4-10 show the effect of injection mass flow on total pressure profile at constant actuation frequency. The results are plotted for 900 Hz actuation, since 900 Hz corresponds to  $F^+ = 1.03$ . Previous experiments [4] found  $F^+ \sim 1$  to be the optimal actuation frequency. The height of the separation bubble decreased as injection flow increased. The severity of the total pressure loss also decreased as injection mass flow increased. This agrees with the implication from the static pressure tap data; namely that increased injection mass flow with periodic excitation would improve pressure recovery. In Figure 4-10, distance from the wall is normalized by the bump height, 1.39 inches, using Equation 4-4.

$$h_{normalized} = \frac{y}{h_{bump}} \quad (4-4)$$



*Figure 4-9: Total Pressure Profile vs Injection Mass Flow (900 Hz actuation)*



*Figure 4-10: Pressure Recovery Profile vs Normalized Distance form Wall ( $F_+ = 1.03$ )*

Figure 4-11 and Figure 4-12 show the effect of actuation frequency on local pressure recovery for a fixed injection mass flow. The data was collected in different tests and was normalized by upstream total pressure to remove the effect of different atmospheric conditions. The local pressure recovery profile improves with increasing actuation frequency, until about 1 kHz. At actuation frequencies of 1 kHz and above, the local pressure recovery profiles show little variation in shape.

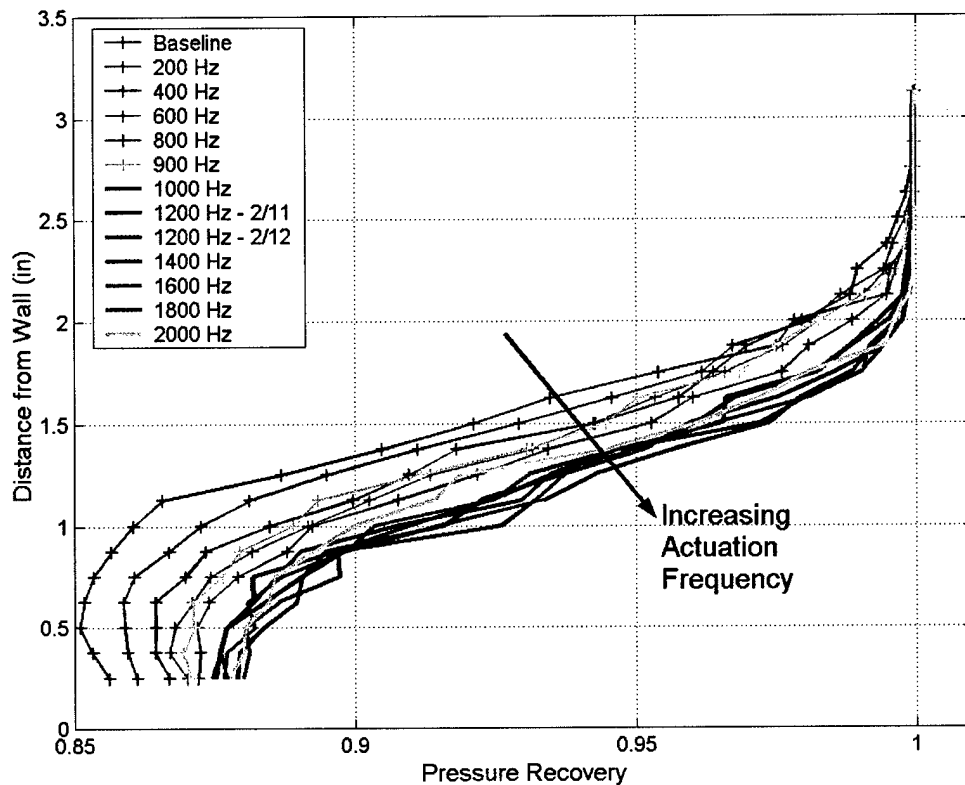


Figure 4-11: Pressure Recovery vs Actuation Frequency (0.018 lb/sec injection,  $C_\mu \sim 0.05\%$ )

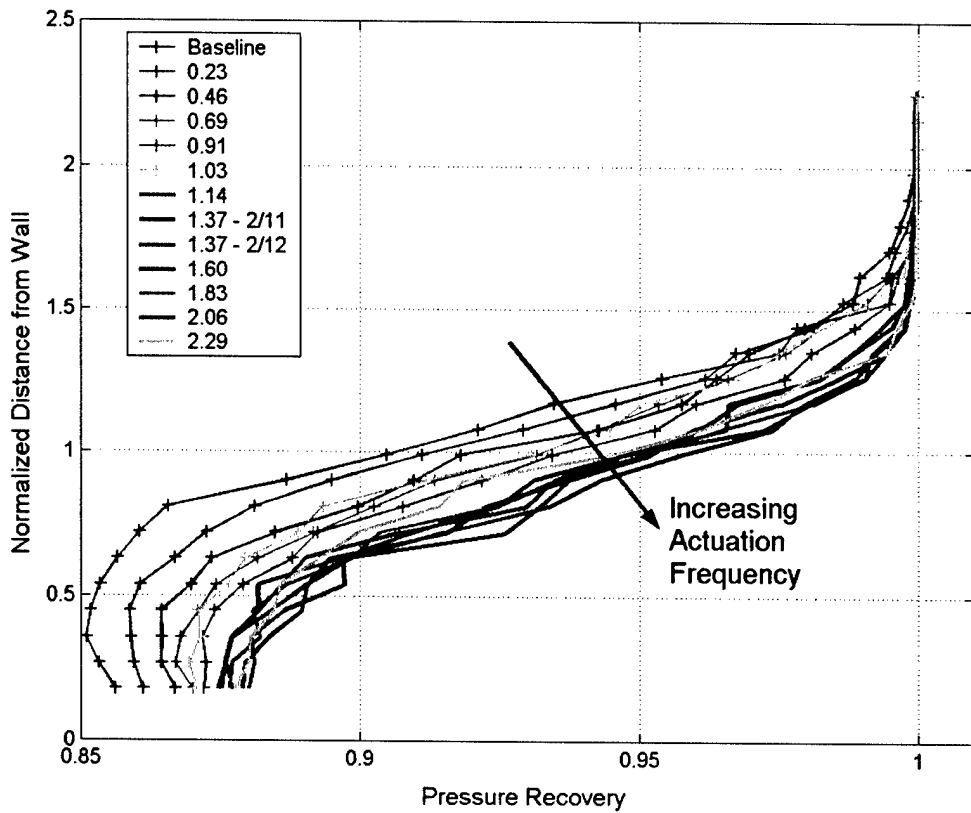


Figure 4-12: Pressure Recovery vs  $F^+$  (0.60% Core Flow,  $C_\mu \sim 0.05\%$ )

Pressure recovery results for various combinations of injector mass flow and actuation frequency are plotted in Figure 4-13 and Figure 4-14. The average pressure recovery is the measured total pressure at each location divided by the upstream total pressure, averaged across all locations of the traverse using Equation 4-5, where n is the number of locations.

$$\text{Pressure Recovery} = \frac{1}{n} \sum \frac{P_{T_i}}{P_{atm}} \quad (4-5)$$

The slight kinks in the graph at 1200 Hz are due to testing on different days at different atmospheric conditions. The data collection up to 1200 Hz was completed at a measured Mach of 0.75 past the top of the bump. The data above 1200 Hz was collected at a measured Mach of 0.77 past the top of the bump. Both of these Mach numbers were measured without injection. Once injection commenced, the measured Mach number dropped to 0.67 and 0.69 respectively. In order to eliminate the effect of the different

Mach numbers, the data for frequencies above 1200 Hz were adjusted to eliminate the difference in dynamic head. The total pressure loss measured inside the separation bubble was multiplied by the ratio of dynamic head between the two run conditions. This approach assumes the pressure recovery due to actuation scales with dynamic head. This is a reasonable assumption since the losses due to the separation scale with the dynamic head at the separation point.

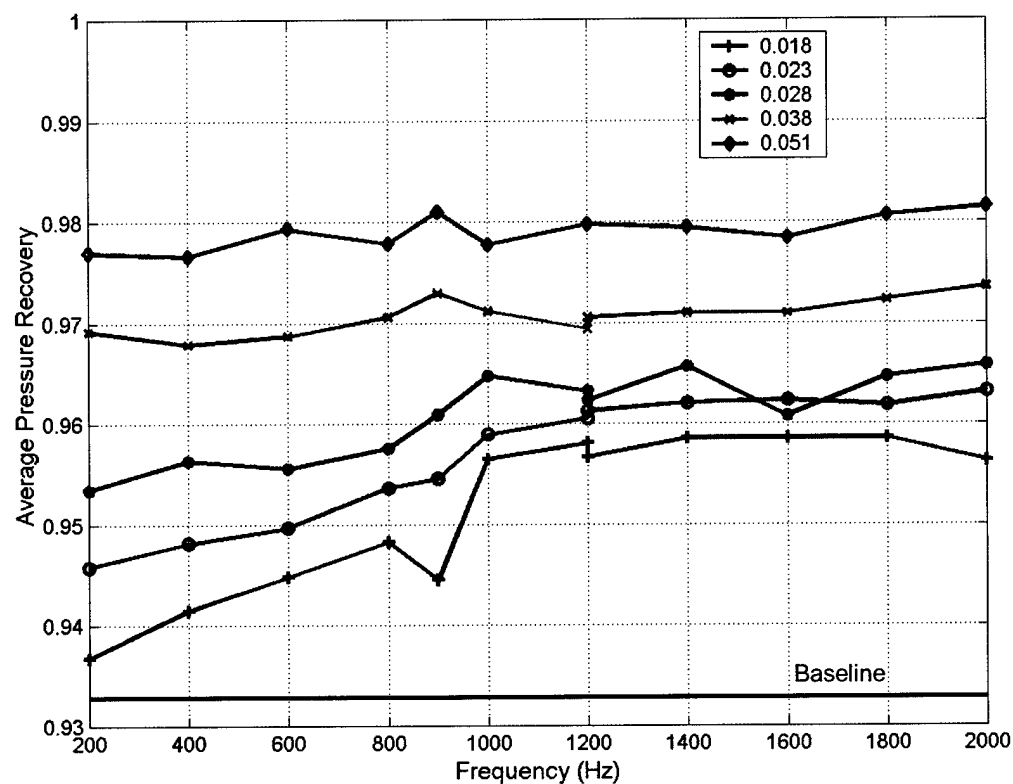


Figure 4-13: Pressure Recovery vs Actuation Frequency and Injection Mass Flow ( $C_\mu=0.05\%$ )

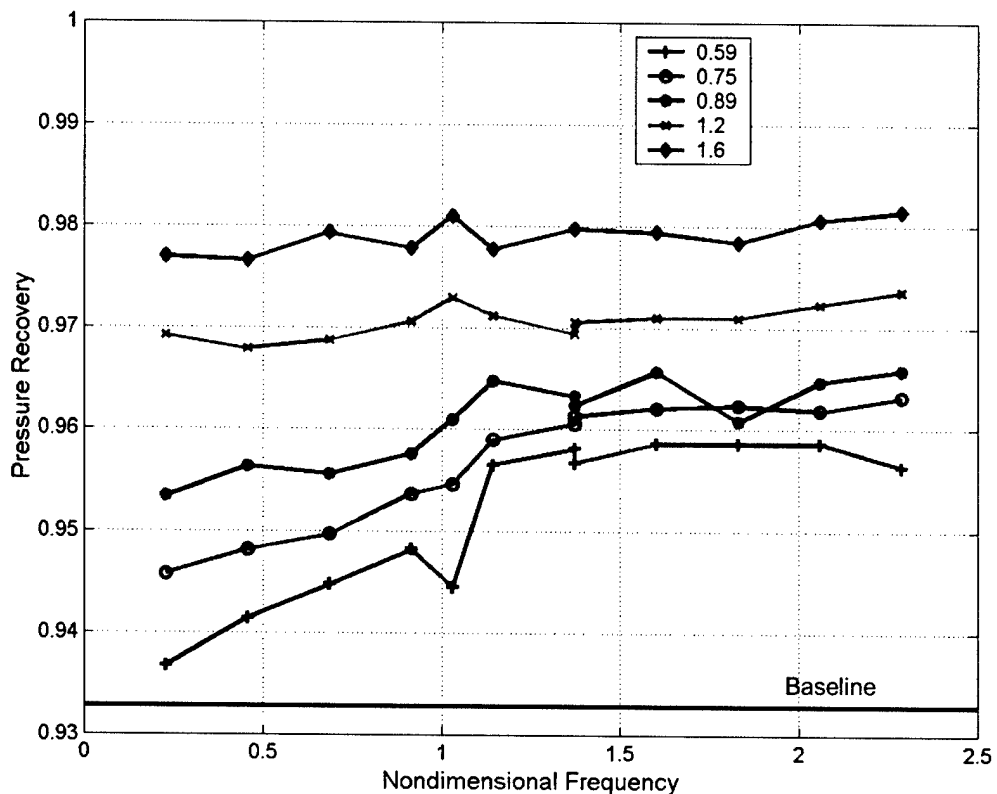


Figure 4-14: Pressure Recovery vs  $F+$  and Percent Core Flow ( $C_\mu=0.05\%$ )

Figure 4-13 clearly illustrates that high frequency actuation is much better than low frequency actuation at low injection mass flow. It also shows that as injection mass flow increases, the sensitivity of pressure recovery to actuation frequency decreases. Higher injection mass flows continue to improve the pressure recovery, but the largest pressure recovery per unit injected mass flow occurs above 1 kHz and at the minimum measurable mass flow, 0.018 lb/sec (0.60% core flow). The lowest measurable mass flow is set by the flow meter described in Section 3.2. The flow meter will not read below 8% volume flow, which corresponds to 0.018 lb/sec in all injection cases.

## 4.8 Flow Visualization

To verify the effect of actuation on the shape of the separation bubble, a flow visualization plate was built (Figure 4-15). This plate had a knife-edge leading edge to cleanly split the flow around the plate without disturbing it. It extended forward of the injector block and

fit closely to the surface of the flow separator bump. It was mounted to a wall section that mounted in place of the five inches of Plexiglas spacers in the test section. In order to prevent flutter at the high test section speed, the attachment to the Plexiglas section was made via L-brackets and bolts on both sides of the plate.

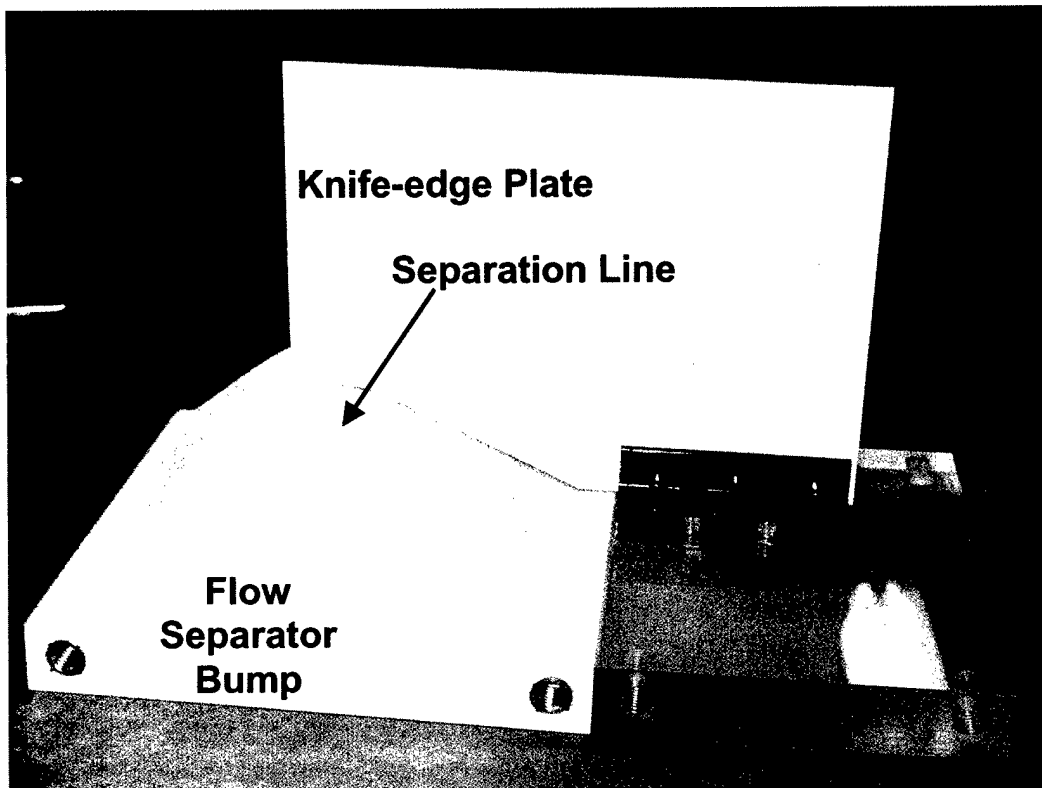


Figure 4-15: Flow Visualization Plate

The flow visualization plate was painted with a mixture of black Pigment Pur Dry Pigment (manufactured by Senneller) and silicone oil. As the flow passed the plate, the oil flowed along the air streamlines. The particles flowed with the oil, leaving steady flow lines on the plate.

The plate was painted and run at Mach 0.7 past the top of the bump with no injection as the De Laval came up to speed. As the De Laval warmed up, the oil and particles outside the separation bubble scrubbed clean, leaving the outline of the separation bubble. When the De Laval came up to speed, the actuation was turned on at 2 kHz ( $F^+ = 2.29$ ) and 0.070 lb/sec (2.50% core flow) injection. This actuation remained on for a few minutes while the

new flow paths formed inside the formerly separated region. The resulting pattern on the flow visualization plate is shown in Figure 4-16.

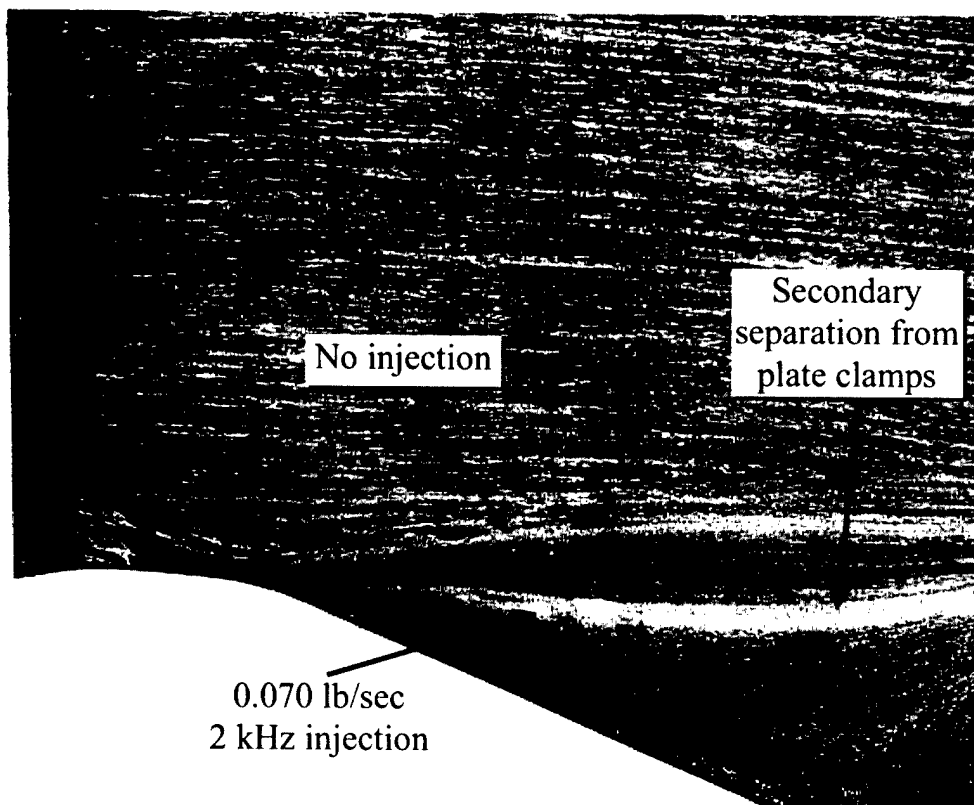


Figure 4-16: Flow Visualization Plate Results

The separation line showed up clearly on the flow visualization plate. The separation line changed with actuation, moving down toward the bump. Unfortunately, the L-brackets and bolts securing the plate to the Plexiglas holder caused a secondary separation at the end of the bump that prevented the flow from fully developing on the backside of the bump.

In later testing, glycol smoke was injected into the test section. In some tests, smoke was injected into the separation bubble via the traverse slot in the wall of the test section. In this test, the smoke filling the separation bubble completely dissipated when injection at 2 kHz and 0.070 lb/sec commenced, indicating the separation bubble had either reattached before the traverse slot (located 4.64 inches downstream of the injector exit) or been eliminated entirely.

To verify the flow structure, smoke was then fed along the wall of the test section by producing smoke on the edge of the bellmouth. The smoke followed the wall and clearly demonstrated the streamline curvature ahead of the flow separator bump. It followed the surface of the bump and then dissipated into the separation bubble, filling it with particles. When actuation at 2 kHz and 0.070 lb/sec commenced, the smoke in the separation bubble blew downstream. The smoke turned the corner down the back face of the bump and expanded down the back face of the bump. This implies the separation bubble was still present but greatly reduced in size. The smoke rounded the corner where the backside of the flow separator bump meets the test section wall, indicating the streamlines do curve, possibly producing the maximum  $C_p$  values discussed in Section 4.7.2.

While injecting the glycol smoke into the separated region, liquid glycol accumulated on the top wall of the test section inside the separated region. The glycol flowed along the wall streamlines, similar to the flow of silicone oil on the flow visualization plate. When testing without injection, a line of glycol formed approximately 10 inches downstream of the separation line. The line of glycol represented the reattachment line of the separated region. Upstream of the glycol line, the flow was reversed in the separated region. Downstream of the line, the flow continued axially through the test section. When actuation commenced, the line of glycol moved upstream, indicating a shortened separated region. As injection mass flow increased, the line of glycol continued to move upstream. Once the line of glycol reached the traverse slot, smoke could no longer be injected into the separated region. At that point, the separated length was reduced to approximately 4.5 inches, the distance of the traverse slot from the separation line.

No quantitative measurement of the reattachment line was recorded. In general, all actuation frequencies (from 100 Hz up to 2 kHz) caused the reattachment line to move to the traverse slot. Injection at 2 kHz required the least mass flow (0.036 lbs/sec, 1.20% core flow). When  $F^+$  was rescaled to reflect reattachment at 4.5 inches, 2 kHz corresponded to  $F^+ = 1.03$ . Decreasing actuation frequency increased the amount of injection mass flow necessary to move the reattachment line to the traverse slot.



---

## **5 Tactical Aircraft Inlet Test**

---

### **5.1 Objective**

The tactical aircraft inlet test was designed to show the effect of unsteady separation point injection in a scaled serpentine aircraft inlet under cruise conditions.

### **5.2 Setup**

This section describes the various duct elements that make up the tactical aircraft inlet test setup, shown in Figure 5-1. A mass flow throttle plug was mounted to a plate on the De Laval compressor piping (the large flange in the rear portion of the photo). A section containing steady total pressure rakes for measurement of total pressure at the aerodynamic interface plane, the steady total pressure can, was then mounted to the front of the throttle plug. The diffuser was then bolted to the front of the static pressure can. The bellmouth was attached to the front of the diffuser. The rotary valve was secured in a recess cut into the diffuser. The injector block sat securely in position in the diffuser, held in place by the rotary valve (as described in Section 3.2).

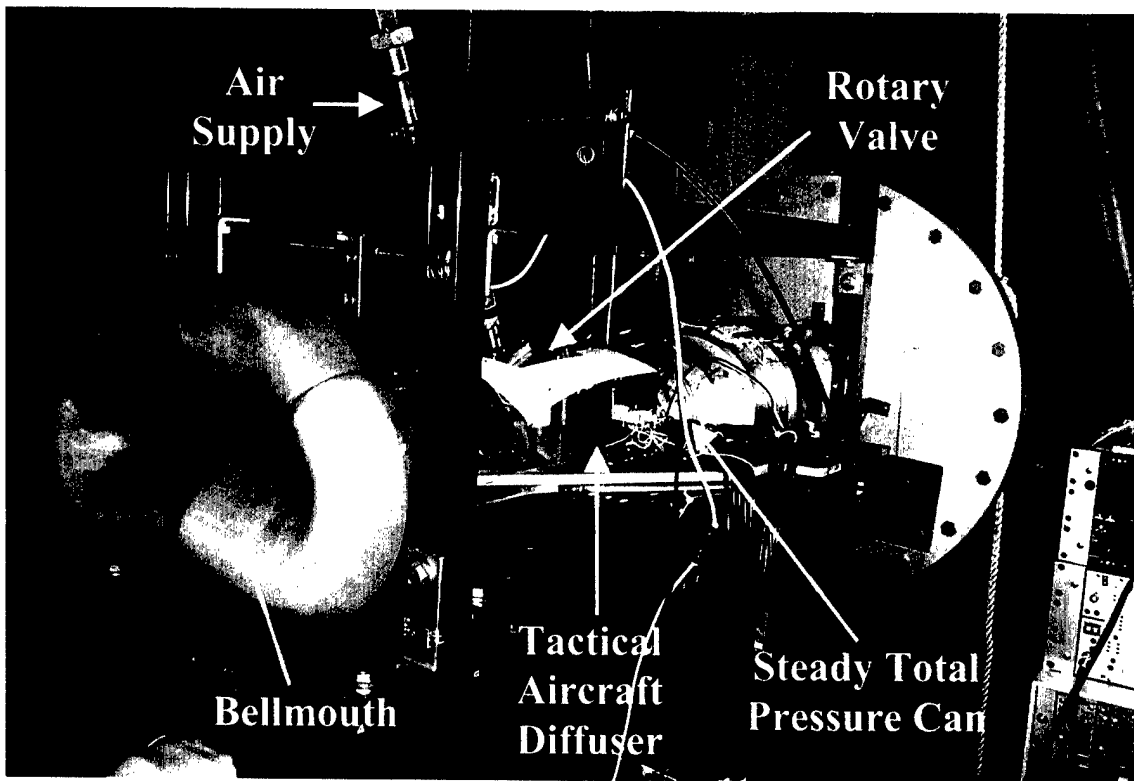


Figure 5-1: Tactical Aircraft Inlet Test Setup

The mass flow throttle plug is a device that meters mass flow through the inlet by choking the flow. Inside the throttle plug, the outer flow wall expands conically. There is a bullet in the center that sets the size of the choking area by its axial position in the plug. A stepper motor built into the throttle plug controls the position of the bullet. It can be set anywhere from fully closed at the front of the travel to fully open at the rear of the travel. If the throttle plug is set fully open, the minimum cross section in the system is no longer in the throttle plug. The bullet no longer sets the choking area, and therefore the mass flow through the inlet would be unknown. To prevent this from occurring, the throttle plug is operated at low enough mass flows to ensure the choking orifice is inside the throttle plug. To ensure that the system was indeed choking, the pressure ratio across the entire inlet was maintained at a minimum of 2.0. This pressure ratio was determined by dividing the measured atmospheric pressure by the pressure measured from a tap in the plate joining the mass flow plug to the De Laval piping.

The stepper motor is controlled by a 12 – 20 V DC drive power supply. The connection to the power supply includes a three-way switch that controls the wiring of the drive circuit.

It allows the sense of the signal to be switched in order to reverse the traverse direction. The third position of the switch disconnects the power supply to prevent accidental changes to the bullet position and the related mass flow setting. Another push button switch is used to close the circuit. This way one circuit controls the direction of the traverse and a second, higher precision switch controls the actual motion of the traverse.

A voltage divider circuit determines the location of the bullet. A 12 V signal is applied across a potentiometer in the throttle plug. The potentiometer outputs a signal between 0.59 V and 12 V that corresponds to the bullet position in the mass flow plug. Warfield found the calibration between measured voltage and bullet position to be Equation 5-1 [6].

$$x = 0.50517 * V - 0.27751 \quad (5-1)$$

The investigator verified this calibration before using the mass flow plug. Equation 5-2 relates the position of the bullet to the mass flow.

$$\dot{m}_{calculated} = -0.0068 * x^4 + 0.049 * x^3 - 0.201 * x^2 + 1.355 * x - 0.016 \quad (5-2)$$

This equation is for specific atmospheric conditions: 14.7 psia ambient pressure ( $P^*$ ) and 73 °F ambient temperature ( $T^*$ ). The calculated mass flow can be related to actual mass flow by Equation 5-3, where  $P_{atm}$  and  $T_{abs}$  are the ambient conditions at the time of the test.

$$\dot{m}_{core} = \dot{m}_{calculated} \frac{P_{atm}}{P^*} \sqrt{\frac{T^* + 460}{T_a + 460}} \quad (5-3)$$

The investigator wrote two Matlab scripts to calculate the actual mass flow through the inlet. The first, `massflow_curve.m` (see Appendix A), takes the ambient conditions as inputs then calculates the mass flow curve for all bullet positions and plots the results. Using this plot, the investigator would determine the voltages the plug should be reading at the correct mass flow. After the design voltage was arrived at, the investigator would run the other script, `calcmass.m` (see Appendix A), which would prompt the user for input the atmospheric conditions and plug voltage, and from these compute the exact mass flow, ensuring the test was conducted at the desired mass flow.

The injection air supply was the same one described in Section 3.2. The supply hose was supported by a rope looped through an eyehook in the ceiling to relieve most of the load from the weight of the hose and rotary valve. Additional mounting of the rotary valve is described in Section 5.5

### **5.3 Instrumentation**

The only data collection instrument in the tactical aircraft inlet test was a steady total pressure can (Figure 5-2). The steady total pressure can has eight rows of five total pressure taps arranged at  $45^\circ$  intervals around the can. The probes represent the AIP and are used to measure the total pressure recovery and distortion at the AIP. The probes are spaced such that the measurement from each probe estimates the pressure over one-fortieth of the AIP area. The radial spacing of the probes places each probe at the centroid of the AIP area it represents. This places the probes at 31.4%, 54.8%, 70.6%, 83.6% and 95% of the outer radius. The individual probe locations are plotted in Figure 5-3.



Figure 5-2: Steady Total Pressure Can

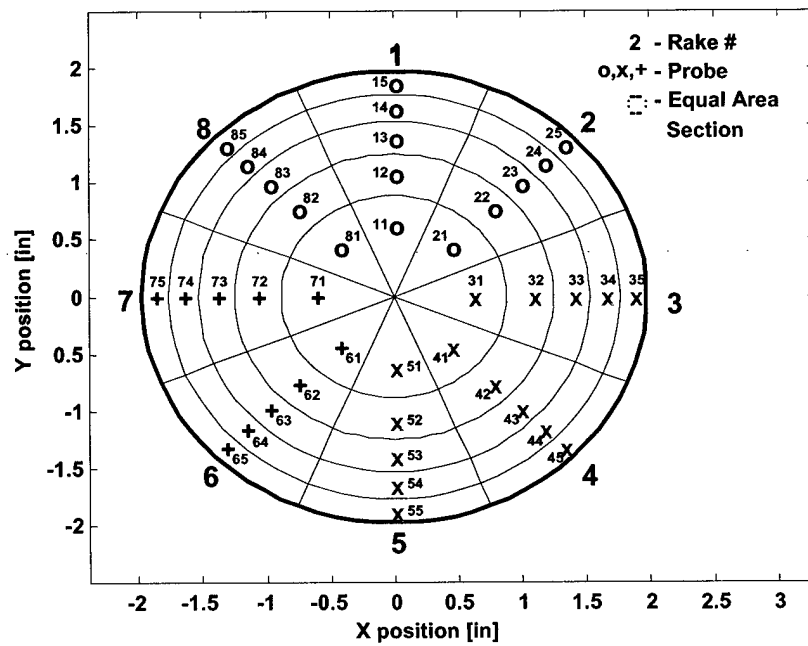


Figure 5-3: Probe Locations in Steady Total Pressure Can

The total pressure probes are connected to metal tubing on the outside of the can. These metal tubes are connected via flexible tubing to pressure transducers to record the total pressure at the AIP. The tubing distance between the probes and the transducer leads to a non-negligible settling time when run conditions change the total pressure profile at the AIP. To prevent taking data during transients, the signals were allowed to settle for several seconds after modification of test conditions before data was collected.

## **5.4 Data Acquisition**

A laptop computer acquired the data for the tactical aircraft inlet via an ethernet connection to a 16-port autonomous Scanivalve.

### *5.4.1 Hardware*

Measurements were taken using a 16-port autonomous Scanivalve (Model DSA 3217/16Px by Scanivalve Corp). This Scanivalve has a 100 psig transducer and measures pressure to 0.0055 psi precision. In order to accommodate measuring more than 16 total pressure ports, the tubes from the total pressure can were connected into two quick-change connector plates to facilitate changing the monitored ports rapidly during testing. Ports 11-25 and 81-85 were connected to one plate (denoted as red “o” ports in Figure 5-3). Ports 31-55 were connected to the other plate (denoted as green “x” ports in Figure 5-3). Data was not collected for ports 61-75 (denoted as blue “+” ports in Figure 5-3). Instead, the flow was assumed to be symmetric about the centerline and data from ports 31-45 were reflected across the centerline to ports 61-75 for plotting purposes.

The Scanivalve calibration was verified before it was used in testing. It was first calibrated against a 600 – 1100 millibar Setra to verify the linearity and scale factor of the readings. The transducers were found to be linear with pressure and report differential pressure accuracy to the 0.0055 psi precision limit set by the internal data acquisition system. Each transducer was found to have its own offset. This offset remained constant during a continuous testing period but varied between testing days. To remove the effect of this offset, data was taken with all ports vented to the room to determine the offset for the scans conducted during testing that day.

### **5.4.2 Software**

The Scanivalve is completely autonomous. On startup, it calibrates the transducers, sets their gains and loads the last scan parameters.

The Scanivalve is controlled by a telnet connection over an ethernet cable. The computer would log into the Scanivalve at IP address 191.30.80.41. In order to record the data, the telnet window was set to start logging to a data file before each scan. The logging was stopped after each scan to close out the data file. For the next data file, logging was started again, this time using another file name.

The first command to the Scanivalve was “status”, to which the response in the telnet window would be “STATUS: READY”. The next command was “list s”, which caused the Scanivalve to report back all the parameters it is set to scan at. These properties include: sample period, number of samples to average, number of scans to complete, units of measurement and scale factor for measurements. The period was set to 1000 ms, which yielded a 1 kHz sample rate. The Scanivalve averaged 100 samples per port to determine the pressure reading during a scan. It was set to complete 10 scans (FPS) each time the scan sequence was triggered. The pressure was measured in psi (UNITSCAN) and recorded with a scale factor (CVTUNIT) of 1.000000. The scan commenced when the investigator entered the “scan” command into the telnet window. Before the telnet window was closed, “list s” was run again to record the scan parameters for the run.

## **5.5 Actuation System**

The rotary valve provided the actuation for the tactical aircraft inlet tests. In order to prevent damage to the inlet from loads associated with the rotary valve, the valve was attached to a superstructure above the inlet test section (Figure 5-1). The tube clamps and threaded rods from the bench test setup were used to clamp the air supply to the superstructure above the inlet. When tightened, these clamps prevented the rotary valve from moving relative to the inlet section. Loads applied to the rotary valve were transferred to the inlet support structure and caused the whole setup to move while preventing relative motion of the rotary valve and its mount on the inlet.

The air supply hose was suspended from the eyehook in the ceiling as in the 2D test section tests. Additionally, the hose was tie wrapped to the superstructure above the inlet to prevent motion of the hose that would apply loads to the rotary valve.

## 5.6 Calibration

The Scanivalve sets the gain of the transducers as part of its startup sequence. Data was taken before the start of each run to determine the offset in measured pressure values as described in Section 5.4.1. This offset was removed from the data sets as part of the reduction process.

## 5.7 Results

Before the data could be reduced, it needed to be reorganized into a matrix format. To accomplish this, the log files were imported into Excel. Both data sets for each set of run conditions were combined on one Excel spreadsheet. The value for each data point was rearranged by probe number and scan number. The offsets were subtracted and the resulting pressure measurements were converted into pressure recovery. The data was reordered to place all the probes in their correct order and to mirror the data from probes 31-54 onto probes 61-75. The resulting local pressure recovery matrix was copied into a text file, resulting in a “results” file with data in ten columns, one for each scan, and forty rows, one for each probe in ascending order.

To visualize the effect of injection on the total pressure profile at the AIP, make\_map.m (see Appendix A), written by Warfield [6], was modified to plot the data from the results file. make\_map.m queries the user for inlet core flow, injection mass flow and which scan number to plot. It can also plot the average of all scans, resulting in a plot of the average of 1000 data samples at each point. The script plots each pressure recovery at its respective location and then interpolates the values between data points. The results for 3.1 lb/sec core flow without actuation are shown in Figure 5-4. The area of low pressure recovery in the center top of the plot was due to the effects of the separation. Figure 5-5 is a plot of the same flow conditions with 0.106 lb/sec injection mass flow at 2 kHz actuation. This injection corresponds to a  $C_\mu$  value of approximately 0.06%. The pressure

recovery in the region affected by the separation improved significantly. The lowest local pressure recovery increased from 85% to 89%. This indicated the injection was decreasing the pressure loss at the AIP due to the separation bubble.

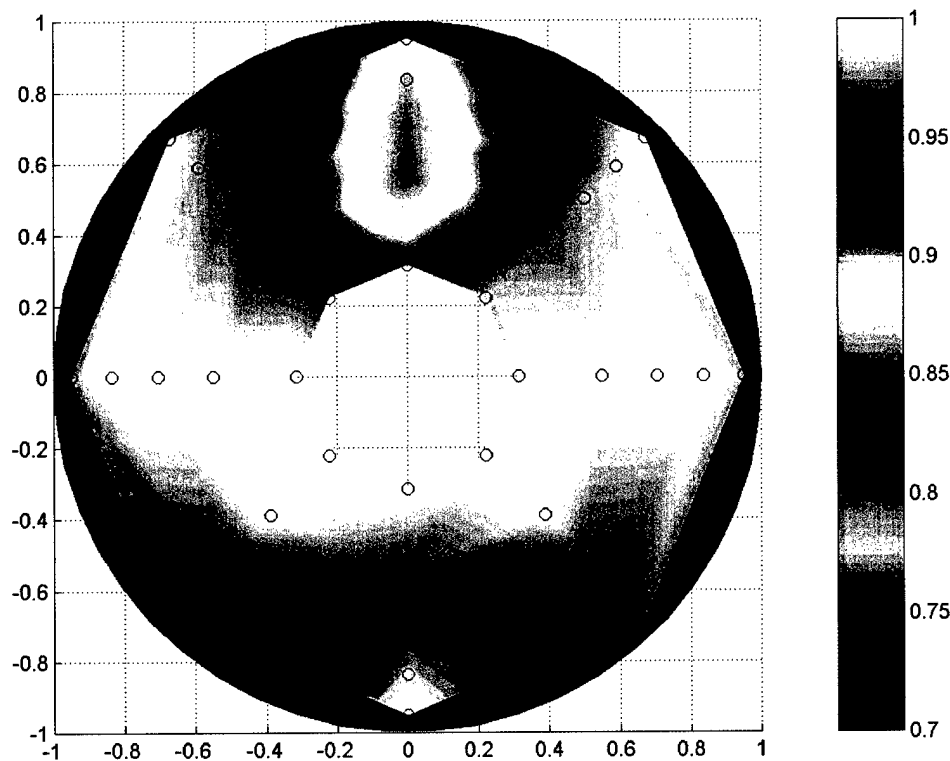
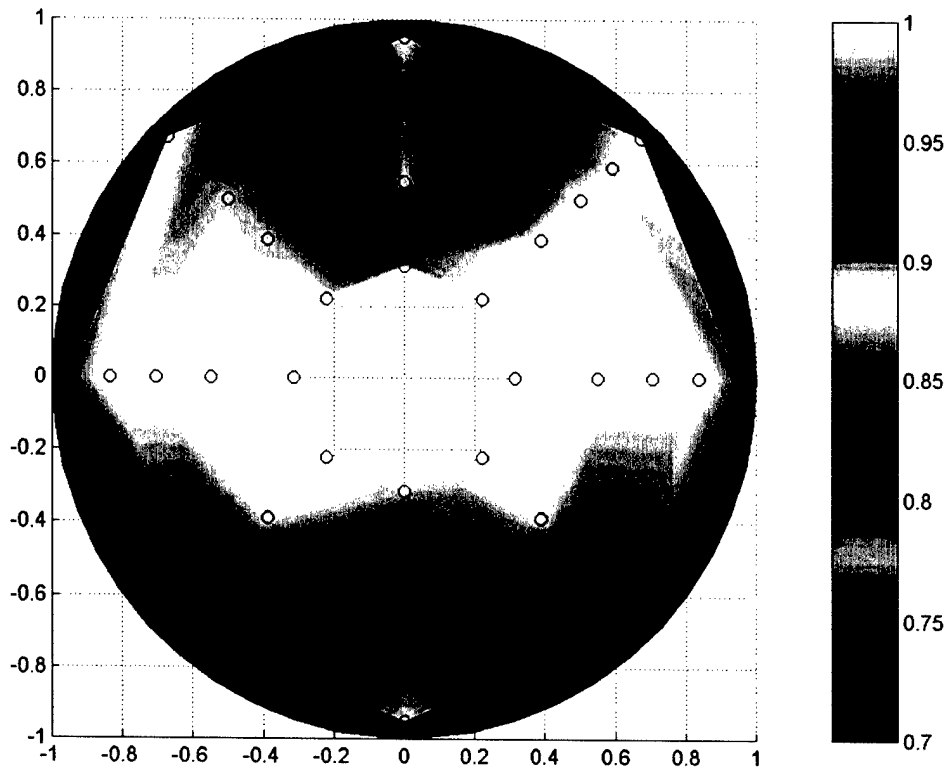


Figure 5-4: AIP Total Pressure Profile at 3.1 lb/sec without Injection



*Figure 5-5: AIP Total Pressure Profile at 3.1 lb/sec with 0.106 lb/sec Injection at 2 kHz ( $C_\mu \sim 0.06\%$ )*

In order to compare the effect of different levels of actuation on the AIP, make\_plot.m (see Appendix A) was developed. It reads in all the results files and averages the local pressure recovery for each injection and flow condition. It then plots the cumulative results in a single plot. Figure 5-6 plots the pressure recovery as a function of both core mass flow and injection mass flow as a percent of core mass flow. Figure 5-7 plots the pressure recovery as a function of core mass flow and steady  $C_\mu$  of the injection flow.

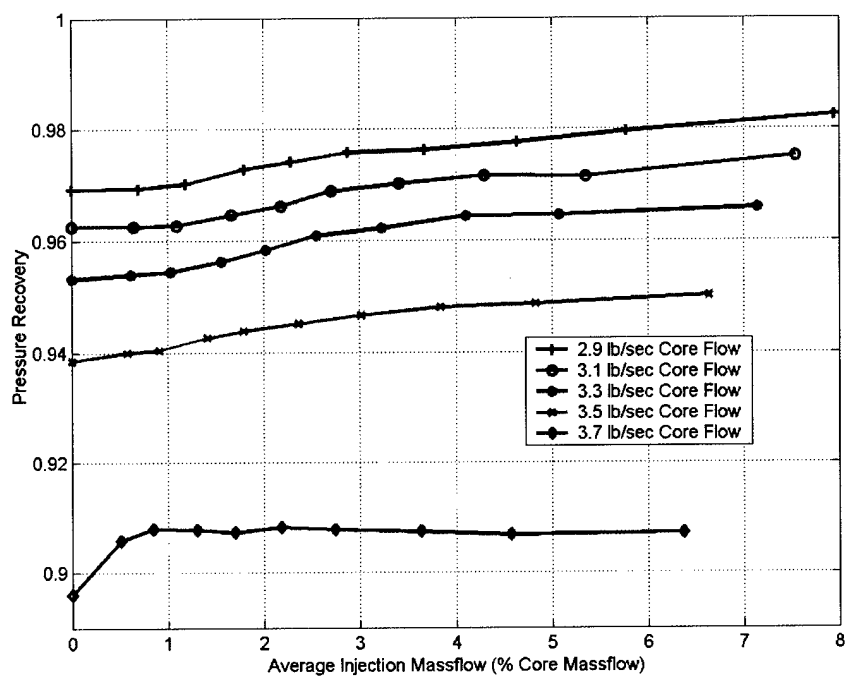


Figure 5-6: AIP Pressure Recovery vs Core Mass Flow and Percent Injection Flow

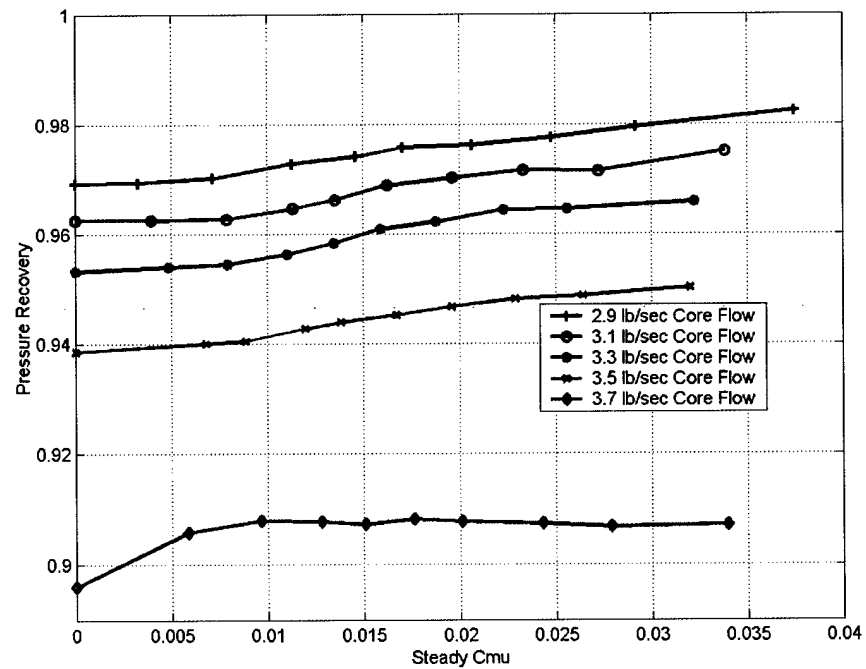


Figure 5-7: AIP Pressure Recovery vs Core Mass Flow and Injection Steady  $C_\mu$

Looking at the pressure recovery for the whole AIP understates the pressure recovery improvement due to injection. There are other factors that contribute to less than ideal pressure recovery at the AIP, most notably a region of low pressure recovery on the bottom of the AIP. The injection was not designed to improve the pressure recovery in this region. In order to better assess the injection performance, the pressure recovery of the upper quadrant of the AIP was analyzed separately. Figure 5-8 plots the pressure recovery on this limited area as a function of core mass flow and percent injection flow. Figure 5-9 plots the pressure recovery on this limited section as a function of injection steady  $C_\mu$  and core mass flow.

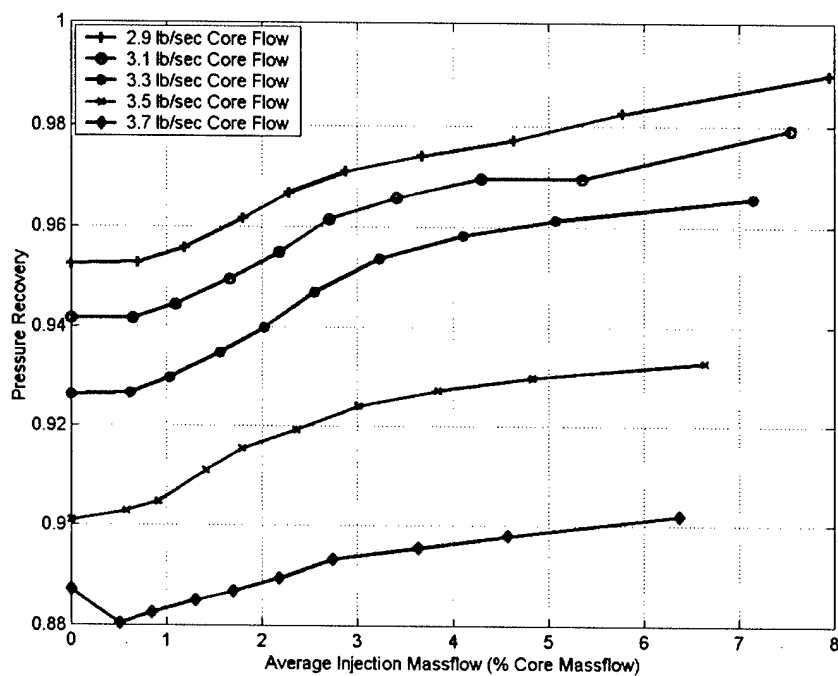
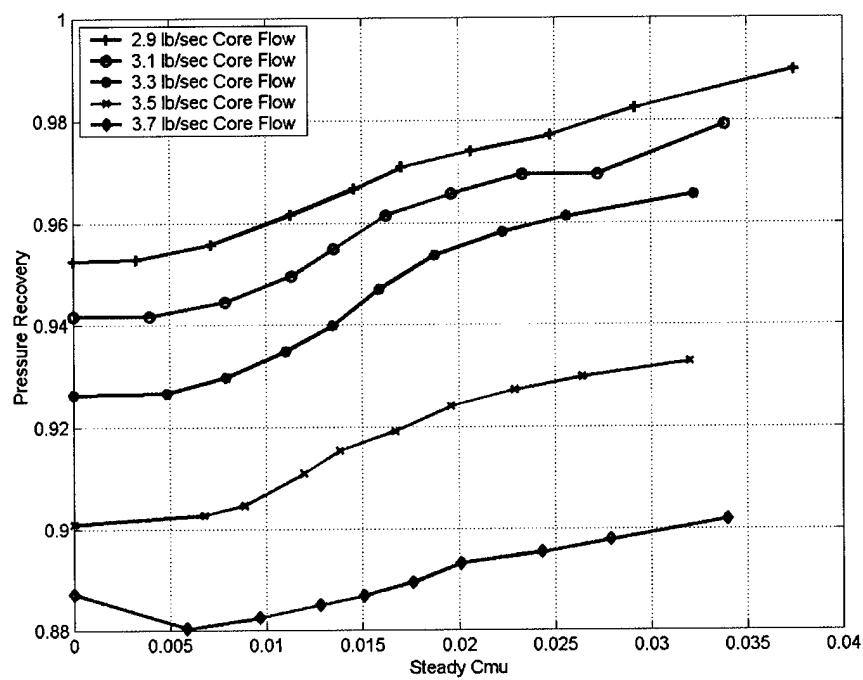


Figure 5-8: Upper Quadrant AIP Pressure Recovery vs Core Mass Flow and Percent Injection Flow



*Figure 5-9: Upper Quadrant AIP Pressure Recovery vs Core Mass Flow and Injection Steady  $C_\mu$*



---

## **6 Discussion**

---

The following sections provide discussion of the results from the bench, 2D test section and tactical aircraft tests.

### **6.1 Bench Test**

The bench test dealt with the characterization of the actuator and injector combination. The issues of flow uniformity and generation of unsteady signals were addressed.

The steady bench test quantified the uniformity of the flow out of the injector. The total pressure across the injection sheet was sufficient for further testing. The flow out the injector produced maximum total pressures within 22% of the mean total pressure across 90% of the span of the injection sheet (Figure 3-7). An average 16% higher total pressure was measured in the span from -20 mm to the centerline and 43% lower total pressure was measured on the edge of the sheet between -50 mm and -45 mm. This test also verified that the injection sheet was turning to follow the wall downstream of the injector, adhering to the Coanda effect as designed. The total pressure profiles (Figure 3-6 and Figure 3-7) indicate the flow turned at least 10° of the 24° turn downstream of the injector. The measurement of flow turning angle was limited to a maximum of 10° due to the size of the probe head.

The first unsteady bench test, conducted 0.64 inches downstream of the injector, tested the suitability of the actuator and injector combination to produce the signal necessary to complete 2D test section and inlet testing. The signal amplitude could be clearly distinguished at actuation frequencies up to 2 kHz. The average output signal degraded in amplitude by approximately 60 percent from steady state up to 900 Hz. Above 900 Hz, the amplitude of the span-wise averaged output signal remained constant with increasing frequency. Also, the amplitude of the output signal at any given frequency decayed at the edges of the injection sheet (Figure 3-8). This was expected to some extent as the edges had demonstrated lower total pressure in steady tests. However, the span-wise decay in

frequency response began closer to the center of the slot than in the steady response, 25 mm from the centerline compared to 40 mm from the centerline respectively. Two possibilities for this difference were considered. The flow out of the slot could be different under unsteady actuation, causing the signal to attenuate at the outside edges of the duct. The flow could also be mixing with the surrounding air more at the edges of the sheet than in the center of the injected flow.

To test the duct, total pressure was measured at the injector exit to determine uniformity of the ejected flow (Figure 3-8). The total pressure variations up to 20 mm from the center were 136 % to 155 % higher than the average pressure amplitudes across the slot. The total pressure amplitudes at the edge of the slot (50 mm) proved to be significantly different. These measurements were at most 53 % of the average at a specific actuation frequency and in general only 21 % of the average pressure amplitude. This can be attributed to the effect of the sidewall as the probe was resting against the sidewall when measurements were taken at the edge of the slot. The consistency of the signal across the injector exit implies that the injector was emitting a uniform signal and that the high frequency signal attenuation near the edges of the sheet was due to mixing with external flow after exiting the duct.

Data from the injector exit test was also used to determine  $C_\mu$  at various operating frequencies and pressure ratios. The calculated values of  $C_\mu$  up to 0.063 % were lower than the 0.2% necessary to establish suitable pressure recovery in experiments at UTRC [4]. Unfortunately, the values of  $C_\mu$  produced on the bench varied between 0.041% and 0.063 % with pressure ratio (Figure 3-14). Increasing the mean flow through the injector increased the steady  $C_\mu$  of the injection flow (Figure 3-16), raising the average momentum of the injected flow. The momentum per unit flow was equal in the injection and core flows at an injection pressure ratio of approximately 2.7.

In order to achieve the desired values of  $C_\mu$  while keeping injection velocity high and mass flow low, the injector block was redesigned so that the exit slot is much thinner than the original injector exit slot. This also reduces the effective plenum size between the rotary valve and the convergent injection duct, so that mass storage effects are minimized.

Therefore this new injector design should exhibit less attenuation of the pressure perturbations generated by the rotary valve at low injection mass flows.

## 6.2 2D Test Section Tests

The 2D test section tests dealt with injector performance at cruise conditions. It quantified the uniformity of steady injection at high subsonic core flow conditions. Tests indicated how injection parameters altered pressure recovery in the separated region. It also gave insight into the nature of the effect the injection had on the separation. The 2D test section tests helped determine the injection parameters tested in the tactical aircraft inlet.

The 2D test section was first used to measure the uniformity of the injection sheet in the presence of the core flow. The injection sheet was found to have the same qualitative characteristics as seen on the bench (Figure 4-3). The maximum total pressures in the span from -20 mm to the centerline were 3 % higher than the span-wise average. The maximum total pressures over the 10 mm at the edges of the duct were 15 % lower than the span-wise average, attributable to better mixing with the flow through the test section. The flow also turned between 17° and 18.7° of the 24° turn downstream of the injector exit, adhering to the Coanda effect.

Parametric studies determined the effect of injection mass flow and actuation frequency on pressure recovery. Unfortunately, the flow separator bump did not produce a clearly defined signal in the downstream unsteady total pressure measurement that could be used to indicate which frequency would be likely to work well for actuation. Both static pressure on the bump and total pressure traverses determined that actuation frequencies above 900 Hz ( $F^+ = 1.03$ ) were significantly better than actuation below 900 Hz. Coefficient of pressure variation with streamwise position, computed from static pressure measurements on the wall increased in slope with actuation frequencies above 900 Hz (Figure 4-6). Total pressure profiles improved with increasing actuation frequency, up to 1 kHz (Figure 4-11). Above 1 kHz, the total pressure profiles collapsed onto a single profile. This dependence on actuation frequency was observed at low injection mass flows. Varying the injected mass flow while holding actuation frequency constant revealed that

pressure recovery improved as injected mass flow increased. Tests combining the actuation frequency and injection mass flow variation indicated that as injection mass flow increased, the dependence of pressure recovery on actuation frequency decreased until the pressure recovery became insensitive to actuation frequency at 0.038 lb/sec injection mass flow (1.2 % core flow) (Figure 4-13).

The results of the 2D test section tests indicated that the best combination of actuation frequency and injection mass flow for the tactical aircraft inlet would be high frequency (above 900 Hz) and low injection mass flow (below 0.038 lb/sec). This combination should yield the highest pressure recovery per unit mass flow. The high frequency was chosen to be 2 kHz as it had the highest values of  $C_\mu$  of any frequency above 900 Hz (Figure 3-10). The injection mass flow was chosen to be 0.018 lb/sec, the minimum measurable mass flow through the injector. This mass flow had the most pressure recovery per unit mass flow in the 2D tests (Figure 4-13). Other frequency and mass flow combinations were also considered, but this point was established as the most promising injection condition and therefore the primary focus point for testing in the tactical aircraft inlet.

Flow visualization in the 2D test section indicated that injection decreases the size of the separation bubble rather than eliminating it. Tests involving increasing mass flow at a set actuation frequency showed changes in the reattachment line at the end of the separated region. Glycol smoke injected into the separated region would accumulate on the wall of the test section and converge on the reattachment line. The wall shear stress is negligible on this line as it is the border between reverse flow on the upstream side and normal flow on the downstream side. Since there is negligible shear stress at the wall, the glycol would form a line on the test section wall indicating the presence of the reattachment line. As injected mass flow increased, this line moved toward the separation line. Thus the separation was shrinking rather than being eliminated by the injection flow. This observation was also supported by tests involving smoke injected along the test section wall. In this configuration, the smoke would follow the wall and clearly diverge throughout the separated region with no injection. When injection commenced, the flow would follow the wall downstream of the separation point. Instead of staying a constant

thickness, the smoke layer would grow to approximately twice its thickness as it passed through the separated region, indicating the separated region still existed although in a much smaller manifestation.

One difference between testing in the 2D test section and the aircraft inlet was the characteristic frequency without injection. In the aircraft inlet, previous testing had found a characteristic frequency between 700 and 900 Hz in the total pressure measurements at the AIP [16]. In the 2D tests, no characteristic frequency was found in the total pressure measurements. A characteristic frequency could be found in some data sets, but none of the amplitudes was very strong compared to the measurement noise (most signals were less than 6 dB of power). Characteristic frequencies in data from neighboring locations in the same run were not the same, suggesting that there was no characteristic frequency in the 2D test section. In contrast, when similar analysis was performed on data sets with injection, the injection signal would show up as a signal roughly 40 dB higher than the measurement noise.

### 6.3 Tactical Aircraft Inlet Test

The tactical aircraft inlet test evaluated the injection performance in an actual inlet design at cruise conditions. First, pressure recovery across the entire AIP was considered. Injection at 2 kHz produced improved pressure recovery (Figure 5-6), but not as dramatically at low injection mass flows as in the 2D test section. Investigators performed an actuation frequency sweep at constant mass flow. The Scanivalve readout of the two lowest probes in the deficient area indicated that pressure recovery was best at 2 kHz actuation frequency and degraded significantly for actuation frequencies lower than 1 kHz. The sweep was abandoned at 500 Hz because the pressure recovery continued to decrease as actuation frequency dropped.

Once 2 kHz was established as the best actuation frequency, the injection mass flow was increased to improve pressure recovery. Pressure recovery continued to improve as injection mass flow increased, but pressure recovery never reached 100% (Figure 5-6). Part of the pressure recovery improvement was due to the energy of the injected air. Analysis of the energy of the injection flow revealed that at low injection mass flows, the

energy associated with pressure recovery improvement was greater than the energy added with the injection flow (up to ~1.3 percent core flow at 2.9 lb/sec, increasing to ~2 percent core flow at 3.3 lb/sec). Above this injection level, pressure recovery continued to improve with increasing injection mass flow, with diminishing return on the energy required to generate the injection. The pressure recovery could not reach 100% due to this actuation because part of the deficit was due to poor flow at the bottom and sides of the AIP. The injection location could not improve these areas, leading to a maximum pressure recovery less than 100%.

To inspect the deficit due to the separation only, the pressure recovery of the top three rakes was considered separately. This showed that the pressure deficit due to the separated region decreased as injection flow increased (Figure 5-8). The increase was fairly linear with injection mass flow increases and steady  $C_\mu$  increases (Figure 5-9).

It is important to note that at the lowest injection level, the pressure recovery in this region remained completely unchanged, except at the highest core mass flows. This was attributed to the low average momentum of the injection air. To remedy this problem, the redesigned injector (Appendix C) has a smaller exit area, ensuring the exit velocity will be higher for the same injection mass flow.

There is a disparity between the jump in pressure recovery in the 2D test section and the lack of enhancement in pressure recovery in the aircraft inlet at high frequency (2 kHz), low mass flow (0.018 lb/sec, 0.60 % core flow) injection. One possible explanation of this behavior is that the inlet has strong secondary flows. These flows cause a pressure recovery deficit at the same area of the AIP as the separation in low core flow conditions where the inlet does not separate. Thus the injection may be able to reattach the flow without improving pressure recovery at the AIP. In this case, the injection should both reattach the flow and counter the secondary flows in order to improve pressure recovery at the AIP.

Another important observation is the difference in behavior of the pressure recovery at 3.7 lb/sec core mass flow. In this case, the pressure recovery is insensitive to level of actuation, responding instead to the presence of actuation. This implies that the physical

mechanism governing the pressure loss had changed. One possibility is that a portion of the flow is supersonic at this flow condition. The resulting shock in the flow would cause the boundary layer to separate. Actuation near the separation line could cause the boundary layer to reattach, improving the pressure recovery at the AIP. The actuation level necessary to incite reattachment could be small, such that even the lowest injection level tested would cause reattachment. In that case, increasing the actuation authority would not necessarily improve pressure recovery. The boundary layer would already be reattached, regaining all the pressure recovery possible in that flow condition.



---

## **7 Conclusions**

---

This chapter presents the conclusions and recommendations for future work of this study.

### **7.1 Conclusions**

Periodic injection was applied at the separation point in a 2D test section and in a tactical aircraft inlet. Tests were conducted at a Mach number of 0.65. The actuation always consisted of adding mass to the freestream flow. A Coanda injector directed the momentum tangential to the wall. The downstream total pressure was measured and used to derive the pressure recovery. In both the 2D and tactical aircraft tests, periodic injection improved the pressure recovery.

In the 2D test section, injection improves the downstream total pressure profile. Flow visualization tests indicated that the recirculation zone shrinks as injection mass flow increases. The same degree of shortening was also achieved using lower injection mass flows with higher actuation frequencies. The highest actuation frequency tested, 2 kHz, was found to be the most efficient injection frequency, yielding the largest increase in pressure recovery per unit injection mass flow. Higher frequencies may increase efficiency, but the equipment was limited to maximum actuation frequency of 2 kHz.

Pressure recovery also improved as the injection mass flow increased.  $C_\mu$  remained constant with increasing injection mass flow, indicating that the steady component of the injection accounts for the enhanced control of separation. This result is contrary to previous findings that steady injection was detrimental to separation control [1,3]. This discrepancy was attributed to the difference between freestream and injected momentum. Most previous testing was conducted at relatively low freestream momentum with comparable or higher injection momentum. The relatively high freestream momentum in the tests conducted for this thesis, on the other hand, necessitated higher injection momentum to prevent the injection from inducing pressure loss at the AIP. The average momentum of the injected flow per unit mass should be comparable to the momentum of the core flow per unit mass, or the injected flow will cause a total pressure deficit.

Increasing injection mass flow increases the momentum of the injected flow, reducing the total pressure deficit created by injecting into the high momentum core flow.

Separation point injection can improve pressure recovery at the aerodynamic interface plane in the tactical aircraft diffuser. At all mass flows, increasing actuation frequency improved pressure recovery for fixed injection mass flow. The improvement was attributed to the separation zone shortening as observed in the 2D tests. Increasing mass flow at fixed actuation frequency also improved pressure recovery. Here the investigator conjectures that the improvement is due to the increased momentum of the injection flow reducing the total pressure deficit introduced by the flow that is injected into the core flow. The injection mass flow can reach a level where the momentum of the injected flow is greater than the freestream flow, creating a total pressure surplus. In this case, the pressure recovery will continue to improve with increasing mass flow, but some input injection energy will be lost to mixing with the lower momentum core flow.

The tactical aircraft inlet has three-dimensional flow that results in strong secondary flows. It is thought that these secondary flows generate total pressure losses that prevent complete reattachment of the separation. For this reason, the pressure recovery is not as strongly affected as in the 2D test section. In order to realize the full potential of separation point injection in modern serpentine inlets, the injection should also address the secondary flows induced by the serpentine turns.

The effectiveness, the extent to which the injection increases pressure recovery, and efficiency of the injection depend on both  $C_\mu$  and the mean velocity ratio, the ratio of the time mean injection velocity to the core flow velocity.  $C_\mu$  measures the control authority of the actuation. The mean velocity ratio, on the other hand, determines the total pressure deficit or surplus introduced by the difference between the mean injection and the core flow. For a given system, there exists a combination of  $C_\mu$  and mean velocity ratio that will produce the best pressure recovery for the least input energy. The investigator conjectures that a good value for mean velocity ratio is 1. This should result in the minimum  $C_\mu$  requirement. Based on the discussion above, values above 1 will tend to be inefficient.

## 7.2 Future Work

The results of the tactical aircraft inlet tests prove that separation point injection can increase pressure recovery at the aerodynamic interface plane. In order to maximize the pressure recovery improvement per unit injected mass flow, several additional approaches can be investigated.

- The redesigned injector (Appendix C) can be tested in the current experimental setup. The new injector has a variable slot width. Varying the slot width will change  $C_\mu$  by changing the injection exit area. This will allow investigation of the effect of  $C_\mu$  on separation control. It can also be used to verify the finding that increased injection velocity improves pressure recovery by reducing total pressure deficit between the injected and core flows. The redesigned injector can be resized to vary injection velocity while holding steady  $C_\mu$  and injection mass flow constant. The experiment will help to determine the effect of injection velocity on pressure recovery.
- Subsequent investigations should study the effect of mean velocity ratio on pressure recovery. They can determine the optimal mean velocity ratio to produce the most efficient injection, the largest increase in pressure recovery per unit input injection energy.
- For a given available mass flow, injectors can be designed to produce a desired  $C_\mu$  and mean velocity ratio at the design points. The mass flow and mean velocity ratio set the injection slot exit area. The volume of the effective plenum of the actuator and supply duct can then be tuned to insure the desired  $C_\mu$  is produced in the frequency bandwidth of interest. These injectors would show the limit of the technology's ability to improve pressure recovery with maximum injection efficiency.
- The secondary flow can be analyzed analytically and/or experimentally to determine the cause of the total pressure loss in fully attached flow. Computational fluid dynamics or experimental flow visualization can indicate the direction and

possibly the structure of the secondary flows. Separation point injection can then attempt to address both the separation and the secondary flow.

- Lessons learned from this study can be applied in other serpentine inlets. This will provide verification of the universality of the conclusions of this study.

## Appendix A: Data Reduction

### Injection Mass Flow Calculation

The injection mass flow was calculated using a flowmeter, a thermocouple and the regulated supply pressure. The Fischer and Porter Co. flowmeter consisted of an FP-2-27-G-10/83 tube and a 2-GSVTA-94 float, which produced a maximum 99 standard cubic feet per minute (SCFM) flow rate. The SCFM is defined at ambient conditions of 14.7 psia and 70° F. The conversion to cubic feet per minute (CFM) from SCFM is listed in Equation A-1, where  $P_{op}$  is the supply pressure (psia) and  $T_{op}$  is the supply temperature (°R).

$$CFM = (\% \text{ Flow})(99 \text{ SCFM}) \sqrt{\frac{P_{op} * 530^\circ R}{14.7 \text{ psia} * T_{op}}} \quad (A-1)$$

Equation A-2 gives the flow density through the flowmeter.

$$\rho = \frac{P_{op}}{RT_{op}} \quad (A-2)$$

The mass flow was then calculated using Equation A-3.

$$\dot{m} = \rho CFM = (\% \text{ Flow})(99 \text{ SCFM}) \sqrt{\frac{530^\circ R}{14.7 \text{ psia} * R}} \left( \frac{P_{op}}{T_{op}} \right)^{1.5} \quad (A-3)$$

Combining terms and defining P as the supply gauge pressure in psi (Equation A-4) and  $T_a$  as the supply temperature in °F (Equation A-5) yields Equation A-6.

$$P_{op} = P_a + P \approx 14.7 \text{ psia} + P \quad (A-4)$$

$$T_{op} = T_a + 460^\circ R \quad (A-5)$$

$$\dot{m} = 0.26708(\% \text{ Flow}) \left( \frac{14.7 + P}{Ta + 460} \right)^{1.5} \left[ \frac{lb_m}{sec} \right] \quad (A-6)$$

## Maxamp.m

Maxamp sweeps frequencies about the nominal frequency to determine the exact frequency of actuation and the offset and amplitude of the total pressure oscillation. The script solves Equation A-7 for frequencies within 50 Hz of the nominal frequency.

$$\begin{bmatrix} \vdots & \vdots & \vdots \\ 1 & \sin(2\pi f * t) & \cos(2\pi f * t) \\ \vdots & \vdots & \vdots \end{bmatrix} \begin{Bmatrix} x_1 \\ x_2 \\ x_3 \end{Bmatrix} = \begin{Bmatrix} \vdots \\ \text{data} \\ \vdots \end{Bmatrix} \quad (A-7)$$

It chooses the fit with the highest amplitude  $\sqrt{x_2^2 + x_3^2}$  and then sweeps a narrower band around that frequency at higher resolution. By repeating this refinement, maxamp.m resolves frequency to the closest 0.001 Hz.

```
function [f, amplitude, offset, X]=maxamp(data, basefreq)
%
% Inputs:           filename = text (in quotes) file name (with extension)
%                   basefreq = designed frequency of excitation (Hz)
%
% Output:          f = frequency of max amplitude (Hz)
%                   amplitude = max amplitude (V)
%                   offset = DC offset of signal (V)
%                   X = coefficients of fit components
%
% -----
%
time=.00005*[1:length(data)]';
max=0;
f=0;

for freq=(basefreq-25):(basefreq+25)
    A=[ones(size(time)),sin(2*pi*freq*time),cos(2*pi*freq*time)];
    x=A\data;
    amplitude=sqrt(x(2)^2+x(3)^2);
    if amplitude>max
        f=freq;
        max=amplitude;
    else
    end
end

max=0;
```

```

for freq=(f-1):.1:(f+1)
A=[ones(size(time)),sin(2*pi*freq*time),cos(2*pi*freq*time)];
x=A\data;
amplitude=sqrt(x(2)^2+x(3)^2);
if amplitude>max
    f=freq;
    max=amplitude;
else
end
end

max=0;
for freq=(f-.1):.01:(f+.1)
A=[ones(size(time)),sin(2*pi*freq*time),cos(2*pi*freq*time)];
x=A\data;
amplitude=sqrt(x(2)^2+x(3)^2);
if amplitude>max
    f=freq;
    max=amplitude;
else
end
end

max=0;
for freq=(f-.01):.001:(f+.01)
A=[ones(size(time)),sin(2*pi*freq*time),cos(2*pi*freq*time)];
x=A\data;
amplitude=sqrt(x(2)^2+x(3)^2);
if amplitude>max
    f=freq;
    max=amplitude;
    offset=x(1);
    X=x;
else
end
end

amplitude=max;

```

## C<sub>u</sub> Data Reduction

The motor speed varied slightly during the data recording phases, causing maxamp.m to be unable to lock onto a frequency that adequately matched the entire data stream (Figure A-1). The waveforms measured by the total pressure probe were also not sinusoidal, causing the fit maxamp.m applied to underestimate the oscillation amplitude (Figure A-2).

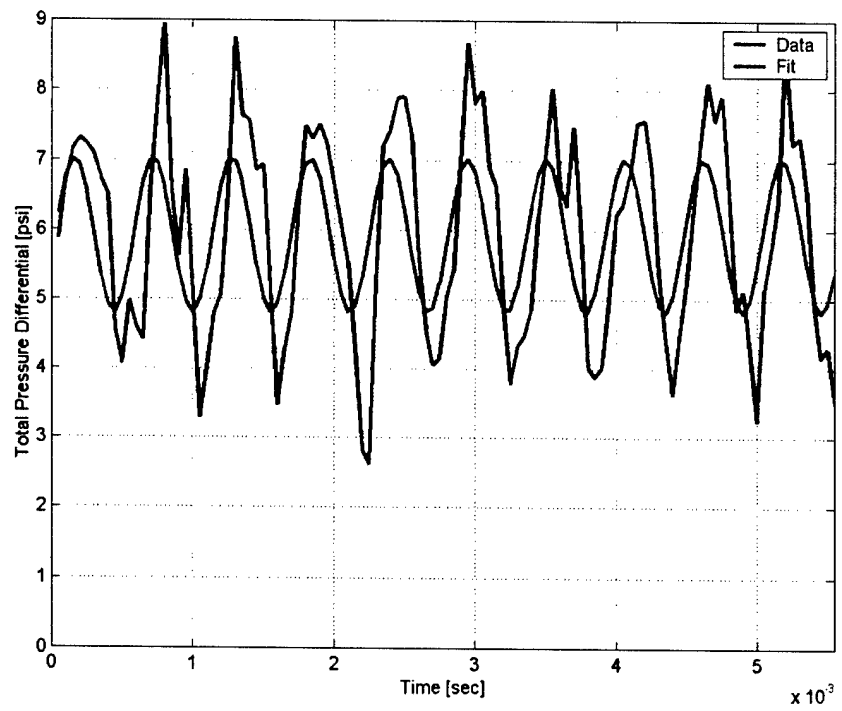


*Figure A-1: Frequency Mismatch using maxamp.m*

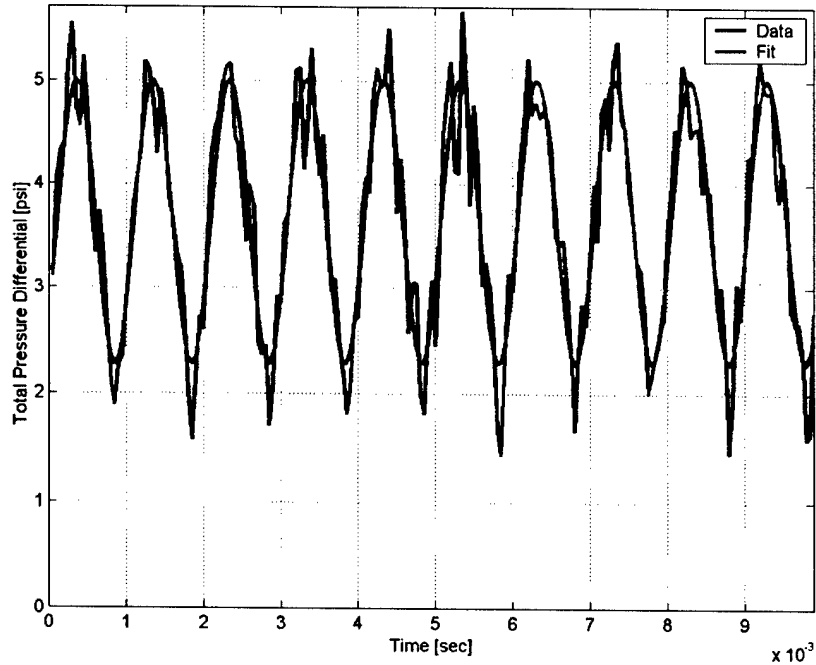


*Figure A-2: Underestimated Oscillation Amplitude due to Non-Sinusoidal Waveform*

The data was reduced using an ensemble average of 50 waveforms for frequencies lower than 1 kHz and 100 waveforms for higher frequencies. maxamp.m was edited to only fit the first 50 or 100 waveforms based on the design frequency. The frequency maxamp.m found to be the actuation frequency was input into ensemble.m. ensemble .m then used the initial data point as the beginning of the first waveform and determined the location each of the other data points in the first 50 or 100 waveforms occurred during a double cycle of actuation using the rem function in Matlab. The data was then reordered to place all the data points in sequential order by occurrence during the cycle using sortrows on the column of data representing the location of the data point in the waveform cycle. This constructed a double cycle from the first 50 or 100 waveforms (Figure A-3).

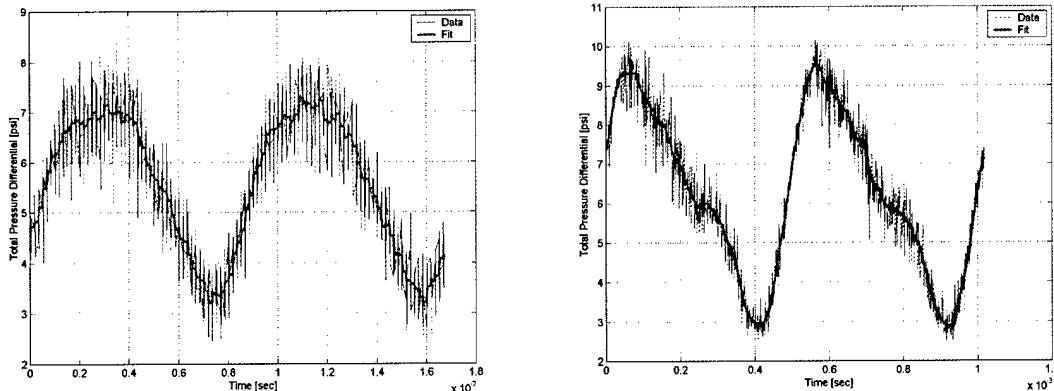


*Figure A-3: Examples of Composite Waveforms and Filtered Data Fit from ensemble.m*

This composite cycle was filtered using a Savitzky-Golay FIR smoothing filter in Matlab. The filter was set to a third order fit of the data over a 51-point window. The sliding filter determined the value at each point based on the local value of a cubic fit of the data point and the 25 points on either side. The maximum and minimum values of total pressure of the filter output between  $\frac{\tau}{2}$  and  $\frac{3\tau}{2}$  (where  $\tau = \frac{1}{f}$ ) were taken to be the extrema of total pressure over the waveform.

```
function [PT_hi,PT_low] = ensemble(data,freq,dp,location)
if freq<1000
```

```

        number_waveforms=50;
else
    number_waveforms=100;
end

data_rate=20000;

for i=1:(number_waveforms/freq)*data_rate;
    X(i,1)=rem(i/data_rate,2/freq);
    X(i,2)=data(i);
end

X=sortrows(X);

fit=sgolayfilt(X(:,2),3,51);
L=length(fit);

figure(2)

dummy=plot(X(:,1),X(:,2),X(:,1),fit);
set(dummy(2),'LineWidth',2)
grid
xlabel('Time [sec]')
ylabel('Total Pressure Differential [psi]')
legend('Data','Fit')
drawnow

print('-f2','-
djjpeg',['sgolay_',num2str(dp),'_',num2str(location),'_',num2str(100*round
(freq/100))])

PT_hi=max(fit(round((L-1)/4):round(3*(L+1)/4)));
PT_low=min(fit(round((L-1)/4):round(3*(L+1)/4)));

```

### Massflow curve.m

```

clear all

Pa=input('Ambient Pressure (psia)');
Ta=input('Ambient Temperature');

V=[1:.01:10];
x=.50517*V-.27751;
massflow=(-.0068*x.^4+.049*x.^3-.201*x.^2+1.355*x-
.016)*(Pa/14.7)*sqrt((460+73)/(460+Ta));

figure
plot(V,massflow)
grid
xlabel('Massflow Plug Voltage')
ylabel('Massflow (lbm/sec)')

```

### Calcmass.m

```
clear all

Pa=input('Ambient Pressure (psia)');
Ta=input('Ambient Temperature');
V=input('Massflow Plug Voltage');

x=.50517*V-.27751;
massflow=(-.0068*x.^4+.049*x.^3-.201*x.^2+1.355*x-
.016)*(Pa/14.7)*sqrt((460+73)/(460+Ta))
```

### Make map.m

```
R = [.95 .836 .706 .548 .314];
R = R(5:-1:1);
Theta=[2 1 0 -1 -2 -3 -4 -5]*pi/4;

load cfd_colormap

% Change to inlet massflow condition
inlet_mass=input('(1) 2.9 lbs/sec (2) 3.1 lbs/sec (3) 3.3 lbs/sec (4)
3.5 lbs/sec (5) 3.7 lbs/sec');
if inlet_mass==1
    cd mass_2_9
elseif inlet_mass==2
    cd mass_3_1
elseif inlet_mass==3
    cd ..
    cd 040502data
    cd mass_3_3
elseif inlet_mass==4
    cd ..
    cd 040502data
    cd mass_3_5
else
    cd ..
    cd 040502data
    cd mass_3_7
end

% Load data file
q=input('(1) for Percent Core Flow (2) for Mass Flow');
if q==1
    if inlet_mass==1
        inj_mass=input('% Core: (1)0.70 (2)1.19 (3)1.80 (4)2.28 (5)2.88
(6)3.68 (7)4.64 (8)5.78 (9)7.95 (10)Baseline');
    elseif inlet_mass==2
        inj_mass=input('% Core: (1)0.65 (2)1.09 (3)1.66 (4)2.18 (5)2.70
(6)3.41 (7)4.30 (8)5.36 (9)7.54 (10)Baseline');
    elseif inlet_mass==3
```

```

    inj_mass=input('% Core: (1)0.62 (2)1.03 (3)1.56 (4)2.02 (5)2.55
(6)3.23 (7)4.11 (8)5.08 (9)7.15 (10)Baseline');
elseif inlet_mass==4
    inj_mass=input('% Core: (1)0.58 (2)0.91 (3)1.41 (4)1.79 (5)2.36
(6)3.01 (7)3.84 (8)4.83 (9)6.64 (10)Baseline');
else
    inj_mass=input('% Core: (1)0.51 (2)0.84 (3)1.30 (4)1.70 (5)2.18
(6)2.74 (7)3.63 (8)4.57 (9)6.37 (10)Baseline');
end
else
    if inlet_mass==1
        inj_mass=input('lbm/sec: (1)0.020 (2)0.035 (3)0.052 (4)0.066
(5)0.084 (6)0.107 (7)0.135 (8)0.168 (9)0.231 (10)Baseline');
    elseif inlet_mass==2
        inj_mass=input('lbm/sec: (1)0.020 (2)0.034 (3)0.052 (4)0.068
(5)0.084 (6)0.106 (7)0.133 (8)0.166 (9)0.234 (10)Baseline');
    elseif inlet_mass==3
        inj_mass=input('lbm/sec: (1)0.020 (2)0.034 (3)0.051 (4)0.067
(5)0.084 (6)0.107 (7)0.136 (8)0.168 (9)0.236 (10)Baseline');
    elseif inlet_mass==4
        inj_mass=input('lbm/sec: (1)0.020 (2)0.032 (3)0.049 (4)0.063
(5)0.082 (6)0.106 (7)0.134 (8)0.169 (9)0.233 (10)Baseline');
    else
        inj_mass=input('lbm/sec: (1)0.019 (2)0.031 (3)0.048 (4)0.063
(5)0.081 (6)0.101 (7)0.134 (8)0.169 (9)0.236 (10)Baseline');
    end
end

if inj_mass==1
    dummy=9;
elseif inj_mass==2
    dummy=12;
elseif inj_mass==3
    dummy=15;
elseif inj_mass==4
    dummy=17;
elseif inj_mass==5
    dummy=19;
elseif inj_mass==6
    dummy=21;
elseif inj_mass==7
    dummy=23;
elseif inj_mass==8
    dummy=25;
else inj_mass==9
    dummy=28;
end

if inj_mass<10
    if inlet_mass==1
        PR=load(['040202_2_9_',num2str(dummy),'.txt']);
    elseif inlet_mass==2
        PR=load(['040202_3_1_',num2str(dummy),'.txt']);
    elseif inlet_mass==3
        PR=load(['040502_3_3_',num2str(dummy),'.txt']);
    elseif inlet_mass==4
        PR=load(['040502_3_5_',num2str(dummy),'.txt']);

```

```

else
    PR=load(['040502_3_7_',num2str(dummy),'.txt']);
end
else
    if inlet_mass==1
        PR=load(['040202_2_9_baseline.txt']);
    elseif inlet_mass==2
        PR=load(['040202_3_1_baseline.txt']);
    elseif inlet_mass==3
        PR=load(['040502_3_3_baseline.txt']);
    elseif inlet_mass==4
        PR=load(['040502_3_5_baseline.txt']);
    else
        PR=load(['040502_3_7_baseline.txt']);
    end
end

% Select run file
run=input('Run # (1 - 10)? (11 for average)');

PR(:,11)=mean(PR,2);

figure

for j=1:length(Theta)
    for i=1:length(R)
        X(i,j) = R(i)*cos(Theta(j));
        Y(i,j) = R(i)*sin(Theta(j));
        Z(i,j) = PR((j-1)*5+i,run);
        plot3(X,Y,2*Z,'ko'),hold on
    end
end

for i=1:2
    r = 1/i;
    j=0;
    for Thet = 0:2*pi/50:2*pi
        j=j+1;
        xcircle(i,j)=r*cos(Thet);
        ycircle(i,j)=r*sin(Thet);
        zcircle(i,j)=.75;
    end
end

counter=length(Theta)+1;
for i=1:length(R)
    X(i,counter)=X(i,1);
    Y(i,counter)=Y(i,1);
    Z(i,counter)=Z(i,1);
end

press_recovery=mean(PR(:,run))

h=surf(X,Y,Z);
%contour(X,Y,Z);
surf(xcircle,ycircle,zcircle)

```

```

colormap(cfd)
shading interp
view(0,90)
axis('square')
grid
colorbar
hold off

```

```
cd ..
```

```

if inlet_mass>2
    cd ..
    cd 040202data
else
end

```

### **Make plot.m**

```

clear all

q=input('(1) for Percent Core Flow (2) for Mass Flow (3) for Steady
Cmu');
if q==1
    massin=[0 0.7 1.19 1.8 2.28 2.88 3.68 4.64 5.78 7.95;
             0 0.65 1.09 1.66 2.18 2.7 3.41 4.3 5.36 7.54;
             0 0.62 1.03 1.56 2.02 2.55 3.23 4.11 5.08 7.15;
             0 0.58 0.91 1.41 1.79 2.36 3.01 3.84 4.83 6.64;
             0 0.51 0.84 1.3 1.7 2.18 2.74 3.63 4.57 6.37];
elseif q==2
    massin=[0 0.02 0.035 0.052 0.066 0.084 0.107 0.135 0.168 0.231;
             0 0.02 0.034 0.052 0.068 0.084 0.106 0.133 0.166 0.234;
             0 0.02 0.034 0.051 0.067 0.084 0.107 0.136 0.168 0.236;
             0 0.02 0.032 0.049 0.063 0.082 0.106 0.134 0.169 0.233;
             0 0.019 0.031 0.048 0.063 0.081 0.101 0.134 0.169 0.236];
else
    load steadycmufit
    PR=[(14.7576+[7.5 11 14.75 17.75 20 23.25 27 31 38.5])/11.76;
        (14.7576+[7.5 11.5 15 17.25 20 23.5 27.25 31.25 38])/11.11;
        (14.777+[7.5 11 14.5 17.25 20 23.25 27.25 31 38.5])/10.25;
        (14.777+[7.5 10 13.75 16 19.5 23 27 31.25 38])/8.59;
        (14.777+[5 9.5 13.25 16 19 22 27 31.25 38.5])/7.81];
    steadycmu=[0 (P(1)*PR(1,:)+P(2))/.840; % Adjusted for core flow
2.9 lb/sec
                0 (P(1)*PR(2,:)+P(2))/1.000;
                0 (P(1)*PR(3,:)+P(2))/1.201; % Adjusted for core flow
3.3 lb/sec
                0 (P(1)*PR(4,:)+P(2))/1.532; % Adjusted for core flow
3.5 lb/sec
                0 (P(1)*PR(5,:)+P(2))/1.661]; % Adjusted for core flow
3.7 lb/sec
end

% Survey both inlet massflow conditions
for inlet_mass=1:5

```

```

if inlet_mass==1
    cd mass_2_9
elseif inlet_mass==2
    cd mass_3_1
elseif inlet_mass==3
    cd ..
    cd 040502data
    cd mass_3_3
elseif inlet_mass==4
    cd ..
    cd 040502data
    cd mass_3_5
else
    cd ..
    cd 040502data
    cd mass_3_7
end

% Load data file
for inj_mass=1:10
    if inj_mass==1
        dummy=9;
    elseif inj_mass==2
        dummy=12;
    elseif inj_mass==3
        dummy=15;
    elseif inj_mass==4
        dummy=17;
    elseif inj_mass==5
        dummy=19;
    elseif inj_mass==6
        dummy=21;
    elseif inj_mass==7
        dummy=23;
    elseif inj_mass==8
        dummy=25;
    else inj_mass==9
        dummy=28;
    end

if inj_mass<10
    if inlet_mass==1
        PR=load(['040202_2_9_',num2str(dummy),'.txt']);
    elseif inlet_mass==2
        PR=load(['040202_3_1_',num2str(dummy),'.txt']);
    elseif inlet_mass==3
        PR=load(['040502_3_3_',num2str(dummy),'.txt']);
    elseif inlet_mass==4
        PR=load(['040502_3_5_',num2str(dummy),'.txt']);
    else
        PR=load(['040502_3_7_',num2str(dummy),'.txt']);
    end
else
    if inlet_mass==1
        PR=load(['040202_2_9_baseline.txt']);
    elseif inlet_mass==2

```

```

    PR=load(['040202_3_1_baseline.txt']);
elseif inlet_mass==3
    PR=load(['040502_3_3_baseline.txt']);
elseif inlet_mass==4
    PR=load(['040502_3_5_baseline.txt']);
else
    PR=load(['040502_3_7_baseline.txt']);
end
end

    pressure_recovery(inlet_mass,rem(inj_mass,10)+1)=mean(mean(PR,2));
end

cd ..

if inlet_mass>2
    cd ..
    cd 040202data
else
end

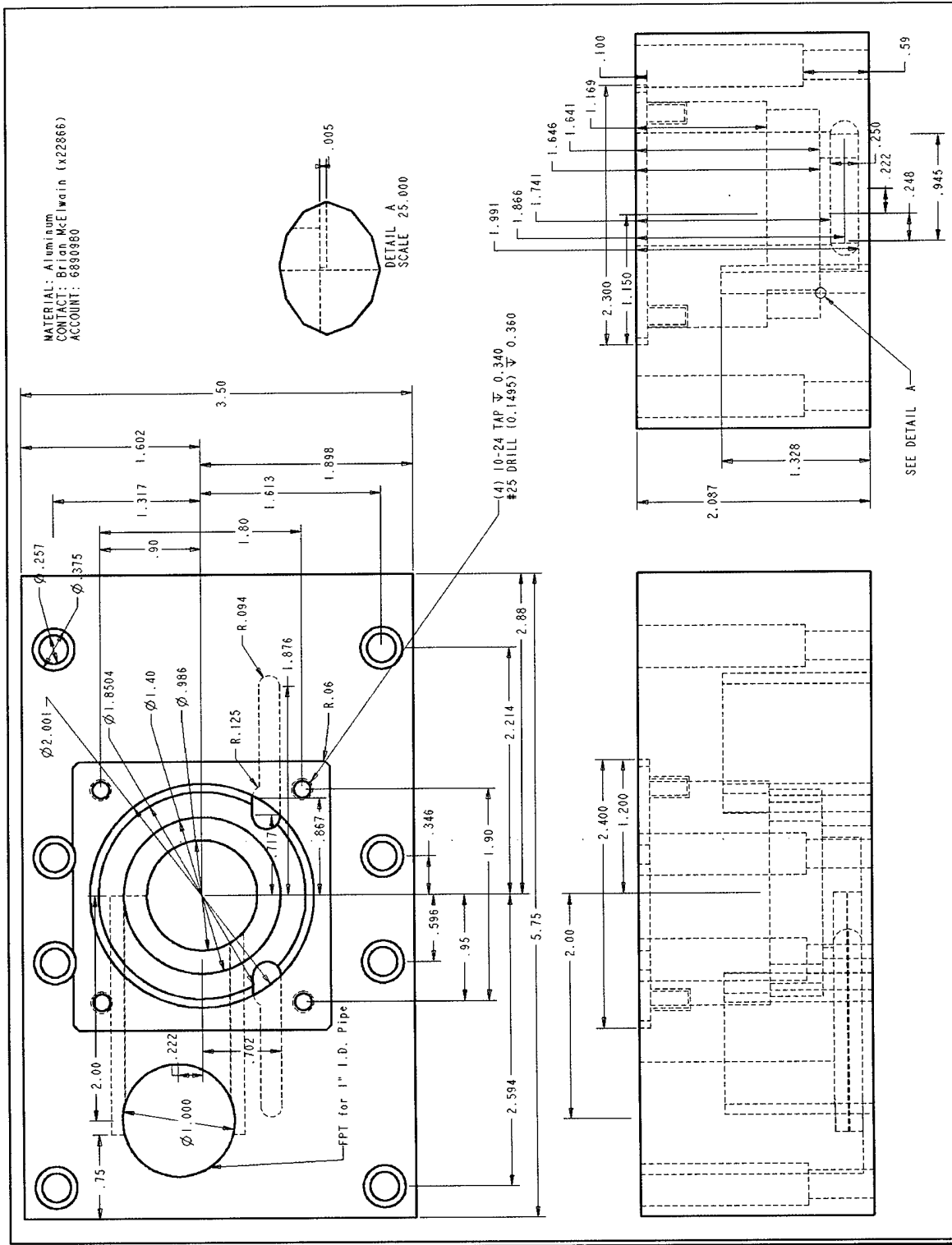
end

figure
if q==1
    plot(massin',pressure_recovery')
    title('Pressure Recovery vs Injection Flow at 2kHz')
    xlabel('Average Injection Massflow (% Core Massflow)')
    ylabel('Pressure Recovery')
    legend('2.9 lb/sec Core Flow','3.1 lb/sec Core Flow','3.3 lb/sec Core
Flow','3.5 lb/sec Core Flow','3.7 lb/sec Core Flow')
    grid
elseif q==2
    plot(massin',pressure_recovery')
    title('Pressure Recovery vs Injection Flow at 2kHz')
    xlabel('Average Injection Massflow (lb/sec)')
    ylabel('Pressure Recovery')
    legend('2.9 lb/sec Core Flow','3.1 lb/sec Core Flow','3.3 lb/sec Core
Flow','3.5 lb/sec Core Flow','3.7 lb/sec Core Flow')
    grid
else
    plot(steadycmu',pressure_recovery')
    title('Pressure Recovery vs Injection Flow at 2kHz')
    xlabel('Steady Cmu')
    ylabel('Pressure Recovery')
    legend('2.9 lb/sec Core Flow','3.1 lb/sec Core Flow','3.3 lb/sec Core
Flow','3.5 lb/sec Core Flow','3.7 lb/sec Core Flow')
    grid
end

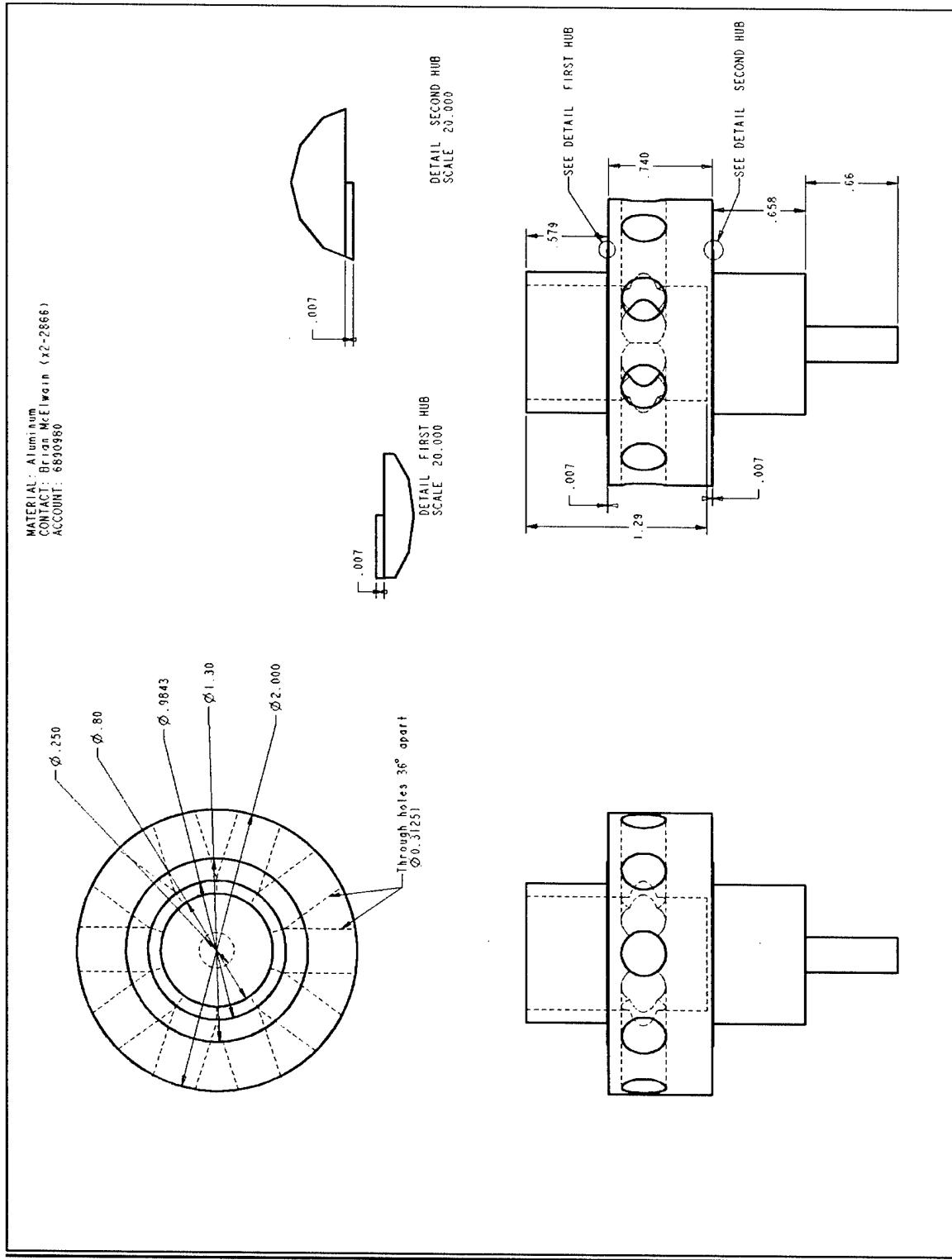
```

## **Appendix B: Component Drawings**

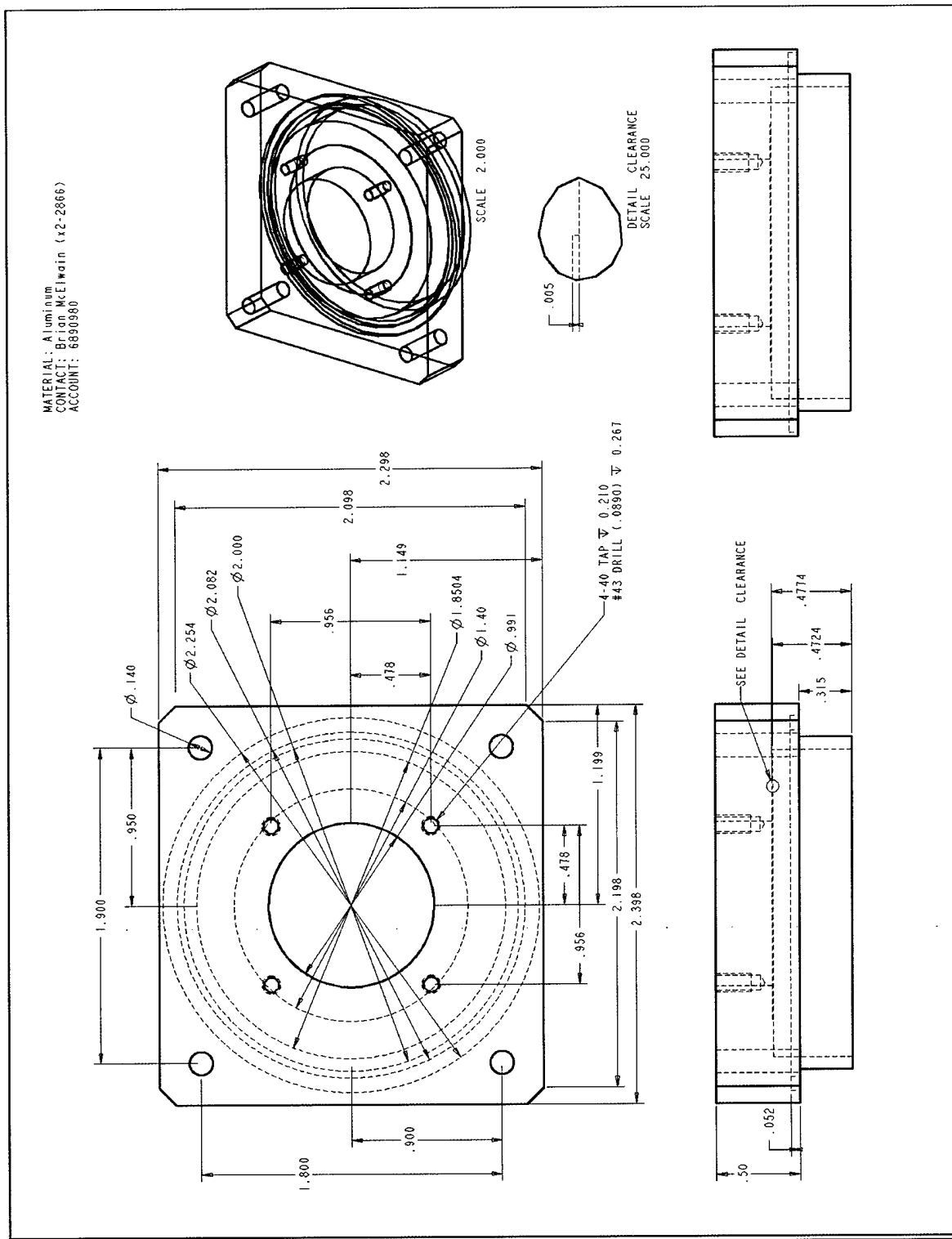
## Rotary Valve Body



## Rotary Valve Rotor

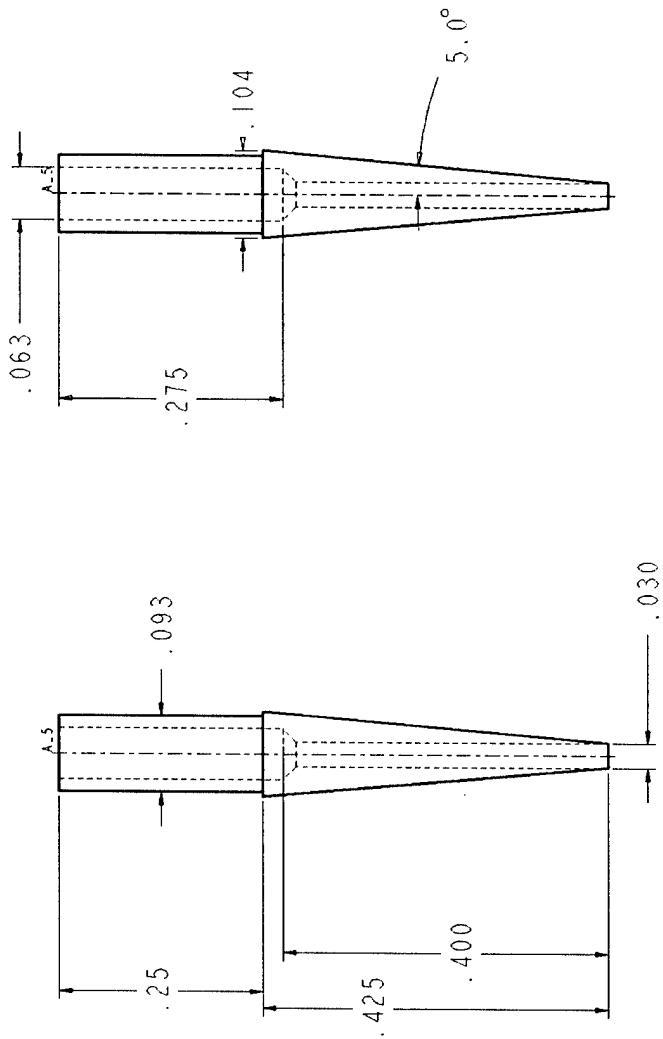


## Rotary Valve Top



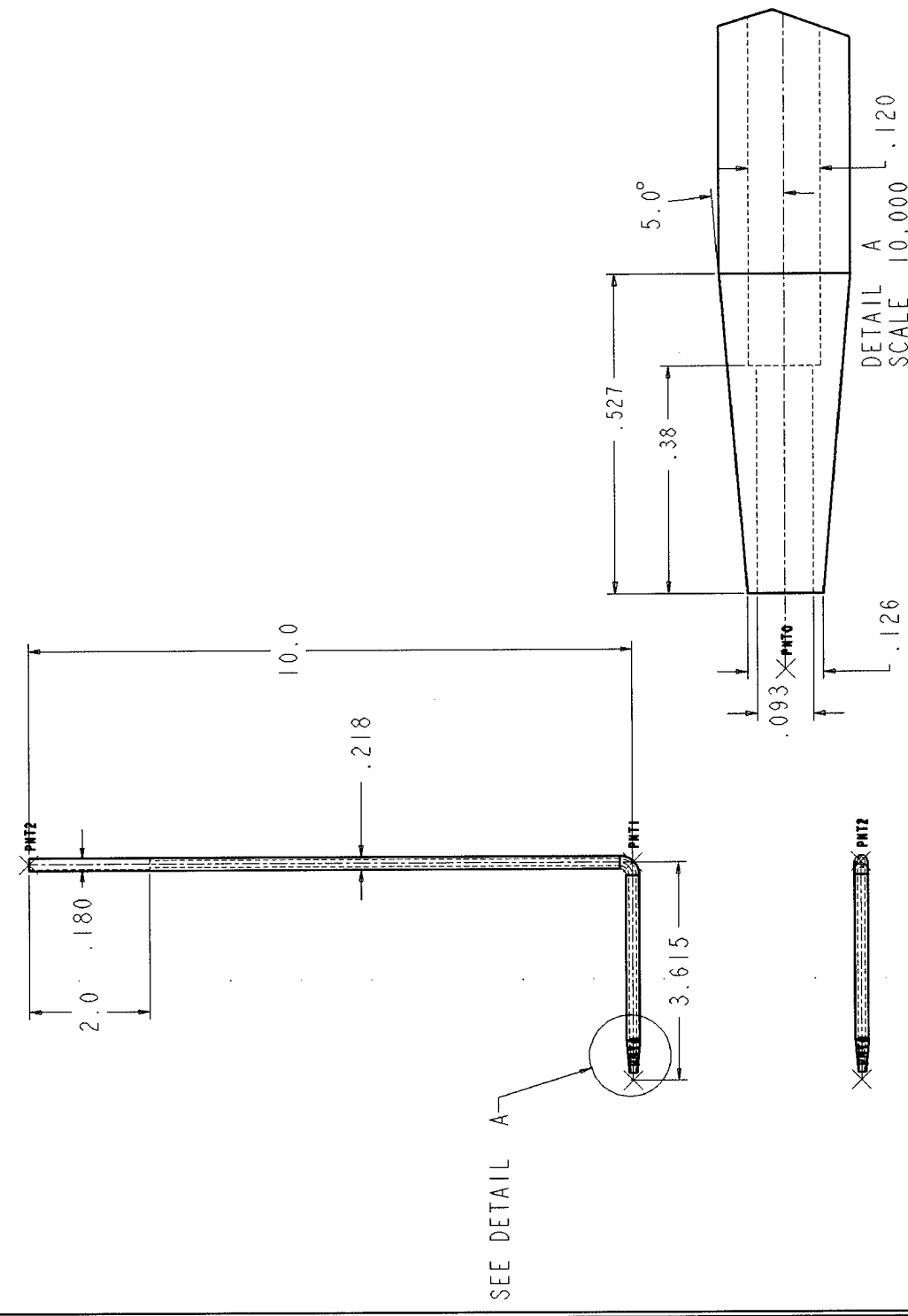
## Total Pressure Probe Head

CONTACT: Brian McElwain  
PHONE: x2-2866



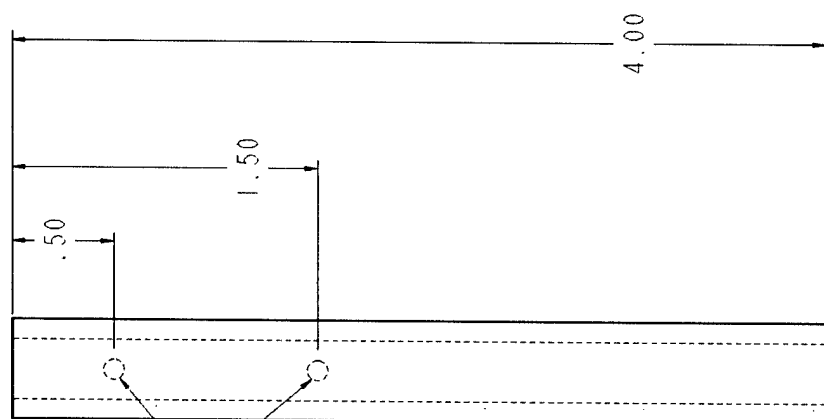
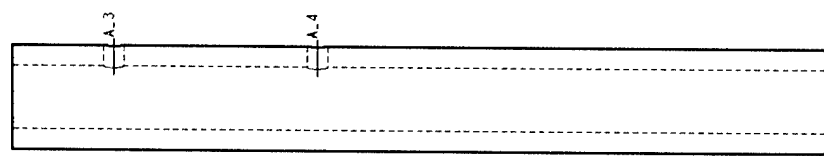
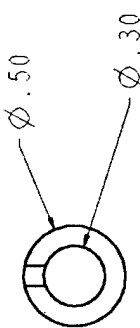
## Total Pressure Probe Body

CONTACT: Brian McIlwain  
PHONE: x2-2866



## **Total Pressure Probe Base**

CONTACT: Brian McElwain  
PHONE: x2-2866  
ACCOUNT: 6890980



## Appendix C: Injector Redesign

Based on feedback from several sources, the injector duct was redesigned. The redesigned injector has a maximum of 1.25 percent core flow. This allows the same velocity perturbations while reducing the quantity of flow necessary to reach high velocities, effectively reducing the mean flow necessary to reach a given actuation level.

The ratio of the supply duct area to the injector exit area was decreased to increase frequency response of the duct. This increased the flow from a maximum of Mach 0.15 to a maximum of Mach 0.30.

Anthony Strazisar at NASA Glenn suggested the concentric circles forming the exit of the duct did not need to be concentric. Offsetting the centers discarded the long, high velocity section at the exit that causes relatively high losses. Instead, the flow converges through the curved section accelerating to Mach 1 at the exit.

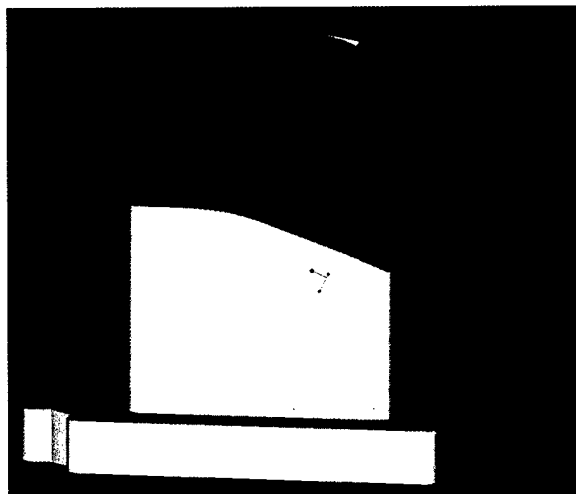


*Figure C-1: Redesigned Injector Insert*

The flow path into the supply duct was also redesigned. In the original injectors, the flow from the actuator tried to follow an abrupt turn toward the centerline as soon as it entered the supply duct. This turn could cause the flow through the supply duct to separate from the wall, causing an effective blockage and non-uniform exit flow. This abrupt turn was

changed to be more axial at the inlet and exit of the supply duct, resulting in an S-shaped inner wall (Figure C-2).

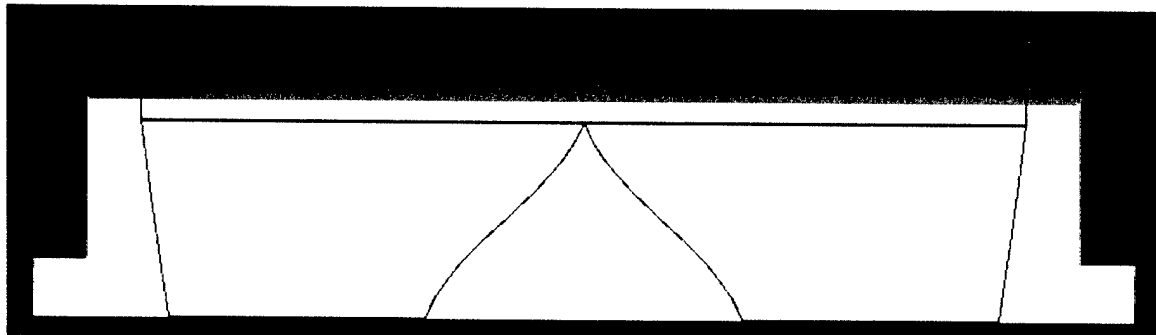


*Figure C-2: Front View of Redesigned Supply Duct*

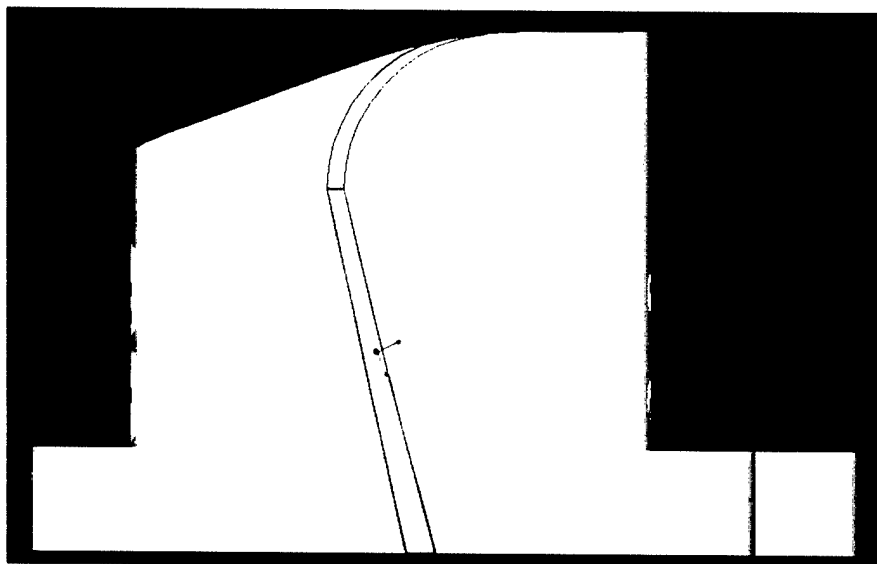


*Figure C-3: Side View of Redesigned Supply Duct*

After the injector block was designed, the block was split into two pieces along the duct (Figures C-4 and C-5). 0.040 inches was removed from the interface. Bolt holes were added through the sides and the divider between the supply paths. This allows the block to be shimmed to a desired width, resizing the injector anywhere from zero flow up to a maximum 1.25 percent core flow. The additional leak paths created by this design are sealed by placing vacuum tape<sup>1</sup> between the shims.

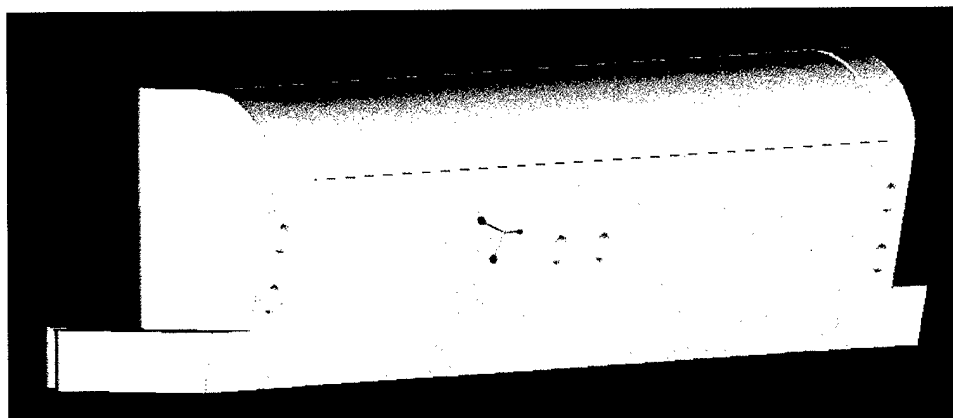


*Figure C-4: Front Half of Redesigned Injector*

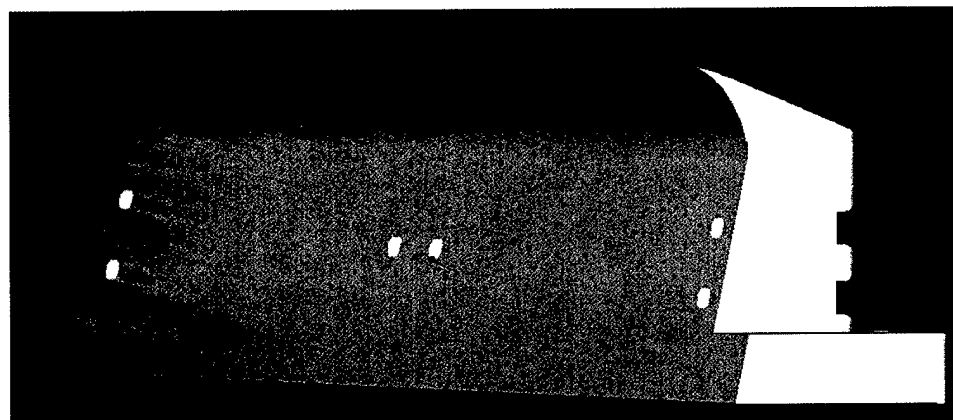


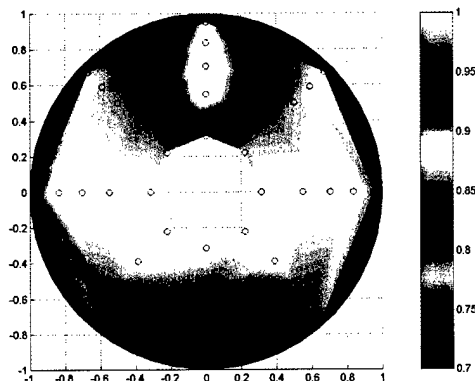
*Figure C-5: Back Half of Redesigned Injector*

The redesigned injector halves were also grown using the same SLS process at NASA Glenn. Unfortunately, the parts did not arrive at MIT in time for their testing to be recorded in this thesis.

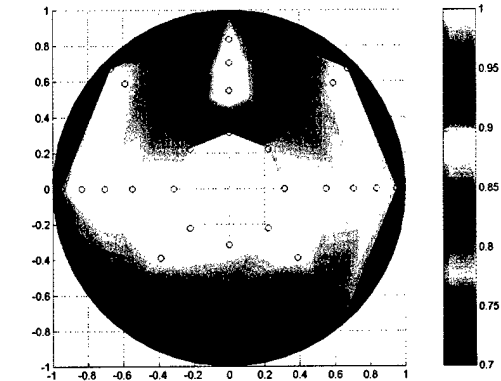


## Appendix D: Aerodynamic Interface Plane (AIP) Profiles

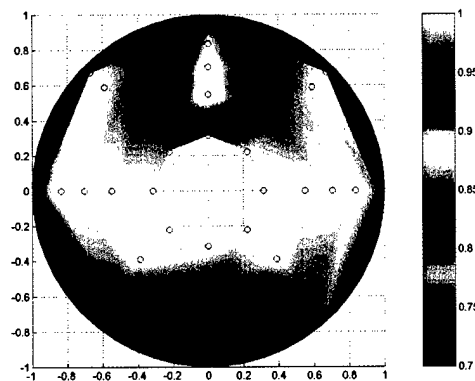
### 2.9 lb/sec Core Flow



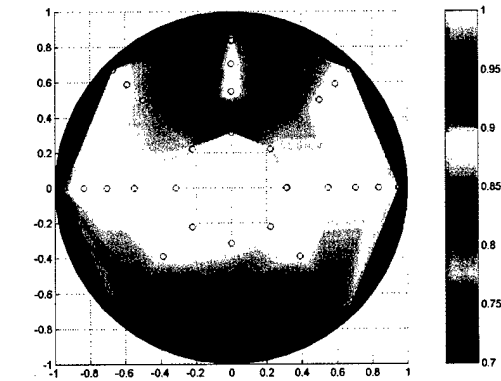
*Baseline*



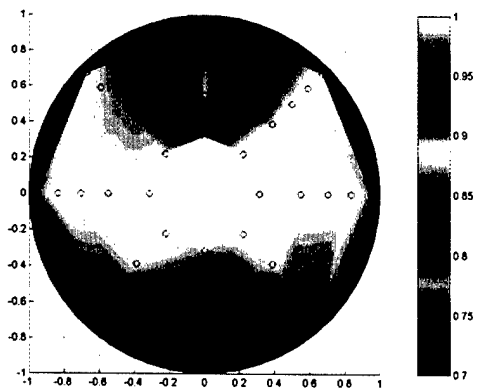
*0.020 lb/sec Injection Flow*



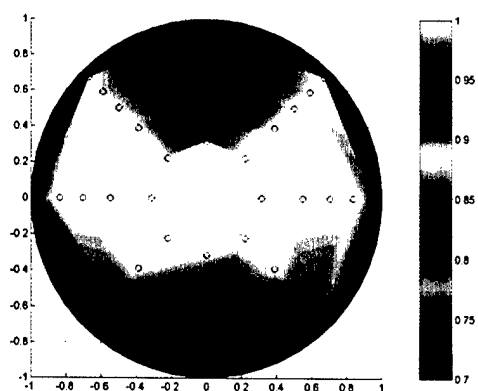
*0.035 lb/sec Injection Flow*



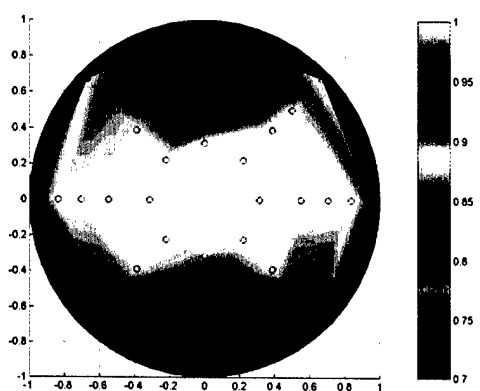
*0.052 lb/sec Injection Flow*



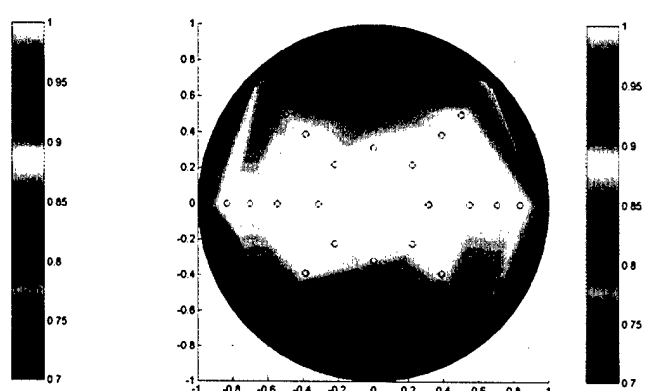
*0.066 lb/sec Injection Flow*



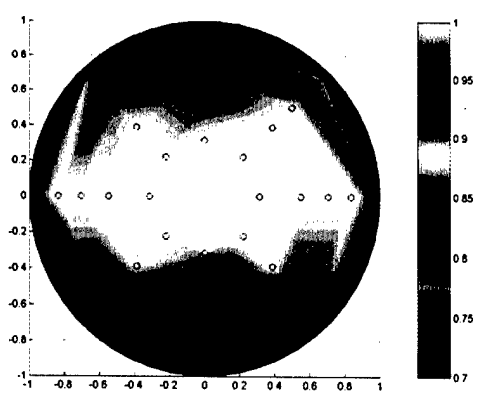
*0.084 lb/sec Injection Flow*



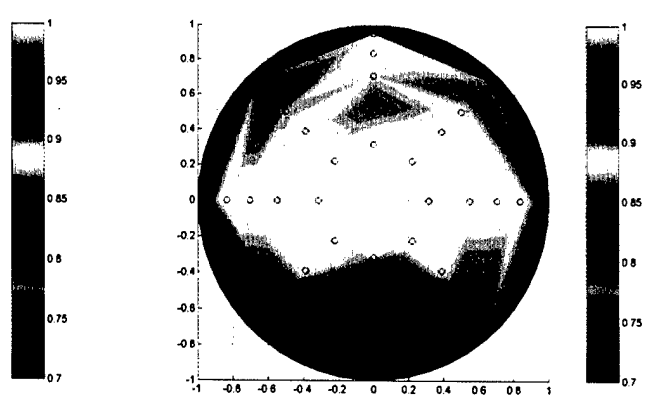
*0.107 lb/sec Injection Flow*



*0.135 lb/sec Injection Flow*

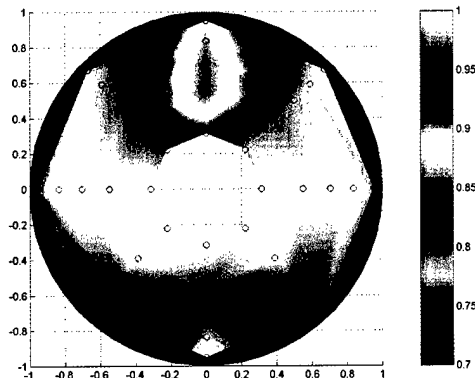


*0.168 lb/sec Injection Flow*

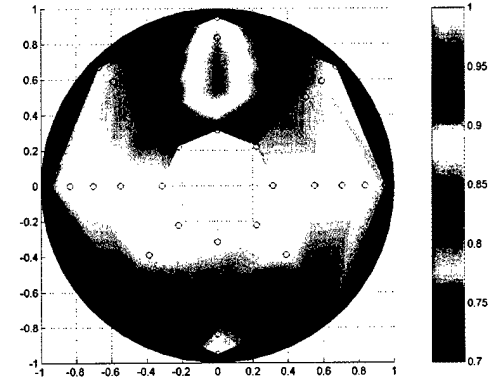


*0.231 lb/sec Injection Flow*

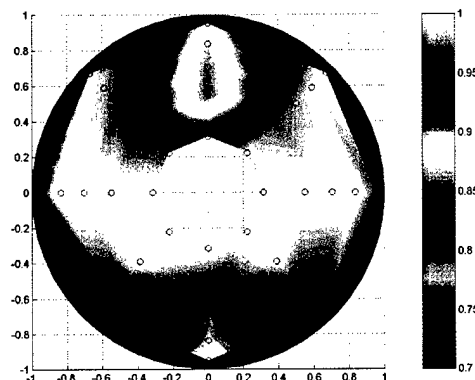
### 3.1 lb/sec Core Flow



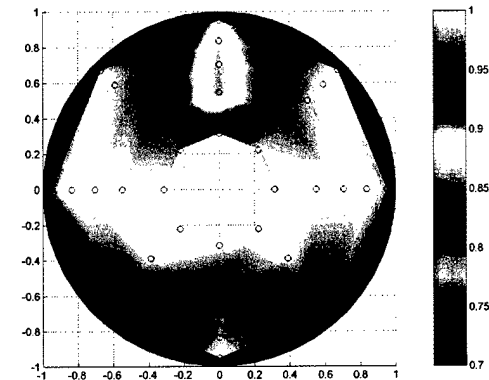
*Baseline*



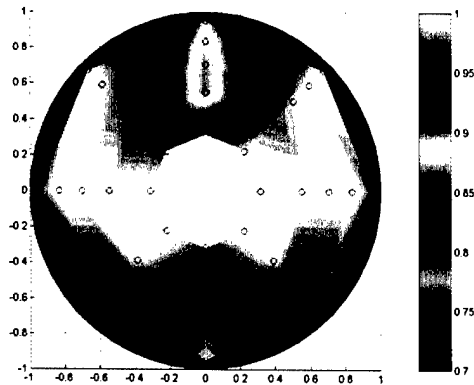
*0.020 lb/sec Injection Flow*



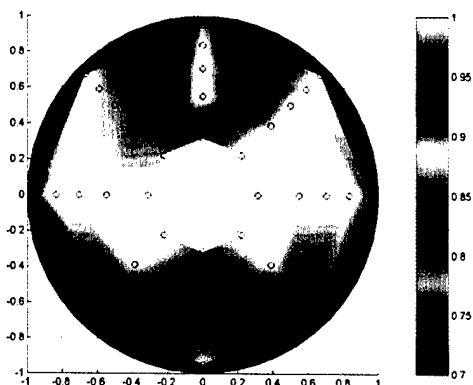
*0.034 lb/sec Injection Flow*



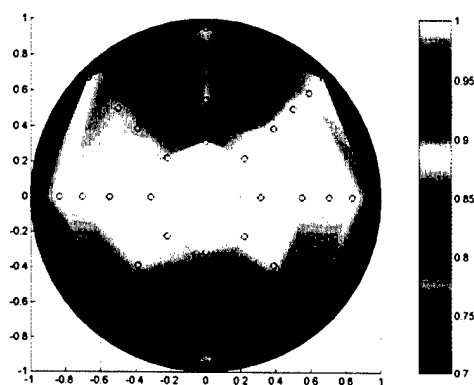
*0.052 lb/sec Injection Flow*



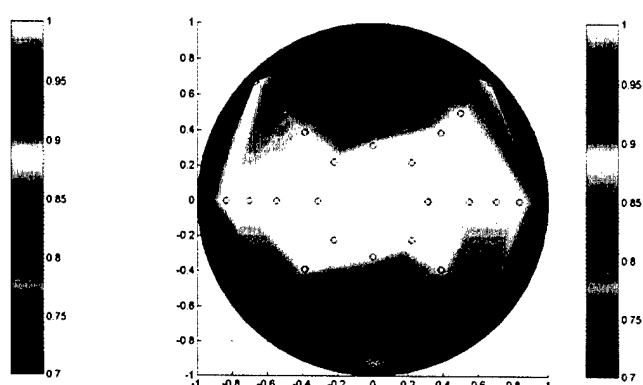
0.068 lb/sec Injection Flow



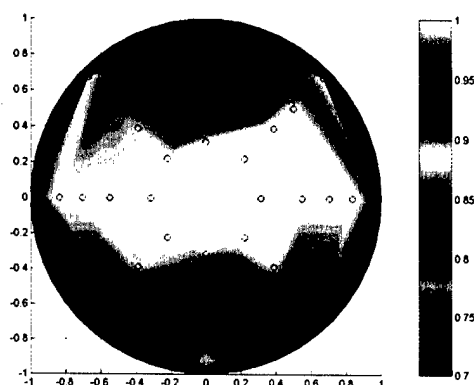
0.084 lb/sec Injection Flow



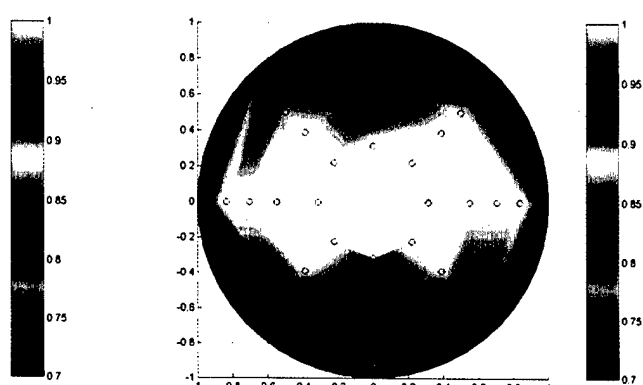
0.106 lb/sec Injection Flow



0.133 lb/sec Injection Flow

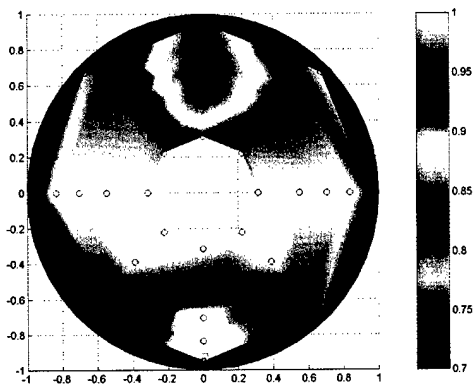


0.166 lb/sec Injection Flow

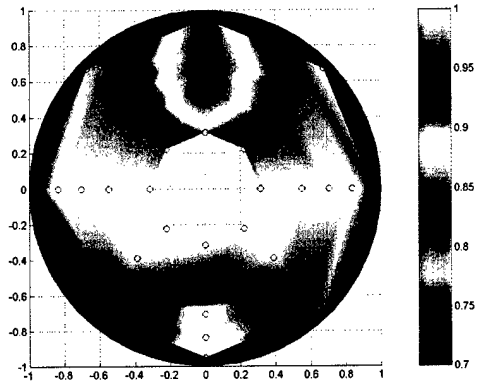


0.234 lb/sec Injection Flow

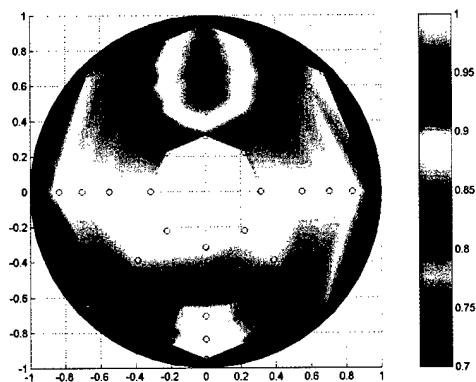
### **3.3 lb/sec Core Flow**



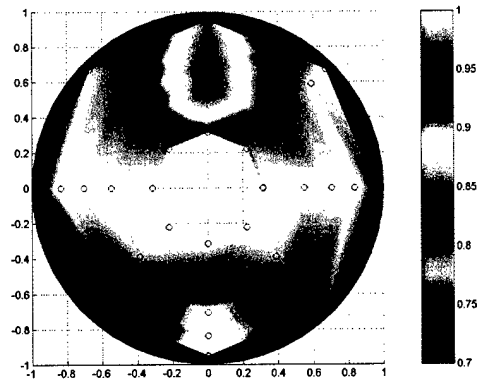
*Baseline*



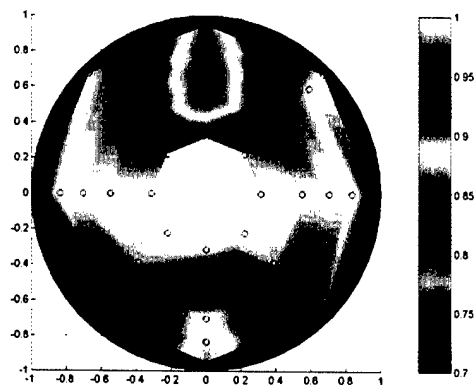
*0.020 lb/sec Injection Flow*



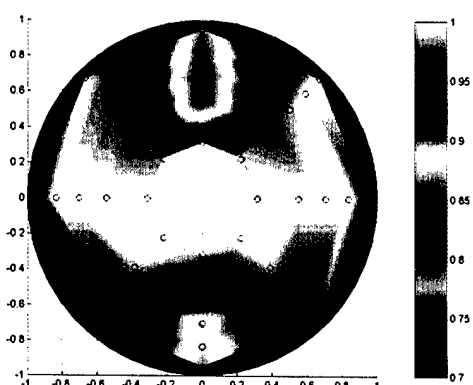
*0.034 lb/sec Injection Flow*



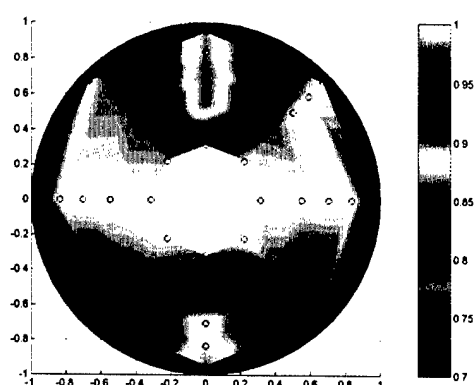
*0.051 lb/sec Injection Flow*



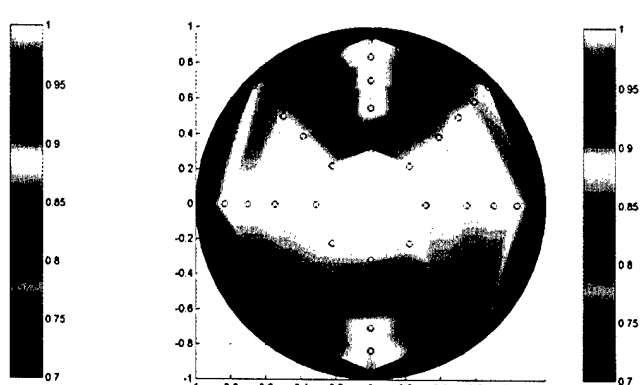
*0.067 lb/sec Injection Flow*



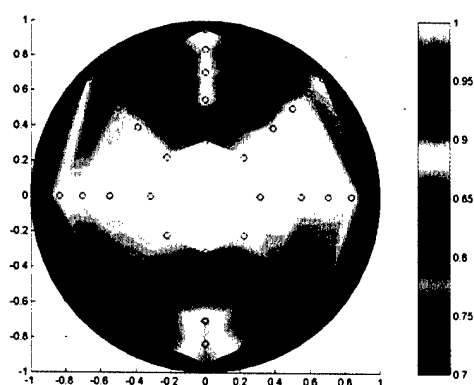
*0.084 lb/sec Injection Flow*



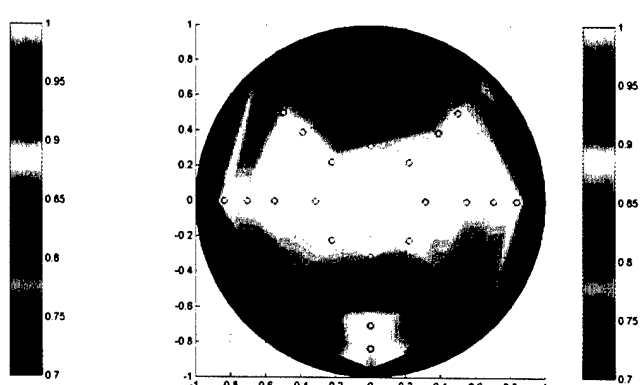
*0.107 lb/sec Injection Flow*



*0.136 lb/sec Injection Flow*

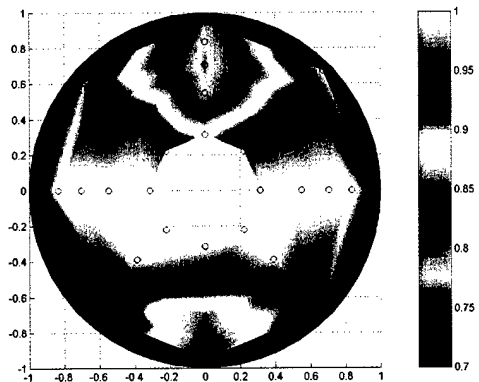


*0.168 lb/sec Injection Flow*

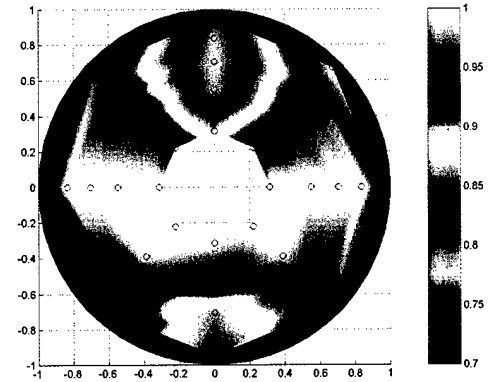


*0.236 lb/sec Injection Flow*

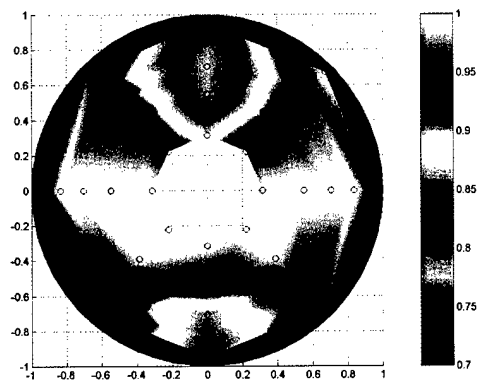
### 3.5 lb/sec Core Flow



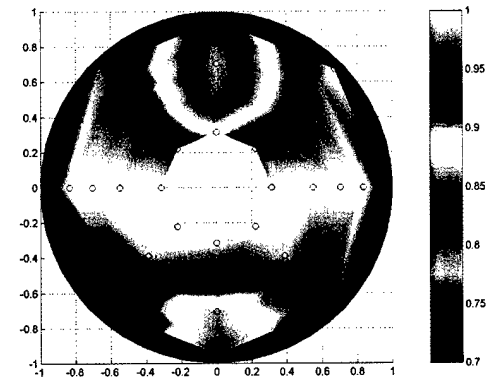
*Baseline*



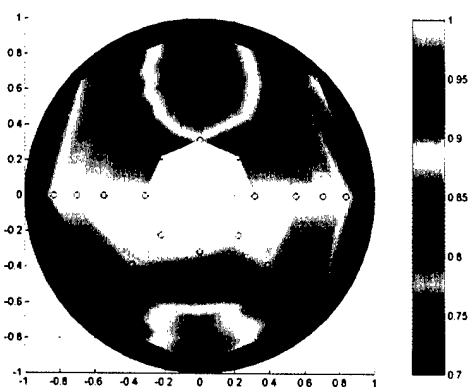
*0.020 lb/sec Injection Flow*



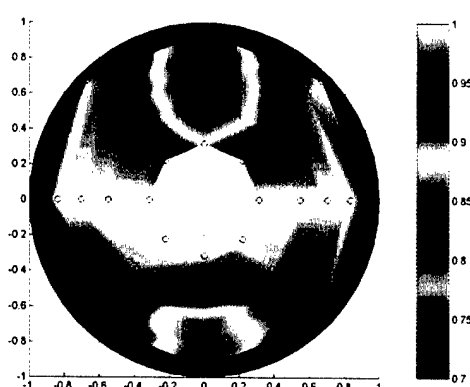
*0.032 lb/sec Injection Flow*



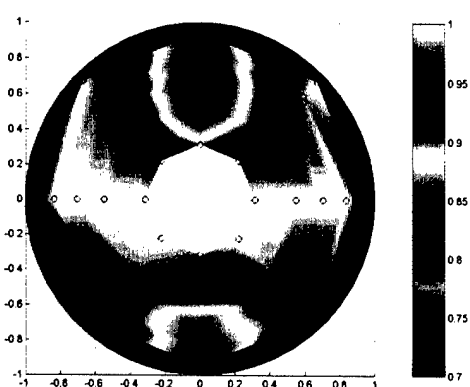
*0.049 lb/sec Injection Flow*



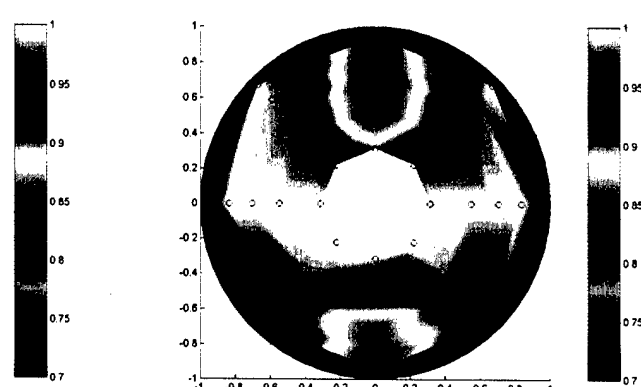
0.063 lb/sec Injection Flow



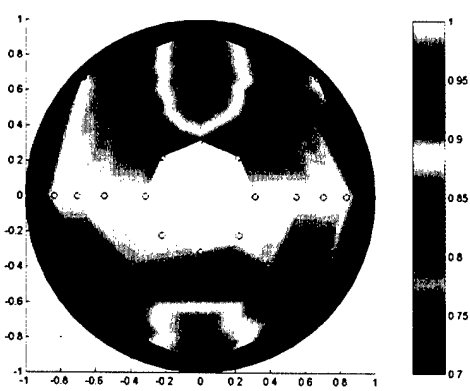
0.082 lb/sec Injection Flow



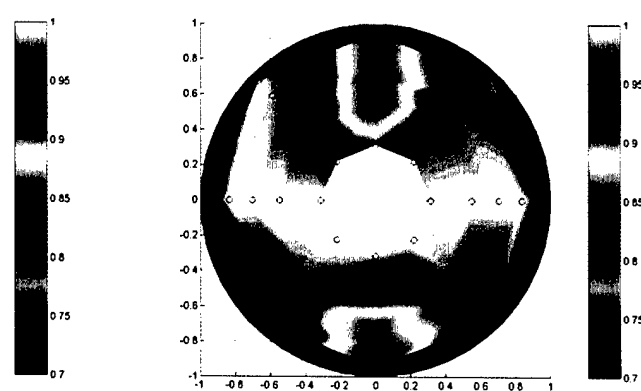
0.106 lb/sec Injection Flow



0.134 lb/sec Injection Flow

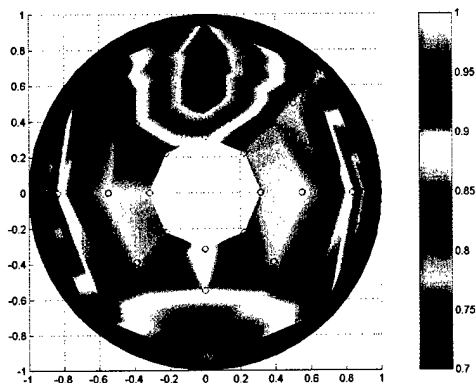


0.169 lb/sec Injection Flow

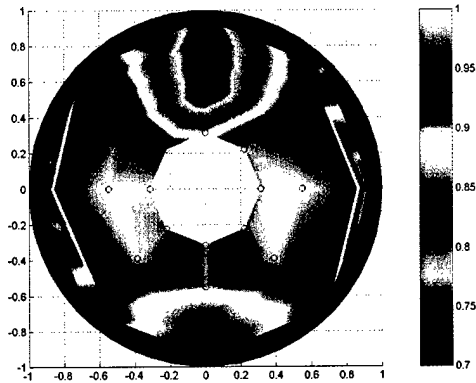


0.233 lb/sec Injection Flow

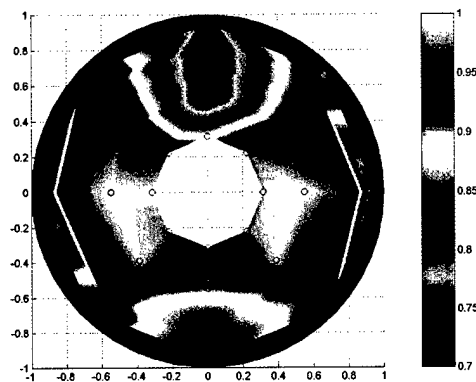
### 3.7 lb/sec Core Flow



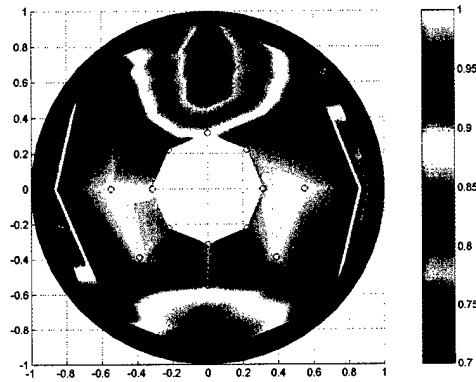
*Baseline*



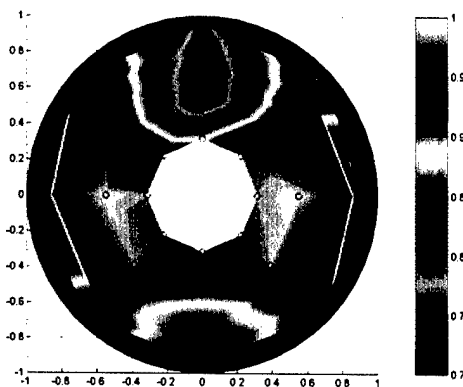
*0.019 lb/sec Injection Flow*



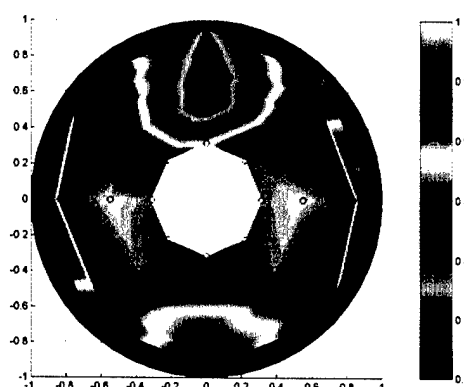
*0.031 lb/sec Injection Flow*



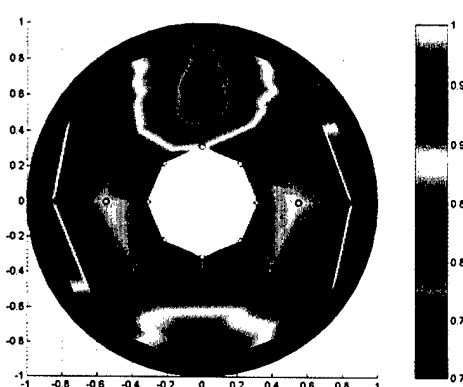
*0.048 lb/sec Injection Flow*



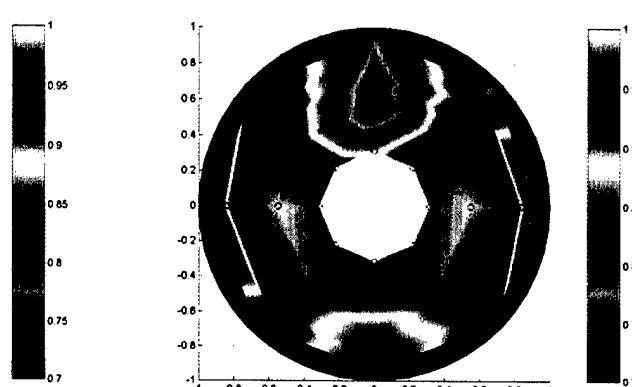
0.063 lb/sec Injection Flow



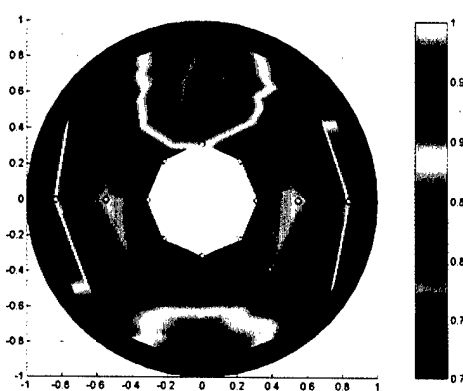
0.081 lb/sec Injection Flow



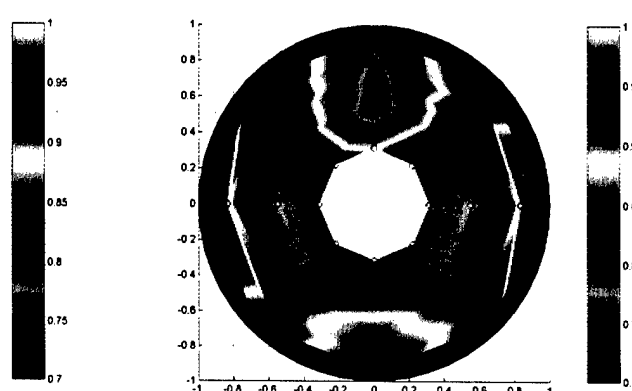
0.101 lb/sec Injection Flow



0.134 lb/sec Injection Flow



0.169 lb/sec Injection Flow



0.236 lb/sec Injection Flow

## References

---

- 1 D. Greenblatt and I. J. Wygnanski, "The control of flow separation and by periodic excitation," *Progress in Aerospace Sciences*, vol. 36, pp. 487-545, 2000.
- 2 J. Paduano, personal communications, 2000-2002.
- 3 A. Seifert and L. G. Pack, "Separation Control at Flight Reynolds Numbers: Lessons Learned and Future Directions," in *Fluids 2000*. AIAA 2000-2542.
- 4 D. C. McCormick, "Boundary Layer Separation Control with Directed Synthetic Jets," in *AIAA Aerospace Sciences Conference*. AIAA 2000-0519.
- 5 M. Amitay, D. Pitt, V. Kibens, D. Parekh, and A. Glezer, "Control of Internal Flow Separation using Synthetic Jet Actuators," AIAA 2000-0903.
- 6 Z. Warfield, "Active Control of Separation Induced Distortion in a Scaled Tactical Aircraft Inlet", M.S. thesis, Department of Aeronautics and Astronautics, Massachusetts Institute of Technology, Cambridge, MA 2001.
- 7 R.G. Berndt, "Actuation for Rotating Stall Control of High Speed Axial Compressors", M.S. thesis, Department of Aeronautics and Astronautics, Massachusetts Institute of Technology, Cambridge, MA 1995.
- 8 D. MacMartin, personal communications, 2000-2002.
- 9 J. Kane, personal communications, 2000.
- 10 J. Philhower, personal communications, 2001.
- 11 "Astro Ten to Twenty Cell Sport Motors" Online: <http://www.astroflight.com/sport1020.html>, May 2002.
- 12 Online: [http://www.torrington.com/products/catalog/E3\\_69.pdf](http://www.torrington.com/products/catalog/E3_69.pdf), p 65-66, May 2002.

---

13 N.A. Cumpsty, *Compressor Aerodynamics*, Singapore: Addison Wesley Longman China Limited, 1989, 384.

14 G. Guenette, Jr., personal communications, 2000-2002.

15 GTL LEMO wiring standard: Red – Positive Excitation, Black – Negative Excitation, Green – Positive Sense, White – Negative Sense

16 S. Braddom, “Design and Characterization of Robust Hot Film Sensors for Tactical Aircraft Inlets”, M.S. thesis, Department of Aeronautics and Astronautics, Massachusetts Institute of Technology, Cambridge, MA 2002.